Local structure of liquid 3d metals under extreme conditions of pressure and temperature

Silvia Boccato

Communauté
UNIVERSITÉ Grenoble Alpes

THÈSE

Pour obtenir le grade de

DOCTEUR DE LA COMMUNAUTÉ UNIVERSITÉ GRENOBLE ALPES

Spécialité : Physique de la Matière Condensée et du Rayonnement

Arrêté ministériel : 25 mai 2016

Présentée par

Silvia BOCCATO

Thèse dirigée par **Dr. Sakura PASCARELLI**
et codirigée par **Dr. Raffaella TORCHIO**

préparée au sein du **European Synchrotron Radiation Facility**
dans **l'École Doctorale de Physique**

Etude de la structure locale des métaux 3*d* liquides en conditions extrêmes de pression et température

Local structure of liquid 3*d* metals under extreme conditions of pressure and temperature

Thèse soutenue publiquement le **19 décembre 2017**,
devant le jury composé de :

Prof. Dr. Andrea DI CICCO, Rapporteur
Professeur, UNIVERSITE DE CAMERINO
Prof. Dr. François GUYOT, Rapporteur
Professeur, UNIVERSITE PIERRE ET MARIE CURIE
Dr. Daniele ANTONANGELI, Examinateur
Chargé de Recherche, UNIVERSITE PIERRE ET MARIE CURIE
Dr. Agnès DEWAELE, Examinatrice
Ingénieur de Recherche, CEA DE SACLAY
Dr. Jean-Paul ITIÉ, Examinateur
Directeur de Recherche, SYNCHROTRON SOLEIL
Prof. Dr. Alexandre SIMIONOVICI, Président
Professeur, UNIVERSITE GRENOBLE ALPES

Summary

Understanding the physical phenomena of our planet requires the capability to investigate the structural and thermodynamic properties of liquid-state materials present in the Earth's outer core. In particular, the melting curves of 3d metals such as nickel and cobalt allow to constrain the temperature at the boundary between inner and outer core in the Earth, the inner core boundary (ICB). This Thesis presents the study of the melting curves and the local structure of nickel and cobalt under extreme conditions. The experimental analysis was performed by X-ray absorption spectroscopy (XAS), suitable technique for the study of the local structure. *Ab-initio* calculations were performed as well in order to validate the melting criterion adopted and to provide starting radial distribution function for the analysis of the local structure.

The melting curves of nickel and cobalt were determined with the XAS melting criterion recently proposed for iron under extreme conditions. The criterion consists in the flattening of the shoulder and the disappearance of the first two oscillations in the X-ray Absorption Near Edge Structure (XANES). It has been validated by Focused Ion Beam (FIB) coupled with Scanning Electron Microscopy (SEM) analysis on the recovered samples, by means of a detection of textural changes in the sample. The melting temperature was detected for nickel and cobalt at different pressures up to 1 Mbar for the two materials. A comparison between the melting curves of nickel and cobalt with iron shows that the melting curves of these 3d metals up to 1 Mbar are very similar, suggesting that: the number of d electrons has no clear influence on the slope of the melting curves of these three materials and that the presence of nickel in the outer core of Earth gives a negligible contribution for the determination of the geotherm at the inner core boundary

Ab-initio calculations performed on cobalt provided an additional confirmation of the XAS melting criterion adopted. Moreover they permitted to understand that the flattening of the oscillations in the XANES is due to the smearing of the structures in the density of the p states linked to the different environments surrounding each absorbing atom in the liquid. These calculations allowed as well to evaluate the compression of liquid cobalt at 5000 K and provided a starting radial distribution function for the analysis of the experimental Extended X-ray Absorption Fine Structure (EXAFS) extracted from the measured XAS.

The EXAFS of the liquids along the melting curve was analysed providing a measurement of the first neighbour distance in the liquid as a function of pressure for both nickel and cobalt. In the two cases our experimental results show slightly less compression than theoretically predicted. This can be interpreted as a first neighbour bond that at higher pressures is slightly more rigid than predicted or as due to an increase of 10-20 $\%$ of the coordination number. Combined to theory, our experimental observation suggests that the local structure of liquid Co and Ni increasingly deviates from a hard sphere model with P and T along the melting curve.

In conclusion, we have developed a protocol that allows validating the melting criterion for a given solid structure. In this work it has been applied to 3d metals with fcc structures and it can be applied to other structures. The presence of nickel and cobalt in the outer core of Earth was found to be irrelevant for the determination of the temperature at the ICB. XAS was shown to be an adequate technique to measure the first neighbour bond under extreme conditions, although both experiment and theory have large margin for improvement. The application of this method to more complex liquid alloys opens the way to investigation of relevant geophysical systems.

Résumé

Pour bien appréhender et comprendre les phénomènes physiques se produisant au sein du noyau terrestre externe, il est nécessaire d'étudier les propriétés structurales et thermodynamiques des matériaux liquides en présence. Ainsi, les courbes de fusion du nickel et du cobalt permettent de contraindre la température à la frontière entre les noyaux interne et externe (ICB). Cette Thèse présente l'étude de la courbe de fusion et de la structure locale du nickel et du cobalt liquide en conditions extrêmes de pression et de température. L'analyse expérimentale a été effectuée par spectroscopie d'absorption des rayons X (XAS), technique bien adaptée à l'étude de la structure locale de la matière. Des calculs *ab-initio* ont permis de valider le critère de fusion utilisé et de fournir une fonction de distribution radiale initiale pour l'analyse de la structure locale.

Les courbes de fusion du nickel et du cobalt sont déterminées à partir des mesures d'absorption et s'appuient sur un critère de fusion récemment proposé dans le cas du fer. Le critère de fusion est basé sur la disparition simultanée de l'épaulement situé au niveau du seuil d'absorption des métaux 3d et des deux premières oscillations du spectre d'absorption. Une sonde ionique focalisée (FIB) couplée à un microscope électronique à balayage (SEM) sont utilisés pour détecter *post mortem* les changements d'état de l'échantillon et confirmer ainsi le critère de fusion. Les courbes de fusion du nickel et du cobalt sont présentées jusqu'à des pressions de 1 Mbar. L'utilisation du critère de fusion est généralisable à tous les métaux $3d$. La comparaison entre les courbes de fusion du nickel et du cobalt avec celle du fer montre que la présence de ces deux matériaux dans le noyau externe de la Terre peut être négligée pour la détermination du profil de température dans la planète.

Les calculs *ab-initio* montrent que la disparition des deux premières oscillations

XANES est due au changement de densité des états électroniques p lors de la fusion et à la perte de l'ordre structural dans le liquide. Ils permettent ainsi de valider le critère de fusion empirique utilisé lors des mesures XAS et d'évaluer la compression du cobalt liquide à 5000 K en fournissant une fonction de distribution radiale initiale pour l'analyse expérimentale du spectre d'absorption.

Les oscillations EXAFS de la phase liquide du nickel et du cobalt sont analysées, permettant ainsi de déterminer la distance des premiers voisins en fonction de la pression. Les résultats expérimentaux montrent une compressibilité inférieure à celle prévue par les calculs *ab-initio*. Cette différence peut être interprétée comme une liaison atomique plus rigide entre premiers voisins ou comme une augmentation de 10 à 20% de la coordinence. Ainsi nos observations expérimentales combinées aux calculs *ab-initio* suggèrent que la structure locale du nickel et du cobalt liquide dévie du modèle des sphères rigides.

En conclusion, nous avons développé en parallèle une méthode expérimentale et un protocole théorique qui permettent de valider le critère de fusion d'une structure donnée. Nous les avons appliqués aux métaux $3d$ fcc afin de déterminer les courbes de fusion du nickel et du cobalt. La similitude entre ces courbes de fusion et celle du fer montre que la présence de cobalt et de nickel dans le noyau externe terrestre peut être négligée pour la détermination de la température au niveau de l'interface entre le noyau externe et le noyau interne de la Terre. L'étude des oscillations EXAFS des liquides à haute pression et haute température permet de déterminer la distance entre premiers voisins. Ces méthodes peuvent maintenant être appliquées à des liquides d'alliages complexes, plus pertinents pour la modélisation de phénomènes géophysiques.

Contents

Chapter 1

Introduction

This thesis uses X-ray absorption spectroscopy (XAS) to study liquid nickel and cobalt under extreme thermodynamic conditions, combining the XAS analysis with simulations of the X-ray absorption near edge structure (XANES) spectra based on ab-initio calculations. This chapter is devoted to the description of the scientific background that motivated this work. At first the two materials under analysis, nickel and cobalt, will be presented, followed by the description of the fundamental interest inspiring a study of their properties under extreme conditions. Then, the geophysical interest behind this work will be outlined.

1.1 Nickel and cobalt

Nickel and cobalt are, as iron, metals with unfilled $3d$ bands. Due to their vicinity in the periodic table, these three transition metals share similar properties. Their density of states show very similar features [106, 155] and justifies their magnetic properties. The structure of these metals is strongly influenced by magnetism which stabilizes bcc and hcp structures for iron and cobalt respectively. If magnetism is neglected, and considering only the number of $3d$ electrons, the predicted structure at ambient conditions would be hcp for iron and fcc for cobalt [122].

While iron is the main component of the Earth's core [98, 97, 2], nickel is it's major alloying constituent in the liquid outer core and cobalt is present in the same region only in minor proportions. The choice of nickel and cobalt as a case study, though, is not only justified by their presence in the Earth's interior, but also and especially by the similarity they exhibit with iron, yet being less reactive and thus easier to study.

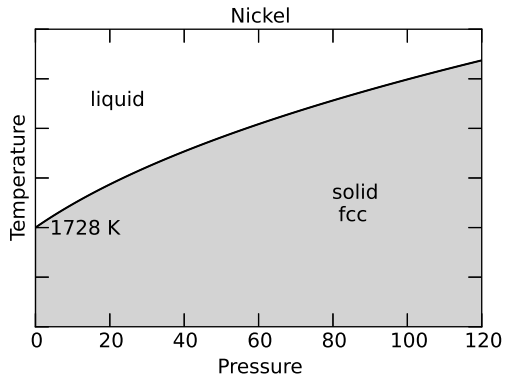

(a) Nickel phase diagram: there are no phase transitions in the solid.

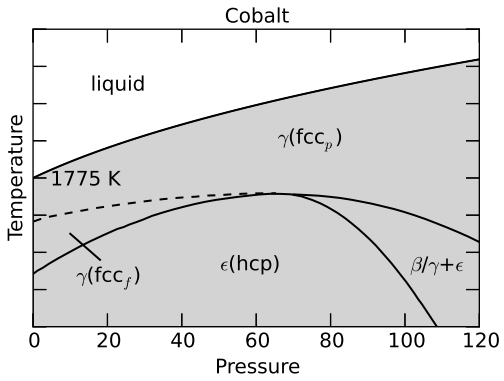

(b) Cobalt phase diagram: the structure of solid cobalt changes according to the pressure and temperature conditions.

Figure 1.1 – Pictorial representation of nickel and cobalt phase diagrams. The existent literature concerning the melting curves of nickel and cobalt is presented in Sections 3.1.1 and 3.1.2.

Nickel

According to Liu et al. [98], nickel is the third most abundant element in the outer core of Earth with a concentration of 4.68 wt.%, preceded by iron (78.78 wt.%) and oxygen (15.52 wt.%). While iron remains the primary component of the inner core (92.89 wt.%), it is proposed that nickel is the second most abundant element (5.14 wt.%) [98]. Determining these concentrations has been the subject of numerous studies [5, 4, 108, 97, 8, 72, 14], and it is widely accepted that nickel is an important alloying constituent of iron in both the Earth's inner and outer core, with a concentration of about 5-10 wt.%.

The interest in nickel, however, is not only justified by its presence in the Earth's core, but is as well due to its simplicity. With two *d* electrons more than iron, the electronic configuration of nickel is $1\mathrm{s}^2 2\mathrm{s}^2 2\mathrm{p}^6 3\mathrm{p}^6 \mathbf{3d^8} 4\mathrm{s}^2$. Unlike iron and cobalt, the phase diagram of nickel does not show any solid-solid phase transition up to 200 GPa and ambient temperature [154], and up to the melting temperatures in the 0 - 110 GPa range. In the regions experimentally probed up to now, nickel is always face centred cubic (fcc), see Figure 1.1(a).

Therefore, nickel is an attractive material to start with, allowing to lay the basis for the study of more complicated materials and alloys.

Cobalt

Cobalt is only a minor alloying constituent of iron in the Earth's outer core, with a concentration of about 0.27 wt.% [97]. Its interest, however, goes beyond its presence in our planet. Following iron in the periodic table and exhibiting a phase diagram more complicated than nickel, it plays a crucial role in the systematic understanding of melting and compression properties of 3d metals. Co and FeCo alloys also have very important technological applications. An example is magnetic recording media where strain plays an important role.

The electronic configuration of cobalt differs from the one of iron only by the presence of one extra *d* electron, that therefore is $1s^2 2s^2 2p^6 3p^6 \mathbf{3d^7} 4s^2$. At ambient conditions and for pressures up to 100 GPa and room temperature, cobalt is always hexagonal close packed (hcp), see Figure 1.1(b). After a region of coexistence, it becomes fcc at pressures higher than 150 GPa at room temperature, or at temperatures higher than 1500 K at ambient pressure. Before the transition to the liquid phase, cobalt is fcc in the explored region of the phase diagram [169, 168, 156].

1.2 Fundamental interest

In 3*d* materials such as iron, nickel and cobalt, the outer electronic shell is composed of unfilled *d* bands. The only exceptions are copper and zinc, whose *d* orbitals are filled. The number of *d* electrons in the outer electronic shell was proposed as an important factor in determining the slope of the melting curve. First measurements of the melting curves of 3*d* metals, determined using as melting criterion the visual observation of movement on the sample surface (known as "speckle" method), were in strong disagreement with the theoretically determined melting curves (this will be developed for nickel and cobalt in Section 3.1). More specifically, theoretical calculations [3] predicted that the melting temperature of transition metals should increase with pressure much faster than those determined experimentally with the "speckle" method, where the melting slopes were characterized by a $\mathrm{dT/dP} \sim 0$ [92, 25, 51, 78, 24, 50].

A semiempirical model [135] was developed to explain the reason of the low melting slopes, showing good consistency with the experimental data obtained for iron, nickel and cobalt [78]. The model predicts that in the case of unfilled *d* band, the transition to the liquid phase, and thus the loss of structural periodicity, is associated to a broadening of the liquid DOS [45, 85, 86] and to an increased stability of the liquid with respect to the solid. According to this model the melting curve steepness is

thus directly linked to the number of *d* electrons, leading to low melting slopes in the case of partially filled *d* electron bands.

Moreover, it is known that the *d* orbitals, unlike the spherically shaped *s* orbitals, are directional. And it was proposed that in transition metals with strong directional bonding induced by incomplete *d* bands, Peierls-Jahn-Teller distortions in the liquid would remove the degeneracy of levels and thus the formation of localized bonds would stabilize the system lowering the energy [133]. The presence of *d*-electron bonding, moreover, matches well with the presence of icosahedral structures in a liquid [64, 140, 95] (this will be developed in Section 5.1). The icosahedral structures in liquids of early transition metals, however, are more distorted than the ones of late transition metals, due to the different number of electrons in the *d*-bands [133, 134]. The compression of *d*-metals in a liquid could thus produce interesting non-uniform effects, dependent on the number of *d*-electrons, that could influence the local structure.

The "speckle" method that gave rise to these interpretations, however, was questioned by more recent X-ray diffraction studies [37, 40, 9] (this will also be developed in Section 3.1), thus leaving uncertain the role of *d*-electrons in the slope of the melting curves and in the study of the local structure.

1.3 Geophysical interest

The deepest point that mankind was able to access is at 12.276 km, and it was reached by drilling a borehole on the Kola Peninsula in Russia from 1970 to 1989 [1] [1]. All other information we have about the Earth's interior originates from indirect observations. These form the basis for our present Earth models. The Earth models can be divided in three interconnected categories: seismological, compositional and thermal [125].

Seismic events, e.g. earthquakes, are documented, and the study of seismic waves propagation and normal mode oscillation allows to formulate seismological models. The Earth's interior is thus described in terms of wave velocity, density, pressure and elastic moduli as a function of the depth. Using the density profile in the Earth's interior and the velocity profiles of the seismic waves, it is possible to formulate compositional models, which describe the composition of the Earth at different depths.

1. Longer boreholes have been drilled since then in Qatar, in 2008, and on the Russian island Sakhalin, in 2011 [1], but the borehole on the Kola Peninsula is still the one that reached the deepest artificial point inside the Earth.

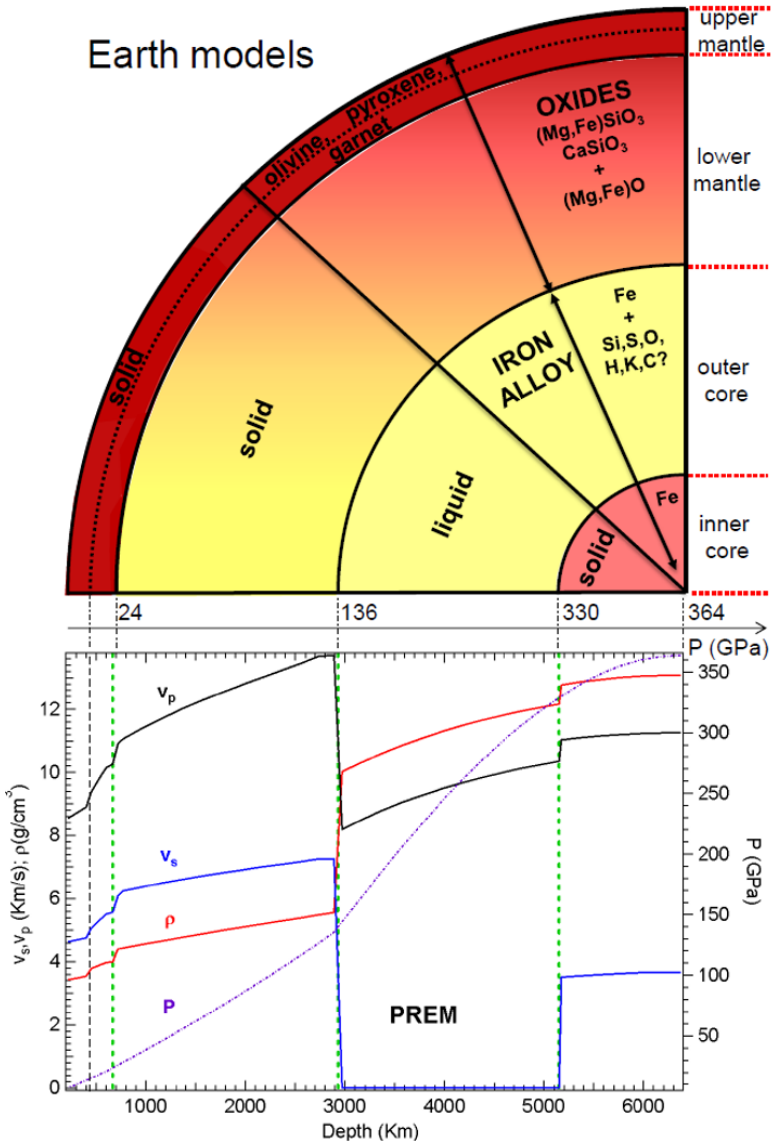

Figure 1.2 – Schematic representation of the Earth's interior [10]. Top panel: the compositional model of the Earth at different depths is represented. The three main shells are highlighted, with their believed composition and the pressure at the boundary separating them. Bottom panel: the PREM data of seismic velocities (relative to longitudinal v_p - black solid line - and transverse v_s - blue solid lines - seismic waves), density - red solid line - and pressure - purple dotted line - are represented as a function of the depth.

Compositional models are not only formulated on the basis of seismologically observed densities and sound velocities in the Earth's interior [20, 109, 29], but they also merge information obtained from compositional studies of meteorites, which are testimony of the building blocks of the early solar system [28, 125], and deductions formulated to describe the origin of Earth's magnetic field [147, 110].

Finally, the thermal models depend on thermodynamic parameters inferred by geomagnetic variations or observations of the heat flux [80]. However, the temperature profile in the Earth (called geotherm), influences and is as well influenced by the compositional models, showing that the three models are interdependent.

In 1923, Williamson and Adams [166] derived the density of the Earth as a function of depth, by assuming a spherically symmetric Earth in hydrostatic equilibrium and considering adiabatic compression. Hypothesizing that the Earth was made of those materials that compose the crust, they estimated the variation of density solely due to compression. Independently, they could derive a density profile inside the Earth from the velocity of longitudinal ($\mathrm{v_p}$) and transverse ($\mathrm{v_s}$) seismic waves.

Comparing the density profiles obtained in these two ways, Williamson and Adams realized that the high density in the Earth's core could not be explained by compression alone. The high density could however be justified by assuming, in the core, the presence of some metals, which are heavier than the materials composing the crust. Observations of metal abundances in meteorites indicated that iron and nickel ($\sim$5%) could be good candidates [5]. However, the iron/nickel mixture is too dense and for this reason the presence of 7-8% of light impurities such as S, Si, O and C was proposed [4, 2, 175].

In 1981, a first model describing the average properties of Earth as a function of the radius was conceived. It is called Preliminary Reference Earth Model (PREM) [47] and its results are summarized in Figure 1.2. As depicted in Figure 1.2, the absence of the shear velocities of seismic waves between 3000 and 5000 km of depth suggests the presence of a liquid outer core. The shear waves cannot be supported by fluids as their direction of oscillation is in a plane orthogonal to their propagation direction.

As proposed by Williamson and Adams, the sudden increase in the density at the mantle core boundary (MCB) indicates a variation of composition between the mantle and the core. If Williamson's and Adams' explanation of this density change being due to the presence of metal is true, this would account not only for the Earth's density profile, but this would also explain the presence of our terrestrial magnetic field. The geomagnetic field can in fact be explained by the presence of a metal such as iron in the liquid region inside the Earth [110].

Another density discontinuity is found at the boundary between the inner and outer core, i.e. the inner core boundary (ICB). This discontinuity cannot solely be explained by the liquid-solid transition density change, but it must be caused by the partition of light impurities between solid and liquid. While estimates of the density in the inner core are consistent with pure iron, in the outer core there could be light impurities as well [2].

As the Earth cools down, light impurities are expelled in the liquid region, and due to their density - lower than the one of iron - they would move further away from the inner core thus driving the convective currents in the liquid part of the core [30]. Also the latent heat released in the crystallization process of the inner core contributes to convection movements. The motion of liquid iron in the outer core, which is hence driven by compositional and thermal convection, is known as geodynamo and it is believed to be the mechanism generating the Earth's magnetic field.

Understanding the Earth's core is important for several reasons. Firstly, the determination of the geotherm, i.e. the temperature profile inside our planet, is essential for understanding the cooling dynamics of the Earth and the convection that takes place in the outer core. In the hypothesis of a liquid in turbulent convection [2], the distribution of the temperature in the core follows an adiabat. At the ICB the geotherm crosses the melting curve of the materials composing the core, see Figure 1.3. Since the pressure of the ICB, where the two curves intersect, is known, the melting curve would provide a fixed point for the temperature profile inside the Earth. For this reason, knowledge of the temperature in the core, combined with precise understanding on how melting temperatures of Fe-rich systems vary with pressure and composition, would allow to better constrain the identities and abundances of light elements in the Earth's core [59].

Many efforts have already been made towards determining the geotherm [79, 72, 7, 159, 113](and references within), and even if the discrepancies among methods of investigations (described in Section 3.1) and melting temperatures of core materials at the ICB pressure are decreasing in the past years [72, 91], uncertainties still exist.

Moreover, determining the physical properties of metals alloyed with light elements at extreme pressure and temperature conditions is very important for the understanding the characteristics of the molten outer core. The dynamics of the core are in fact largely influenced by its density, viscosity and thermal conductivity [152]. Due to significant experimental challenges, complete studies on the experimental determination of structural properties of liquid metals and alloys under extreme conditions of pressure and temperature started to develop only recently. First measure-

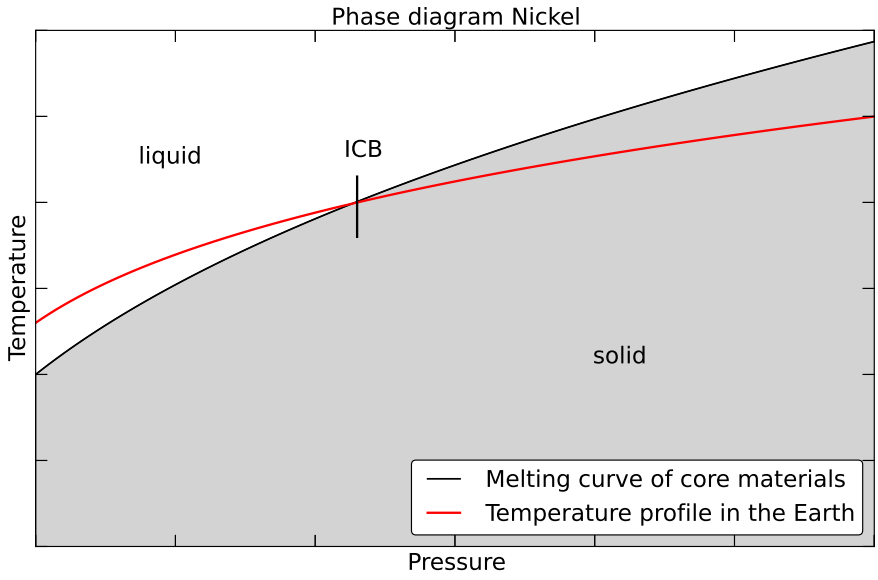

Figure 1.3 – Pictorial representation of the temperature profile at the inner core boundary, i.e. at the boundary between the liquid and the solid core. The melting temperature of core materials at the ICB pressure provides an anchoring point for the determination of the geotherm, i.e. the temperature profile in the Earth.

ments on the equation of state of liquid iron [6, 141] and iron alloyed with light elements such as FeS [138, 117, 33], FeNiS [114], FeSi [170, 136], FeNiSi [114] and FeC [151, 139, 142] were performed. X-ray absorption spectroscopy was used up to about 10 GPa, while at higher pressure, up to about 95 GPa, the analysis was performed on liquid diffuse scattering signal [152]. The findings of these works are that the presence of sulphur reduces the density and the bulk modulus of pure liquid iron. Carbon was found to affect iron in the same direction, but the reduction in density and bulk modulus is more moderate. The presence of silicon instead reduces slightly the density but has almost no effect on the bulk modulus.

The use of X-ray absorption spectroscopy, known for its elemental selectivity, at more extreme pressure and temperature conditions than before, would enable to probe the local structure of the different elements in the alloy and it might help understanding how these light elements affect the local structure of iron.

1.4 Conclusions

In the following chapters we propose to validate a method based on X-ray absorption spectroscopy to investigate the transition from solid to liquid phase of $3d$

metals under extreme thermodynamic conditions. The aim is not only verifying or questioning the experimental evidence that gave rise to the semiempirical models connecting the number of *d* electrons to the slope of the melting curves, but also to lay the foundations for future studies on more complex systems such as Fe (more reactive than nickel or cobalt), FeNi, FeCo, FeO, FeC, FeS, NiS, FeNiS, FeMgO etc.. X-ray absorption spectroscopy currently allows to reach about 130 GPa and 4000 K, i.e. the conditions of the lower mantle, close to the mantle core boundary (MCB) at 136 GPa and 4000 K. The long-term objective will be to improve the experimental techniques so that conditions in the Earth's core, up to about 360 GPa and 6500 K, can be directly investigated.

Furthermore in order to unravel the effects of the directional *d* orbitals in a liquid upon increasing pressure and to continue in the direction of determining the equation of states of core components, we propose a method to study the variation of the bond length of the liquid as a function of pressure. Results of the analysis of the local structure of liquid nickel and cobalt under pressure are shown. Once the method has been established for relatively simple materials and at the pressures that are nowadays accessible, it will be possible to apply the same method to more complicated systems and at pressures closer to the inner core boundary.

Chapter 2

Experimental methods

Thanks to its short order sensitivity and its elemental selectivity X-ray absorption spectroscopy (XAS) is a suitable technique to study local structure in liquids. In this chapter XAS is presented in its near edge and extended regions. The in-situ experiments in this work were all performed at the energy dispersive X-ray absorption spectroscopy (EDXAS) beamline ID24 of the European Synchrotron Radiation Facility (ESRF) in Grenoble, France. The beamline is described here, with particular attention to those aspects crucial for the success of these experiments. The attention is then focused on high pressure and high temperature methods used to approach the conditions of the Earth's outer core. In this chapter is presented how XAS, high pressure and high temperature are combined in the experiments. Finally, the technique used for ex-situ post analysis is presented.

2.1 X-ray Absorption Spectroscopy

X-ray Absorption Spectroscopy is a powerful technique used to probe the local structure of a selected element in a material. It is used to study solid matter, in crystalline or amorphous form, liquid matter and molecular gases [31].

The physical quantity measured is the absorption coefficient. It describes the probability of an incident photon to be absorbed as a function of the incident photon energy. The absorption coefficient μ can be calculated from the Lambert-Beer law

$$\mathrm{I} = \mathrm{I}_0 \mathrm{e}^{-\mu \mathrm{x}}$$

as

$$\mu(\mathrm{E})\mathrm{x} = \ln \frac{\mathrm{I}_0}{\mathrm{I}},$$

where x is the thickness of the sample, I_0 is the intensity of the probing X-rays without the sample and I is the intensity transmitted by the sample.

The absorption coefficient is normally a smooth function of the energy $\mu(E) \sim 1/E^3$, where E is the energy of the incoming radiation. In the hard X-ray range however the absorption coefficient is mainly determined by core-electron excitations. These give absorption edges in correspondence of the core binding energies that are thus characteristic of the elements present in the sample. The absorption edges are followed by characteristic oscillations that depend on the environment of the atom that absorbed the radiation.

When an X-ray photon with an energy E_X equal or greater than the binding energy E_0 impinges on the sample and is absorbed, it generates a photoelectron whose energy is given by $E_{ph} = E_X - E_0$. This photoelectron can, to a first approximation, be considered as a wave which diffuses from the absorbing atom and scatters from the surrounding atoms, see Figure 2.1(a). The backscattered wavelets interfere with the outgoing wave. This interference, at the origin, modulates the absorption probability beyond the edge, giving rise to the oscillations observed as a function of energy in the absorption coefficient, see Figure 2.1(b).

X-ray absorption is a quantum mechanical phenomenon [31]. The discussion that follows is in the framework of a semiclassical [1] nonrelativistic approximation. In the first order approximation of the time dependent perturbation theory, the transition rate W_{if}, and thus the absorption coefficient, is proportional to the square modulus of the perturbation matrix element between the final and the initial state multiplied by the density of states at the transition frequency. This is known as Fermi's golden rule

$$W_{if} = \frac{2\pi}{\hbar} | < \Psi_f | \hat{H}_I | \Psi_i > |^2 \rho$$

where Ψ_i and Ψ_f are the initial and final states respectively, including all the electrons of the absorber atom involved, $\hat{H}_I$ is the interaction Hamiltonian and ρ is the density of states compatible with energy conservation $E_f = E_i + \hbar\omega$. The Hamiltonian $\hat{H}_I = -\frac{e\vec{A}\cdot\vec{p}}{m_e}$ describes the interaction between the X-ray electromagnetic field and the electrons. Where $\vec{p}$ is the momentum operator of the electron and $\vec{A}$ is the vector potential of the electromagnetic wave that, in the case of a linearly polarized (in the direction $\hat{\epsilon}$) monochromatic plane wave, can be expressed as $\vec{A} = A_0 \hat{\epsilon} \cos(\vec{k}\cdot\vec{r} - \omega t)$. The absorption coefficient is then proportional to:

$$\mu(E) \propto | < \Psi_f | \hat{\epsilon}\cdot\vec{p}\, e^{i\vec{k}\cdot\vec{r}} | \Psi_i > |^2 \rho(\hbar\omega - (E_f - E_i)). \tag{2.1}$$

1. The X-ray electromagnetic wave is considered as a classical field.

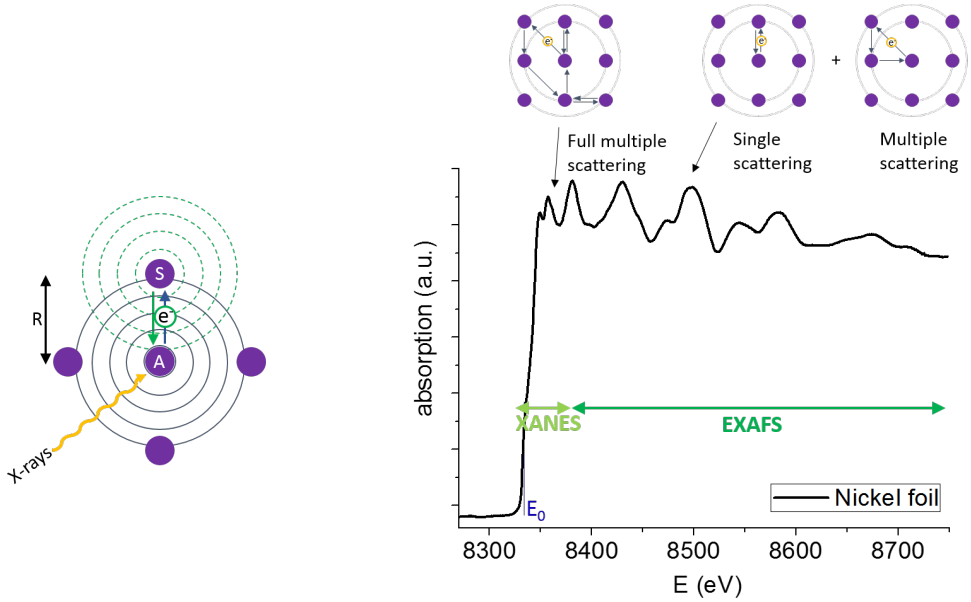

(a) Schematic of the X-ray absorpdion process, where A is the absorber atom and S the scatterer.

(b) Representation of a XAS spectrum. The XANES part is dominated by a large number of multiple scattering processes, while the EXAFS part is instead dominated by single scattering, or by multiple scattering with three or four atoms.

Figure 2.1 – Schematic of the XAS process and representation of an absorption spectrum.

The initial and final wavefuctions Ψ_{i} and Ψ_{f} are given by the contribution of the wavefunctions of all the electrons in the atom. Only one electron is photoemitted, all the others that do not interact directly with the perturbation can be assembled in the term S_0^2. The value of this parameter is normally between 0.75 and 1, taking into account the relaxation of the non interacting electrons. In the dipole approximation and using the commutation relations with the interaction Hamiltonian (see Appendix A for the derivation), Equation 2.1 can be written as

$$\mu(\mathrm{E}) \propto \mathrm{S}_0^2 | < \psi_{\mathrm{f}} | \hat{\epsilon} \cdot \vec{\mathrm{r}} | \psi_{\mathrm{i}} > |^2 \rho(\hbar\omega - (\mathrm{E}_{\mathrm{f}} - \mathrm{E}_{\mathrm{i}})), \tag{2.2}$$

where in the initial state the electron is a core electron described by the wavefunction ψ_{i}, the final state it is a photoemitted electron described by ψ_{f}. The photoabsorption many-body problem is thus reduced to the problem of one electron moving in an effective optical potential.

The final wavefunction of the photoemitted electron can be written as the sum of the outgoing and the incoming scattered wavefunction: $|\psi_{\mathrm{f}}> = |\psi_{\mathrm{f}}^0 + \delta\psi_{\mathrm{f}}>$. If the atom is isolated there is no backscattering and $\delta\psi_{\mathrm{f}} = 0$. The absorption coefficient of the isolated atom $\mu_0(\mathrm{E})$ is thus calculated considering just the outgoing part of wavefunction. In the case of condensed matter the expression for the $\mu(\mathrm{E})$ is more complicated, but since the initial state is strongly localized on the absorber atom, the relevant part of the final state wavefunction for the matrix element will be localized on the core electron.

The absorption spectrum can be divided in two energy ranges, the X-ray Absorption Near Edge Structure (XANES) describing the region closer to the edge and the Extended X-ray Absorption Fine Structure (EXAFS) describing the oscillations about 50 eV after the edge, see Figure 2.1(b).

2.1.1 X-ray Absorption Near Edge Structure (XANES)

The interpretation of the XANES part of the spectrum is complex and several approaches known as scattering, Green's function and band structure approach have been proposed [116]. In the one-electron approximation, though, the three of them are basically equivalent and they differ only for their formalism. According to the problem to be solved, the more suitable can be chosen. Here it is worth citing that the interpretation of the XANES can be based on the real space or the reciprocal space.

If the real space is considered, when the energy of the photoelectron is small, approximatively less than 30-50 eV, the mean free path is large and the photoelectron is involved in multiple scattering processes with a large number of atoms, see Fig-

ure 2.1(b). In this region it is generally very difficult to keep a track of the path travelled. Due to the complexity of the processes involved extracting structural parameters from the shape of the XANES is possible in the framework of multiple scattering calculations, but is not straightforward. The inverse problem, where the experimental spectra are qualitatively compared with simulations, is instead widely used and is a part of this work. The procedure adopted to simulate the spectra is presented in Section 4.2.3.

In the reciprocal space interpretation, the probability of absorption in the near edge region is strongly influenced by the density of states just above the Fermi level. In the case of a K edge the final states allowed for the dipole selection rules are the p-states. As a result the shape of the near edge region of the spectrum reflects the shape of the *p* empty states.

This region of the X-ray absorption spectrum contains information about the oxidation state of the absorber and about its chemical speciation. Changes in the XANES are adopted in this work as criterion to determine when the sample measured is solid or liquid. More information will be provided in Section 3.2.

2.1.2 Extended X-ray Absorption Fine Structure (EXAFS)

The region of the absorption spectrum corresponding to an energy of the photoelectron larger than $\sim$ 50 eV is called Extended X-ray Absorption Fine Structure (EXAFS). In this region the mean free path is small (few Angstroms) and thus the photoelectron can only undergo very few scattering events before losing its energy. If the photoelectron loses its energy in a scattering event it means that the scattered wave does not interfere with the outgoing wave and the information is lost. EXAFS is thus dominated by single scattering and few multiple scattering processes. The information contained here is about the local structure around the absorber, the number and type of neighbours and their disorder.

Subtracting from the general absorption coefficient the contribution of the isolated atom it is possible to isolate and extract only the information about the environment. The EXAFS signal is then obtained as

$$\chi(\mathrm{k}) = \frac{\mu(\mathrm{E}) - \mu_0(\mathrm{E})}{\mu_0(\mathrm{E})}. \tag{2.3}$$

where the wavevector k is

$$\mathrm{k} = \frac{\sqrt{2\mathrm{m}(\mathrm{E_X} - \mathrm{E}_0)}}{\hbar}.$$

In the description of a crystalline solid at sufficiently low temperatures, the radial distribution function, which is the probability of finding an atom at distance r from

the absorber, can be represented as a Gaussian radial distribution function. The EXAFS signal can thus be written as the sum of scattering contributions (or paths)

$$\chi(\mathrm{k}) = \mathrm{S}_0^2 \sum_{\mathrm{i}} \mathrm{N}_\mathrm{i} \frac{\mathrm{f}_\mathrm{i}(\mathrm{k},\pi)}{\mathrm{kR}_\mathrm{i}^2} \mathrm{e}^{\frac{-2\mathrm{R}_\mathrm{i}}{\lambda(\mathrm{k})}} \mathrm{e}^{-2\mathrm{k}^2\sigma_\mathrm{i}^2} \sin(2\mathrm{kR}_\mathrm{i} + \delta_\mathrm{i}(\mathrm{k})) \tag{2.4}$$

where in the case of single scattering N_i is the number of equal atoms at the same distance R_i from the absorbing atom, and σ_i^2 is the variance of the Gaussian describing the radial distribution function, also known as mean square relative displacement or Debye-Waller factor. The amplitude $\mathrm{f}_\mathrm{i}(\mathrm{k})$ and the phase $\delta_\mathrm{i}(\mathrm{k})$ are due to the scattering, they are respectively the backscattering amplitude and the phase shift function. In a muffin tin potential approximation $\delta_\mathrm{i}(\mathrm{k})$ is given by the phase shift that takes place when the photoelectron crosses the edge between the spherically symmetric potential around the atoms and the interstitial region where the potential is constant.

Equation 2.4 can be generalized to include MS paths. In this case N_i is the number of identical paths, R_i is half the total path length [2], and f_i and δ_i are the effective scattering amplitude and phase respectively.

The two exponentials cause a damping of the signal due to the mean free path $\lambda(\mathrm{k})$, related to the core-hole lifetime and the inelastic scattering, and due to the thermal and static disorder considered in σ^2. The sinusoidal term $\sum_\mathrm{i} \sin(2\mathrm{kR}_\mathrm{i})$ is the one that modulates the constructive or destructive interference. The distance appears as a frequency and it can be extracted performing a Fourier transform.

The Fourier transform is thus characterized by peaks in correspondence of the leading frequencies of the EXAFS signal [63], and by fitting these peaks it is possible to obtain information about the position, static and thermal disorder and coordination number of the different atomic shells. The Gaussian shell model here presented though, is appropriate to describe only crystalline solids at low temperature, when both the thermal and the static disorder are negligible.

Already at higher temperature it is required to go beyond the harmonic approximation and to describe the atomic positions using more sophisticated models or in the cumulant expansion approach [62, 21]; therefore Equation 2.4 is no longer valid. In the cumulant expansion approach dynamic and, to a certain extent, static disorder are taken into account in the mean square relative displacement σ^2. Moreover the asymmetry of the peaks in the radial distribution function due to the anharmonic potential is considered into the third cumulant.

In the case of a liquid, where the configurational disorder is significant, the radial

2. In case of multiple scattering involving the three atoms A (the photoabsorber), B (first scatterer) and C (second scatterer), half of the total path length will be $\mathrm{R}_\mathrm{ABC} = (\mathrm{d}_\mathrm{AB} + \mathrm{d}_\mathrm{BC} + \mathrm{d}_\mathrm{CA})/2$, where d is the distance between two atoms.

distribution function cannot be described as constituted by separate peaks associated to different atomic shells. While analysing the structure of a liquid an entirely different approach is required, and it will be shown in Section 5.3.

2.2 The energy dispersive beamline ID24

The energy dispersive X-ray absorption spectroscopy (EDXAS) beamline ID24 was designed for time resolved and extreme condition experiments, where time-resolution, high flux and small focal spot are required [120].

The most important optical element in the dispersive geometry is the polychromator - an elliptically bent Si(111) crystal - whose function is to create an angular correlation of the X-ray photons' energy and to focus the beam horizontally on the sample. The beam is then transmitted by the sample and detected on a position sensitive detector where the energy is correlated to the position. In this way the entire XAS spectrum is simultaneously collected ensuring fast data collection.

The beamline is designed in two branches called S and L, see Figure 2.2, dedicated to high pressure and chemistry respectively. The branch used for this work is the first one, where a smaller beam can be obtained and where the laser heating setup for the high temperatures is placed.

In the following, a more detailed description of the beamline from the X-ray beam generation to its detection will be provided for the S branch. The ID24 source is located on a 6 m-long straight section of the storage ring [120] and is composed of a sequence of 27 mm (U27) and 32 mm (U32) period undulators whose combination allows to span an energy range between 5 and 28 keV. The gap of the undulators is chosen according to the required energy and their tapering allows to obtain a homogeneous flux over an energy bandwidth of about $\sim$1 keV at 7 keV. Energy dispersive XAS beamlines are usually installed on bending magnet sources. In this way the large horizontal divergence necessary to obtain an energy dispersion ΔE able to cover a whole EXAFS spectrum is already naturally provided. Nevertheless installing a EDXAS beamline on an undulator source offers some advantages as well [121]. The first one is the possibility of matching the bandwidth of emission of the undulator and the acceptance of the polychromator by optimizing the gap, the taper and the radius of curvature of the polychromator crystal, that results in a reduction of heat load on the optics. Then there is a substantial reduction of unwanted harmonics. Finally an undulator provides higher brightness, lower vertical angular divergence and low monochromatic horizontal and vertical divergences.

The beam generated by the undulators is a pink beam around the designated en-

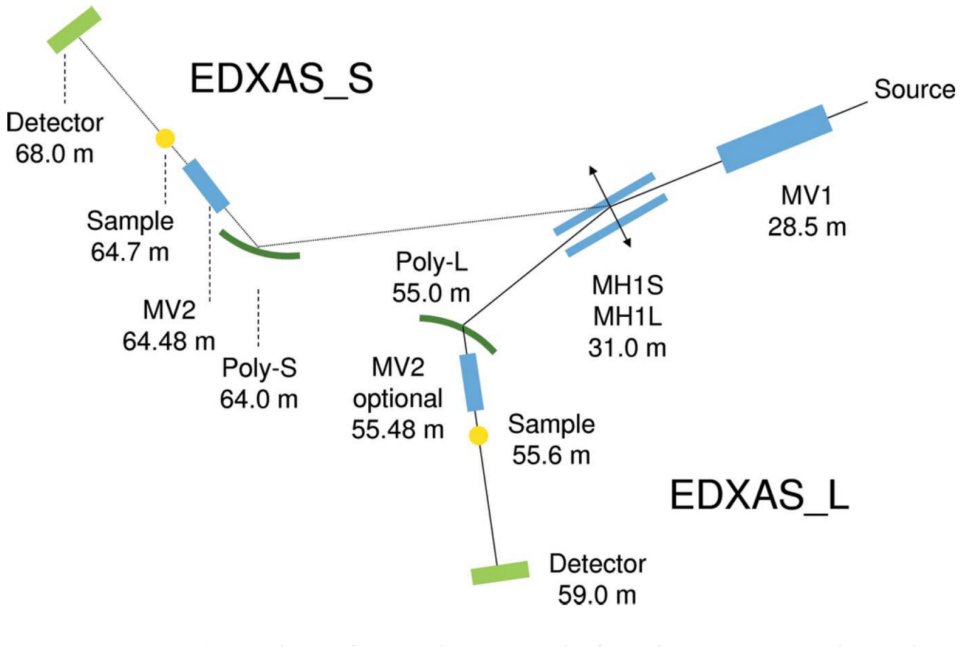

Figure 2.2 – The two branches of the beamline ID24 are here schematized. Mirrors are in blue (MH is a mirror for horizontal focalization, MV for vertical one), polychromators are in green, sample positions in yellow and detectors in light green. The branch used for the experiments in this work is EDXAS_S.

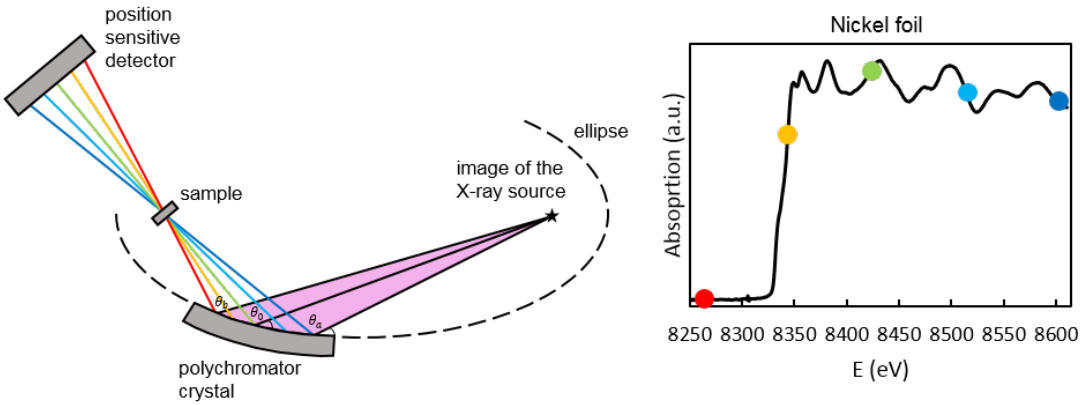

Figure 2.3 – Schematic of the principle of operation of the polychromator on ID24 [120], where the image of the X-ray source is the one projected by MH1S. In the right panel is represented an absorption spectrum of a nickel foil placed in the sample position.

ergy. The first optical elements encountered by this beam are a pair of mirrors (MV1 and MH1) in a Kirkpatrick-Baez configuration. The mirror for vertical focusing (MV1) focalizes at 58 m from the source, see Figure 2.2. The mirror for horizontal focusing (MH1) allows both to choose the branch and to transform the collimated pink beam coming from the undulators into a diverging beam in the horizontal plane. The beam is horizontally focused at about 33 m from the source, in the position of the focus of the imaginary ellipse on which the elliptically bent polychromator lies, and then diverges until it hits the polychromator, see Figure 2.3. The idea is to maximize the footprint of the beam on the polychromator that in this way collects the pink X-ray beam at different angles. Following Bragg's law $2\mathrm{d}\sin(\theta) = \lambda = \mathrm{ch}/\mathrm{E}$, different energies are reflected in different positions of the crystal, where d is the spacing between the (111) planes in the silicon crystal, θ is the angle between the beam and the crystal, λ is the wavelength of the beam and E its energy, c and h are the speed of light and Planck's constant respectively. Note that, as schematized in Figure 2.3 at smaller incidence angles correspond a higher energy and *vice versa*. The full spectral range diffracted by the polychromator can be expressed as

$$\Delta\mathrm{E} = \mathrm{E}_0 \Delta\theta \cot\theta \tag{2.5}$$

which means that it increases with the energy and, in the case of ID24_S is ∼1 keV at 8 keV.

After being dispersed and focused horizontally the X-ray beam can be focused again vertically by means of a second mirror (MV2). Note that the function of the

mirrors is not only to focus and direct the beam, but also to reject harmonics. The beam converges to a focal point, where at 7 keV the resulting beam size can be of $\sim$4x4 μm^2. The size of the beam is determined performing knife-edge scans on a vertical and horizontal blade. A fit of the resulting intensity to a step function convoluted with a Gaussian; the FWHM of the Gaussian gives the FWHM size of the beam. At higher energies the X-ray beam penetrates more into the bended polychromator crystal; part of the beam is thus diffracted by a region of the crystal with a different lattice parameter. This results in a larger beam, up to $\sim$7x7 μm^2 with a tail of about 10 μm at 13 keV. When all the optical elements of the beamline have been aligned and both the polychromator crystal and the MV2 are bended in order to optimize the X-ray beam size, the sample is positioned in the focal point. The beam transmitted by the sample diverges again towards a position sensitive detector, a FReLoN camera with an Hamamatsu chip [82], where the energy is correlated to the position through a calibration with a standard reference. In Figure 2.3 it is clear that different energies reach the detector in different positions, thus allowing the collection of a whole XAS spectrum in a single acquisition.

The XAS spectrum is then obtained as $\mu(\mathrm{E})\mathrm{x} = \ln(\mathrm{I}_0/\mathrm{I}_1)$, where x is the thickness of the sample, and I_0 and I_1 are the X-ray intensities (as a function of the energy) measured on the same detector in different moments in the absence and in the presence of the sample respectively.

In the energy range of interest for this work, which is between 7 and 9 keV, the energy resolution $\delta\mathrm{E}/\mathrm{E}$ is less than 2x10^{-4} and the photon flux is $\geq$1.5x10^{14} photons/s.

In conclusion, in the dispersive setup an absorption spectrum can be visualized in real time on a position sensitive detector in its whole energy range. The micro-beam and the fast readout are particularly convenient for the experiments performed in this work. A reduced size of the beam permits to probe smaller samples thus to reach more extreme conditions and a fast readout allows to reduce the sample exposure to the laser thus lowering the probability of reactions, as illustrated later in this chapter.

2.3 Sample

In this work pure nickel and cobalt were measured.

The nickel sample is a 4 μm thick polycrystalline nickel foil 99.95% pure from Goodfellow. The size of the larger grains is less then 2 μm.

The cobalt sample is a 4 μm deposition 99.95% pure provided by E. Monsifrot [3].

3. Eric Monsifrot, DEPHIS, Etupes, France.

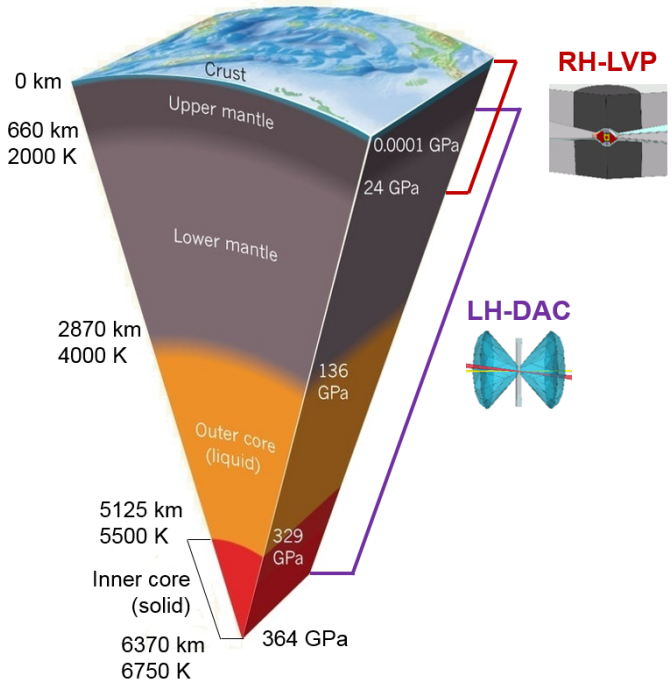

Figure 2.4 – Schematic of the Earth's interior, with the two static high pressure techniques that can be used for its investigation. RH-LVP stands for resistively heated large volume press (picture from [132]) and LH-DAC is laser heated diamond anvil cell. The pressures for the Earth's interior reported here are the ones proposed by the PREM model [47]. The temperatures are the ones proposed by Andrault et al. [7].

2.4 High pressure

In order to reproduce the conditions of Earth's interior it is necessary to study samples under high pressure. Different techniques can be used according to the conditions that have to be reached. In Figure 2.4 are indicated the ranges of operation for the two most common static high pressure techniques used to probe Earth's interior: resistively heated large volume press (RHLVP) and laser heated diamond anvil cell (LH-DAC). The main purpose of this thesis is to probe materials in the region of the liquid outer core, for this reason we used a laser heated diamond anvil cell. With this technique it is in principle possible to reach pressures up to 200 GPa and 6000 K [149, 148, 150], but when it is coupled to X-ray absorption on the ID24 beamline at the ESRF, due to the present X-ray beam size, the conditions that can be reached are only up to 130 GPa and 4000 K.

2.4.1 Diamond Anvil Cell

In a diamond anvil cell (DAC) the sample is compressed between two diamonds (of about 1/3 carats), whose tip, called culet, has been machined in order to be flat and parallel to the table, as shown in the top part of Figure 2.5(b). The two diamonds are glued on two separate parts of a cell that are called piston and cylinder. In this work we used membrane DACs with Le Toullec design [96], see Figure 2.5(a). The piston side is characterized by four pistons that are designed to slide into the four cylinders in the cylinder side in a way that drives the two anvils to face one another. A rocker and a small translation of the diamond seats allow a very fine alignment of the two anvils that have to be perfectly concentric and parallel.

The pressure is defined as $\mathrm{P} = \frac{\mathrm{F}}{\mathrm{S}}$, where F is a force and S is a surface where the force is applied. This means that the smaller the culet of the diamond, the higher the pressure that can be reached. The pressure on the sample is therefore given by a force applied on the surface of the culet. In membrane cells, like the ones with the Le Toullec design, the force is transmitted from the expansion of the membrane, which is filled with helium through the capillary, to the back of the diamond and then from the back of the diamond to its tip. Some of the force is lost due to the deformation of the diamonds (even though it is the hardest known natural material) and the other components of the DAC.

Diamonds

Due to their hardness and their transparency over a wide range of wavelengths, diamonds are the most suitable anvils for high pressure experiments performed with spectroscopy - such as Raman, infrared spectroscopy and X-ray absorption - and X-ray diffraction.

In this work we used two different kinds of diamonds: single crystal and nano-polycrystalline, see Figure 2.5(b). The single crystal diamonds, synthesized with a multi anvil large volume pressure at 9 GPa and 1600 K [118], are transparent in the visible range but during X-ray absorption experiments it often happens that, in the range of energy probed, photon intensity at specific energies is lost due to Bragg scattering, this results in a large deformation (glitches) of the XAS spectrum. Those glitches can be moved at different energies by rotating the DAC, but sometimes it is very difficult to eliminate them completely. The nano-polycrystalline diamonds (NPD), instead, are composed of nano-sized crystalline grains oriented randomly [74]. NPD diamonds prevent the appearance of Bragg peaks in the spectrum, see Figure 2.5(b), thus allowing to record good quality EXAFS data over a wider range

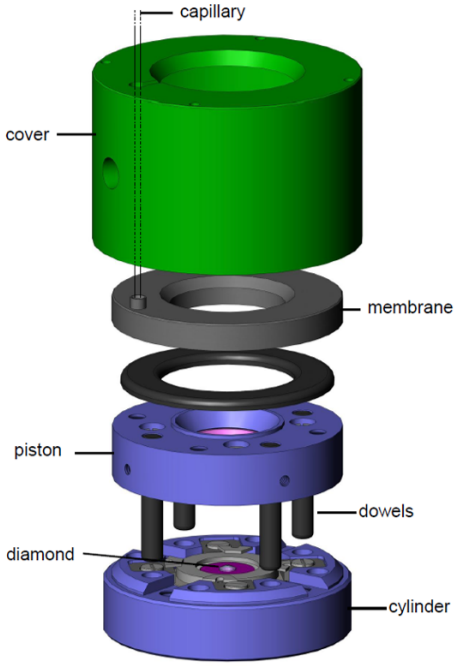

(a) Schematic of a membrane high pressure cell [10] with Le Toullec design [96].

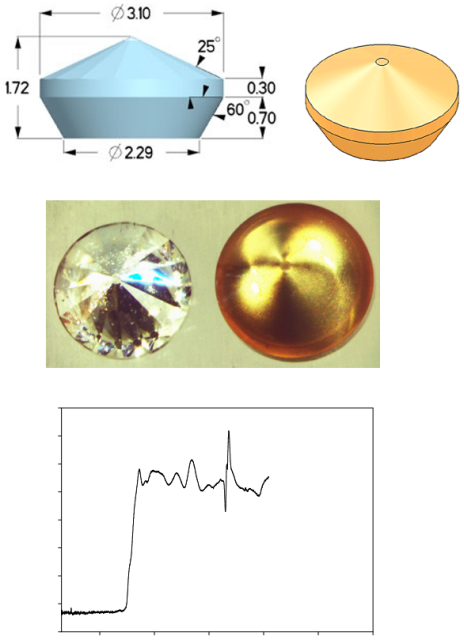

(b) Top: Schematic of Boehler-Almax diamonds [48]. Middle: picture of single crystal and nano-crystalline diamonds. Bottom: Bragg diffraction of a single crystal diamond affecting the XAS spectrum [74].

Figure 2.5 – Components of a membrane diamond anvil cell.

[75].

The diamonds used for this study have Boheler-Almax design [26], which allows a mechanical stability superior to the one achievable with conventional (flat) diamonds. This is due to the optimized mechanical support for the anvil's crown section which matches perfectly with the seats. Moreover the Boheler-Almax design allows the use of thinner diamonds, thus reducing the X-ray beam absorption, and the use of seats with larger angular aperture (typically 70 deg for the DACs used in experiments during this work), thus allowing more flexibility in the experimental setup. This last point will be clearer in Section 2.5.1.

Gasket and pressure transmitting medium

The sample is embedded in a softer material, called pressure transmitting medium (PTM), and both are placed in a chamber drilled in a gasket, see Figure 2.6. The gasket is a metallic foil typically 200 μm thick. To increase its hardness the gasket is normally pre-compressed between the two diamonds to a pressure of about 30 GPa. During this procedure, called pre-indentation, the material deforms plastically and is extruded outside the anvils [46]. The thickness between the two diamonds culets will be about 25-45 μm and outside the anvils it will be greater than the original thickness. A cylindrical hole is then drilled in the thin part of the gasket, to create the sample chamber, whose diameter is normally between 1/2 and 1/3 of the diamond culet. Here the sample is embedded in the pressure transmitting medium that can be a gas, a liquid or a solid. In this configuration the uniaxial pressure provided by the diamonds is transformed to an hydrostatic (or quasi-hydrostatic) pressure thanks to the PTM and the resistance provided by the outer part of the gasket beyond the diamond culets [46].

The properties of gaseous, liquid or solid pressure transmitting media are very different. In particular the hydrostatic limit, i.e. the pressure at which the PTM is still hydrostatic, can vary considerably according to the phase of the PTM [123]. Gases are the most hydrostatic ones, among which He is the best. It has been recently demonstrated that the effect of non-hydrostatic stress in the case of He can be neglected up to 150 GPa [35]. The hydrostatic limit for liquids such as methanol-ethanol mixtures or silicone oil is $<$12 GPa [87]. In the case of a solid PTM, such as alkali halides or Al_2O_3, the hydrostatic limit is even lower. In this study we always used solid pressure transmitting media since, despite their poorer hydrostatic properties, they normally provide a good thermal insulation and can confine liquids.

Thermal insulation, chemical inactivity, ease of compaction and transparency

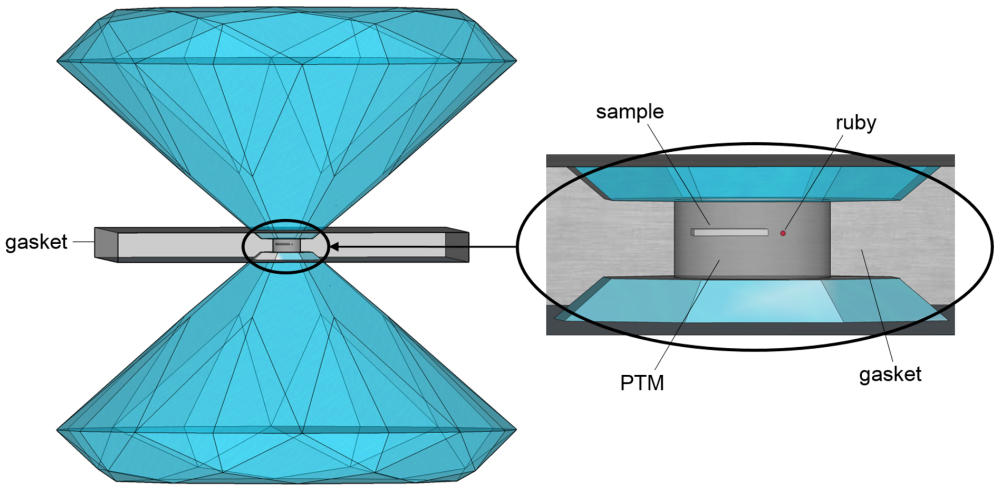

Figure 2.6 – Schematic of the sample chamber.

Characteristics	**KCl**	**amorphous SiO_2**	**KBr**	**Al_2O_3**
Thermal insulation	✓	×	✓	✓
Chemical inactivity	✓	✓	∼	?
Ease of compaction	✓	×	✓	∼
Transparency (amb P)	✓	×(opaque)	✓	×(opaque)
Transparency (P>10 GPa)	✓	✓	✓	✓

Table 2.1 – Summary of tests on different pressure transmitting media performed in the first experiment of this work. The question mark is due to insufficient number of experimental runs performed with Al_2O_3.

were characterised for several selected solid pressure transmitting media; the relevant properties are listed in Table 2.1. As these tests demonstrated the superiority of KCl, this PTM was always used for all subsequent experiments. Drying the KCl in an oven at 120 °C for at least four hours allows to minimize the amount of water that could trigger chemical reactions between the sample and the carbon of the diamonds [38]. As additional caution, the sample loadings were performed in a glove bag in nitrogen atmosphere.

2.4.2 Pressure determination

Several methods have been developed to measure the pressure *in-situ* in the diamond anvil cell. One method is to use X-ray diffraction on a standard (such as KCl, Au, etc) where the pressure is obtained from the lattice parameters calculated from the diffraction pattern. This procedure is particularly convenient if the experimental

technique used to probe the sample is X-ray diffraction. Otherwise it is also possible to use an optical sensor (such as a ruby or the diamond itself) as a pressure gauge. The ruby fluorescence and the Raman signal of the diamond change with pressure and have been already calibrated. Since the nano-polycrystalline diamonds do not show a Raman signal we measured the pressure with this method very rarely.

The ruby is a Cr:Al_2O_3 crystal showing, if excited by a laser or by X-rays, a characteristic luminescence doublet of peaks R1 and R2 at specific wavelengths, see Figure 2.7. In 1972 it was shown for the first time that the doublet shifts with pressure [61], and several empirical laws to determine the pressure as a function of the wavelength of peak R1 have been proposed since. The relationship between pressure in GPa and the wavelength λ of the peak R1 in nanometres can be described, at room temperature, as

$$\mathrm{P} = \frac{1904}{\mathrm{B}}\Big[\Big(\frac{\lambda - \lambda_0}{\lambda_0}\Big)^{\mathrm{B}} - 1\Big] \tag{2.6}$$

where λ_0 is normally 694.24 nm and the parameter B is 5 in non-hydrostatic, 7.665 in quasi-hydrostatic [104] and 9.5 in hydrostatic conditions [36]. In Figure 2.7 several ruby luminescence shifts are represented and the three different ruby scales here introduced. The position of the ruby luminescence line R1 varies with the temperature as well, with a slope of 0.068 Å/K [69].

In this work the pressure was determined with the ruby fluorescence method: one or few tiny ruby crystals with a diameter of $\mathrm{sim}5$ μm were always placed in the diamond anvil cell in the pressure transmitting medium together with the sample, as in Figure 2.6, and their luminescence was excited by a green (532 nm) laser or by X-rays (with an energy between 7 and 8 keV). The ruby scale we used is the non-hydrostatic one.

Pressure and temperature are not completely disentangled. The thermal motion of the atoms in the lattice causes an increment $\mathrm{P_{th}}$ of the total pressure; the total equation of state P(V,T) can be expressed as follows

$$\mathrm{P(V,T)} = \mathrm{P(V,300K)} + \mathrm{P_{th}(V,T)} \tag{2.7}$$

where $\mathrm{P(V,300K)}$ is the equation of state at ambient temperature and $\mathrm{P_{th}}$ is the thermal pressure correction. During X-ray diffraction measurements, knowing the temperature and the thermal equation of state of the standard (such as KCl), it is possible to deduce the thermal pressure acting on the sample. In X-ray absorption measurements this is not possible. The pressure is thus measured before and after heating and the thermal pressure has to be calculated.

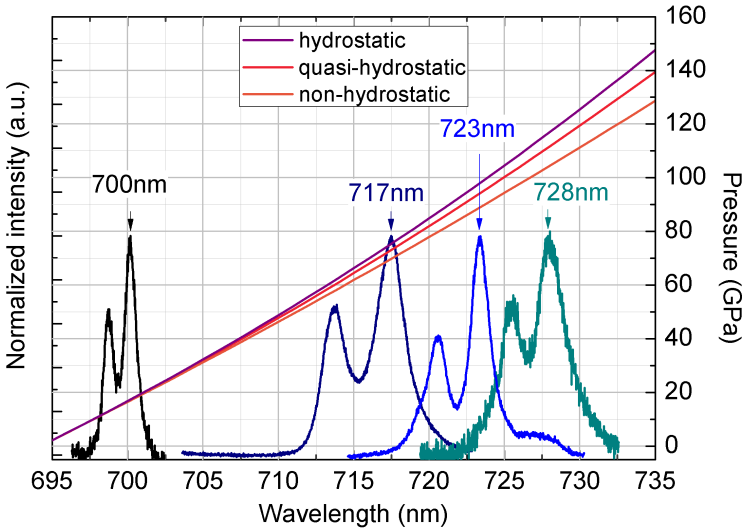

Figure 2.7 – Ruby luminescence signal at different pressures (normalized for the intensity of the peak R1) and the value of pressure as a function of the position of the peak in the hydrostatic [36], quasi-hydrostatic and non-hydrostatic conditions [104].

The procedure adopted in this work to calculate the thermal pressure is the one proposed by Lord et al. [100]. The thermal pressure can be described in its linear dependence with the temperature as

$$\mathrm{P_{th}} = \alpha \mathrm{K_T}(\mathrm{T} - \mathrm{T_0}), \tag{2.8}$$

where $\mathrm{T_0} = 300$ K while $\alpha \mathrm{K_T}$ is not known *a priori* and according to Lord it has to be described as a function of pressure. The thermal pressure at the melting temperature, $\mathrm{P_m}$, can thus be expressed as $\mathrm{P_m} = \alpha \mathrm{K_T}(\mathrm{T_m} - \mathrm{T_0})$, where $\mathrm{T_m}$ is the melting temperature. Its trend as a function of pressure was empirically evaluated for KCl by Lord et al. using X-ray diffraction. If $\mathrm{P_{300}}$ is the pressure measured on the ruby at room temperature after heating, the thermal pressure at the melting temperature can be calculated as $\mathrm{P_m} = 0.03 \cdot \mathrm{P_{300}}$. From these two equations it is then possible to evaluate $\alpha \mathrm{K_T}$. In the case of KCl Equation 2.8 can be written as

$$\mathrm{P_{th}} = \frac{0.03 \cdot \mathrm{P_{300}}}{\mathrm{T_m} - \mathrm{T_0}}(\mathrm{T} - \mathrm{T_0}). \tag{2.9}$$

The error in the evaluation of the pressure is principally due to intrinsic gradients in the cell and by the pressure variations that occur while heating. Gradients in the

cell can be evaluated measuring several rubies placed in different positions of the sample chamber; the difference of pressure between them can be of few GPa at 100 GPa. The difference in the pressure measured on the ruby before and after heating the sample instead is $\sim$5 GPa at about 50 GPa and can be up to 10 GPa at 100 GPa. In this work we considered that the main contribution to the error is given by the sample pressure variation that occurs during heating that is evaluated as 10% of the pressure value.

2.5 High temperature

A sample in a diamond anvil cell can be heated resistively or using lasers. In the first method the entire sample chamber is heated by the Joule effect and the temperature is measured with a thermocouple. The maximum temperature that can be reached with this method is 1600 K, before the diamonds oxidise and the gasket starts to flow. In order to go beyond 1600 K it is necessary to localize the heating on one spot of the sample. This is achieved with the laser heating method, where temperatures up to 6000 K can be reached [149, 148, 150] and measured through the black body radiation emitted by the heated spot. The system dedicated to X-ray absorption spectroscopy that is used on ID24 to laser heat and measure the temperature is described here below.

2.5.1 Laser heating setup

The principal characteristics of a laser heating setup are the delivery of a laser beam on the sample and an optical system that allows sample imaging and temperature measurements *via* spectral-radiometry. The laser heating system used for this work is then coupled with the detection of X-ray absorption spectroscopy that allows *in-situ* measurements [153, 81]. The angular aperture of the DAC is thus crucial to allow the simultaneous heating with the laser and temperature and X-ray absorption measurement.

Two 120 W Nd:YAG fiber-coupled lasers in their fundamental TEM_{00} mode with a wavelength of 1064 nm (2 in Figure 2.8) are delivered to the two opposite sides of the diamond anvil cell (1 in Figure 2.8) with dedicated optics that consists in several mirrors with a proper antireflection coating cutting some of the laser tails and a 0.5 inch diameter lens with a 50 mm focal distance (3 in Figure 2.8). Heating from both sides minimises axial temperature gradients on the sample. The two lasers, whose beam profile is Gaussian, hit the diamond anvil cell with an angle of 30 degrees with respect to the direction normal to the sample. This configuration avoids back-reflections

that could heat the lenses, thereby changing the focal distance. The laser beams are slightly defocused in order to have a uniform temperature on the sample surface up to 20 μm in diameter, at least 2-3 times larger than the X-ray spot.

Sample imaging and temperature measurement are coupled in this system. The image of the cell and the thermal emission of the heated spot share the same path for most of its length (from 1 to 5 or from 1 to 7 in Figure 2.8). The image of the sample chamber, whose typical size is in the order of hundreds of microns, is magnified by means of a couple of achromatic lenses mounted at the two extremities of a custom-build objective (4 in Figure 2.8). The lens closer to the DAC has 30 mm focal distance, while the other one has a 500 mm focal distance. In front of the first lens is placed a removable aperture, or pupil. During the optical alignment of the DAC it is completely open and the numerical aperture of the microscopes is 0.2; during the temperature measurements the pupil is closed lowering the numerical aperture to 0.065 and thus reducing the effect of chromatic aberrations [66]. The magnified image is projected on a metallic mirror positioned at the entrance slit of a Czerny-Turner type optical spectrometer (5 in Figure 2.8). The mirror has two ∼35 μm holes separated vertically by ∼4 mm that are used to collect the light from the two sides of the DAC. As a convention, the optical path from the DAC to the higher hole is called upstream (US) and the other one is the downstream (DS). The mirror is tilted by ∼5 degree thus projecting the image on a high sensitivity colour digital video camera (8 in Figure 2.8) used for X-rays and lasers alignment on the sample. The two holes in the mirror, that correspond to few microns in diameter in the DAC image on the camera, collect the light of the hot spot from two sides of the DAC simultaneously into the spectrometer. In the spectrometer the light from the two sides is dispersed and focused on a 1340x400 pixels Pixis back-illuminated CCD camera (6 in Figure 2.8) at two different heights, where they are recorded. In the spectrometer there are three separate diffraction gratings that allow temperature measurements (where a wide wavelength range is necessary: 570 - 980 nm) and pressure determination measured by ruby fluorescence or Raman signal of the diamond (where a high spectral resolution is required).

A 532 nm green laser (12 in Figure 2.8) is used to excite the ruby luminescence and the Raman signal of the diamonds and joins the optical path of one of the two infrared lasers.

2.5.2 Temperature determination

The typical way to measure the temperature from a small hot spot (∼ 20 μm in diameter) is *via* spectral radiometry. The spectrometer has to be calibrated in

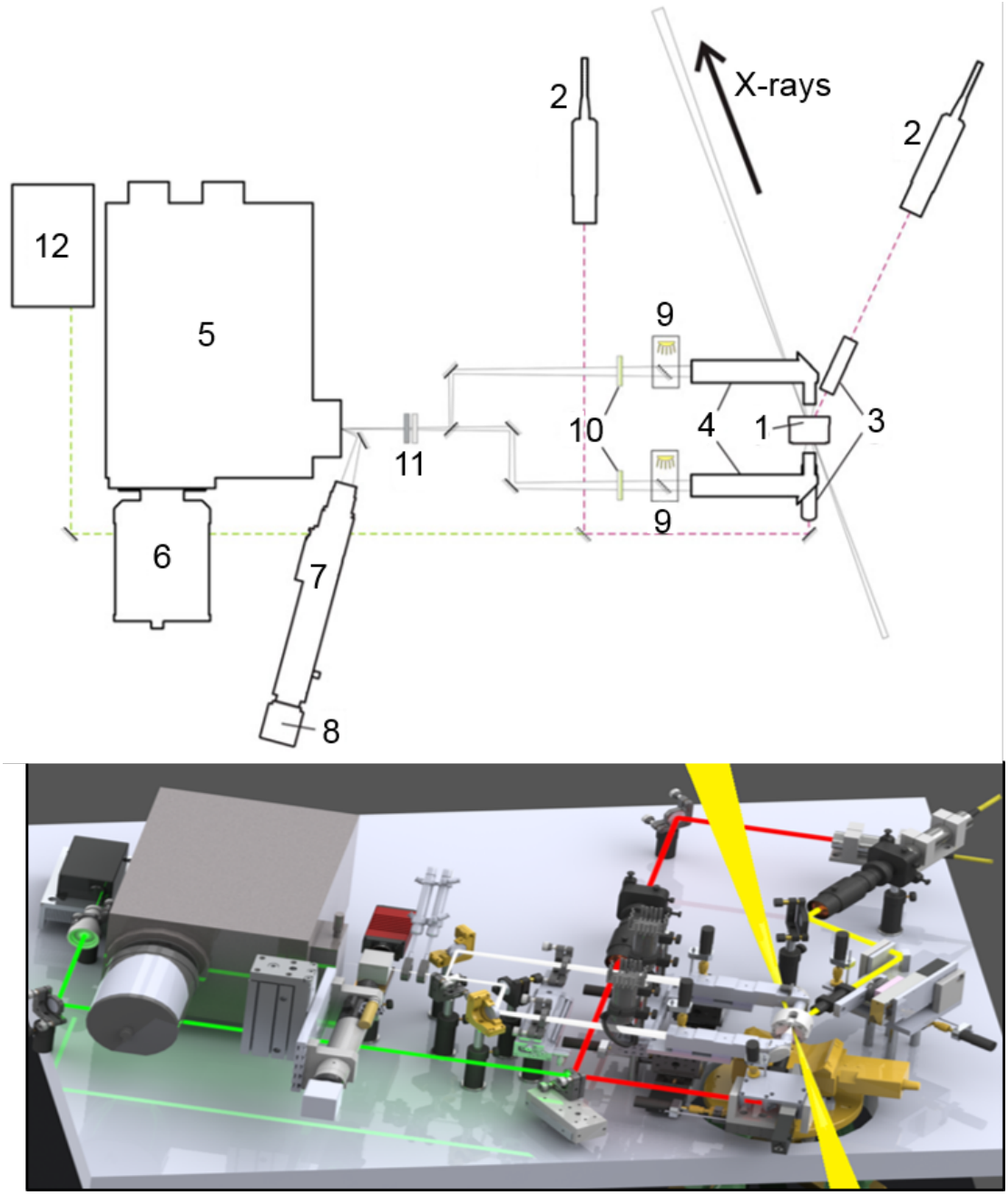

Figure 2.8 – Scheme of the laser heating system of ID24 at ESRF [153]. (1) water-cooled copper holder where the diamond anvil cell is positioned, (2) fiber coupled IR lasers whose optical path is indicated by a dashed red line, (3) laser focusing lenses, (4) objectives for the images and the temperature measurement, (5) spectrometer, (6) Pixis CCD back illuminated camera, (7) motorized zoom, (8) colour digital video camera, (9) beam splitters and LED illumination modules, (10) removable notch filters, (11) neutral density filters, (12) green laser for ruby luminescence and Raman excitation, its direction is indicated by a dashed green line. The direction of X-rays is indicated by a black arrow.

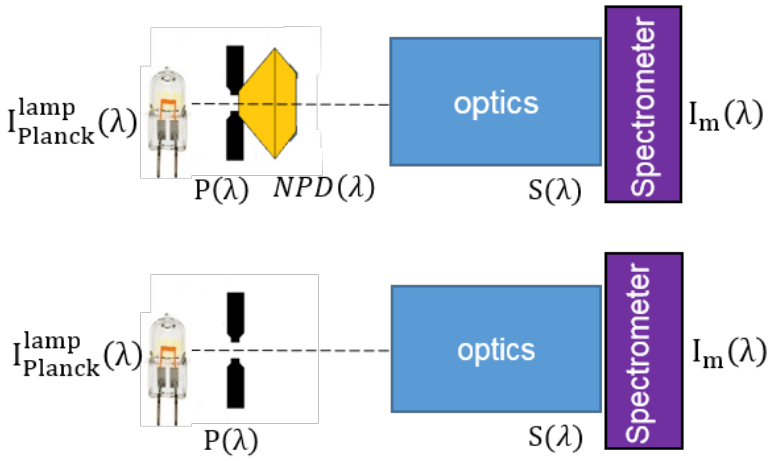

Figure 2.9 – Nano-polycrystalline diamond calibration.

wavelength and intensity. To calibrate the wavelength a neon lamp, whose spectrum shows very sharp peaks in the range 580-750 nm, is used. To calibrate the intensity a tungsten lamp, whose temperature as a function of the current applied is known, is used. The lamp is placed in the position of the DAC (1 in Figure 2.8) and a potential difference is applied until the current flowing in the lamp, measured with an amperemeter, is 3 or 4 Ampere, corresponding to a temperature of 2436 or 2913 K respectively.

Calibration

The intensity $I_m(\lambda)$ measured on the spectrometer as a function of the wavelength is given by the intensity emitted by the source $I_e(\lambda)$ (the calibration lamp or the hot spot) multiplied by the response of the system $S(\lambda)$ that includes the efficiency of each optical element: filters, mirrors and grating and camera of the spectrometer. We can thus write:

$$I_m(\lambda) = I_e(\lambda) * S(\lambda).$$

During the calibration $I_e(\lambda)$ is known, since the temperature of the lamp is known, $I_m(\lambda)$ is measured and $S(\lambda)$ is calculated for the two paths upstream and downstream separately. During a real measurement the $I_e(\lambda)$ can be calculated assuming that $S(\lambda)$ is constant with the temperature. Because of its yellowish colour, when a nano-polycrystalline diamond is used, its contribution has to be taken into account as well.

The procedure used to calculate the contribution of the nano-polycrystalline diamonds follows. A NPD diamond was glued on a pinhole with a 100 μm diame-

ter, as shown in Figure 2.9, and $I_m^{NPD}(\lambda) = I_e(\lambda) * S(\lambda) * P(\lambda) * NPD(\lambda)$ was measured, where $P(\lambda)$ is the contribution of the pinhole and $NPD(\lambda)$ the one of the nano-polycrystalline diamond. Then the same measurement was performed removing the diamond and leaving the pinhole thus obtaining $I_m^P(\lambda) = I_e(\lambda) * S(\lambda) * P(\lambda)$. Since the current flowing in the lamp was unchanged, the temperature and thus $I_e(\lambda)$ remained unchanged as well. The calibration of the NPD is then calculated as $NPD(\lambda) = I_m^{NPD}(\lambda)/I_m^P(\lambda)$. During the experiment the $I_e(\lambda)$ emitted by the hot spot is calculated as $I_m(\lambda)/S(\lambda)$ when single crystal diamonds are used and as $I_m(\lambda)/(S(\lambda) \cdot NPD(\lambda))$ in the case of nano-polycrystalline diamonds, under the assumption that $NPD(\lambda)$ does not change with pressure and temperature.

Planck's law

The $I_e(\lambda)$ is then fitted with Planck's law describing the spectral density of electromagnetic radiation emitted by a grey body at a given temperature T

$$P(\lambda, T) = \epsilon \frac{2\pi hc^2}{\lambda^5} \frac{1}{e^{\frac{hc}{\lambda k_B T}} - 1} \tag{2.10}$$

Where h is the Planck's constant, c the speed of light, λ the wavelength (in the 570 - 980 nm range). The two fit parameters are the emissivity ϵ, considered constant as a function of the wavelength in the grey body approximation, and the temperature T.

Spectroradiometrical temperature determination is critical since large errors appear from wavelength dependent emissivity and both radial and axial thermal gradients. In fact the emissivity as a function of pressure is not known *a priori*, moreover slight misalignments of the pinhole of the spectrometer on the hot spot can lead to a misestimation of the temperature. Therefore another method, reported in the literature as "sliding two-color" technique, has been used in this work to investigate wavelength dependent irregularities that can be due to emissivity variations, optical misalignment, chromatic aberrations etc. [66, 84]

Sliding two-color technique

Before presenting the two-color method we first need to introduce the Wien formula [163, 66]. Assuming that $e^{\frac{hc}{\lambda K_B T}} >> 1$ approximates Equation 2.10 in

$$P_W(\lambda, T) = \epsilon \frac{2\pi hc^2}{\lambda^5} e^{-\frac{hc}{\lambda k_B T}} \tag{2.11}$$

If then we define the Wien function as

$$\mathrm{Wien}(\lambda, \mathrm{T}) = \frac{\mathrm{K_B}}{\mathrm{hc}} \ln\Big(\mathrm{P_W}(\lambda, \mathrm{T}) \frac{\lambda^5}{2\mathrm{hc}^2}\Big)$$

we obtain

$$\mathrm{Wien}(\lambda, \mathrm{T}) = \frac{\mathrm{K_B}}{\mathrm{hc}} \ln\epsilon - \frac{1}{\lambda \mathrm{T}}$$

were the linear dependence with 1/T is clear.

The temperature can thus be expressed as

$$\mathrm{T_{two-color}}(\lambda) = \frac{\frac{1}{\lambda} - \frac{1}{\lambda+\delta}}{\mathrm{Wien}(\lambda) - \mathrm{Wien}(\lambda+\delta)} \tag{2.12}$$

where δ, that defines the width of the window, has to be properly chosen. The two-color is then obtained shifting this window over the entire range in λ. A temperature which is not constant over the spectral range shows that there are problems in the measurements. The choice of δ, as discussed in Benedetti et al. [16], is critical. The best δ is the smallest window width to which corresponds the lowest standard deviation. A too small window would be affected too much by the noise of the thermal radiation spectrum, while if the window is too big the sensitivity to wavelength variation is lost. For our temperature measurements we evaluated the best window to be 50 nm.

In this work we used the two-color fit not only to check that there were no wavelength dependent behaviours in the measurement, but also, as suggested by Benedetti et al. [16], to determine the error in the measurement. An example of Planck's fit and two-color fit is shown in Figure 2.10, where it is possible to notice that the error increases with the increase of the temperature and that it is of the order of hundreds of K.

To summarise, in this work the temperatures are obtained as a result of Planck fits, adopting grey body approximation. The temperature is accepted when the two-color plot is almost flat in a wavelength window $\geq$ 250 nm. The temperature of the sample is obtained averaging the temperature measured in the upstream and in the downstream side. Its error is chosen as the higher value between the difference between the two sides and the error calculated propagating the standard deviation of the two-color fit from the two sides through the average. Typically, the difference between upstream and downstream is smaller than the uncertainty propagated through the average.

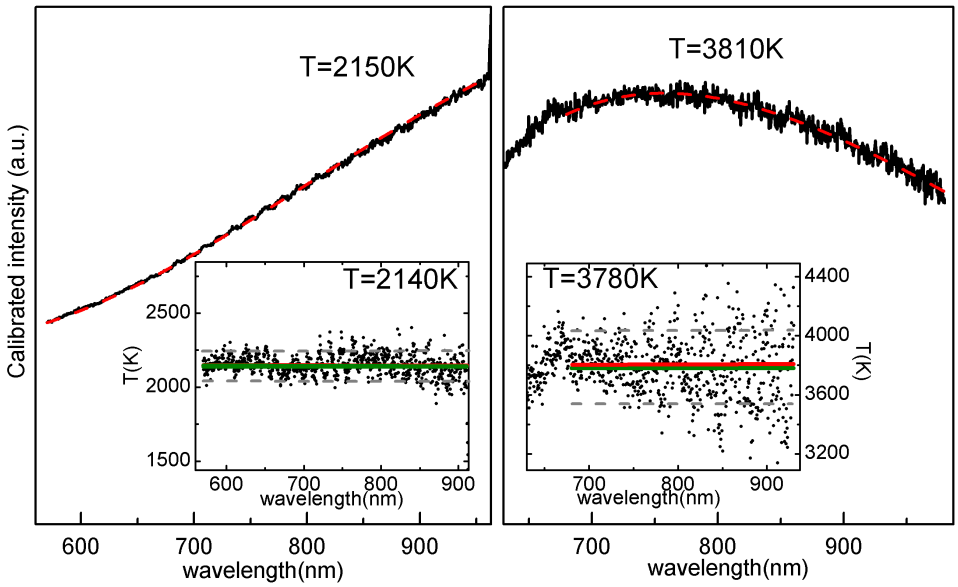

Figure 2.10 – Example of calibrated thermal emitted intensity fitted with the Planck's law, in red, at 2150 K and 3810 K. In the inset the two-color fits are shown with the mean temperature in green, in comparison with the result of the Planck fit in red. The dashed grey lines indicate the standard deviation around the mean value.

2.6 Measurement strategy

Up to now the measurement of the X-ray spectrum, of the pressure and of the temperature were considered separately. During the experiments, though, the three of them are entangled and synchronised as illustrated in the following.

The first step is to collocate the diamond anvil cell in its designated position in the laser heating setup. When it is aligned in the optical path, meaning that its image is visible with the colour digital video camera, the pressure can be increased and it is measured exciting the ruby luminescence with the green laser. When the required pressure is reached, the alignment of the spectral-radiometric optics and the X-rays is checked: the fluorescence of the X-rays on the pressure transmitting medium has to be aligned on the position of the spectrometer pinhole both upstream and downstream [111]. This alignment, crucial to ensure the collection of XAS and temperature data from the same spot on the sample, is double-checked by verifying the X-rays position on gasket borders using knife-edge scans. Then different regions of the sample are checked with the X-rays to find the best XAS signal; during the cell preparation it is in fact possible to slightly ruin the sample that can become thinner in some regions thus giving an inhomogeneous XAS background. The lasers are then aligned on both sides of the chosen region and defocused in order to obtain a wide uniform

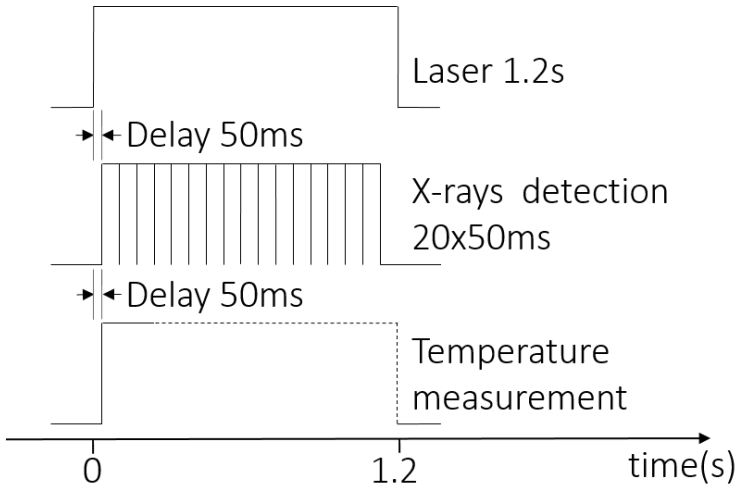

Figure 2.11 – Synchronization scheme. The lasers pulse lasts 1.2 s. During this time 10-20 spectra of 100-50 ms each are collected on the FReLoN X-ray camera starting with a delay of 50 ms after the onset of the laser pulse. The temperature is measured with an integration time that depends on the emitted intensity (it ranges from 1 s to 0.01 s).

hotspot around the selected spot. Each heating run starts with a spectrum at room temperature and is followed by a sequence of alternating hot and quenched (to room temperature) spectra. The quenches allow tracking possible changes in the sample due to chemical reactions or distortions of the sample. The laser power for each of the two lasers can be chosen independently as a fraction of the total laser power. The laser pulse, the XAS acquisition and temperature measurement are synchronized by a trigger according to the scheme in Figure 2.11.

At first the laser is switched on. After 50 ms, delay chose to discard possible instabilities due to sudden temperature variation, the temperature and the X-ray measurement start. The acquisition time for the X-ray detector is chosen to optimize the signal to noise ratio for XAS. Typically an acceptable signal quality for nickel in the DAC is obtained averaging 10-20 acquisitions of 50-100 ms each, therefore the laser pulse is of the order of the second, an interval sufficiently short to minimize chemical reactions. The temperature is measured independently from both sides of the cell, with an integration time varying according to the black body emission intensity: typically 1 s at 1500 K and down to 0.01 s around 3000 K.

An on-line analysis is carried out in order to track changes in the absorption spectrum of the hot sample; the laser power is then increased to reach the melting temperature. Every time a new run of measurement starts, a new position on the sample is chosen, in order to avoid the probing of a region where the sample reacted or per-

colated through the pressure medium.

2.7 Melting at ambient pressure

With the purpose of recording a liquid absorption spectrum at ambient pressure to be compared with the ones at more extreme conditions, a device different than the diamond anvil cell can be placed in the laser heating setup. While in a DAC most of the photons are absorbed by the diamonds, if the sample is in air the number of photons reaching the detector is much more and it thus allows very fast measurements [82].

The foil is placed on a sample holder and is installed in the focal position of the two lasers and the X-rays. The sample holder is then enclosed in a plastic chamber, insert in Figure 2.12, provided with small holes to let the lasers heat the sample and the X-rays pass through the sample and reach the detector. In the chamber an inert gas such as nitrogen is fluxed at 1.5 ℓ/min in order to avoid contamination with the oxygen present in air.

The synchronization is set as follows. X-ray spectra are measured continuously with 250 μs integration time, the two lasers are switched on after 5 ms and they last 0.5 s. The procedure is repeated increasing every time the laser power by $\sim$0.1 W until the sample melts. At this speed it is not possible to measure the melting temperature with the spectrometer, whose fastest acquisition time is 10 ms, but the transition to the fcc phase and the melting are detected. An example is shown in Figure 2.12. The temperature of these phase transitions is normally well known at ambient conditions. In the case of cobalt, represented in Figure, we thus expect the first fcc spectra to be at around 800 K and the first liquids at around 1800 K (the melting temperature is 1775 K).

2.8 Ex-situ techniques

After performing the *in-situ* measurement with X-rays while heating the sample, an *ex-situ* post analysis on recovered samples can be performed. This allows to have a more complete vision of the sample behaviour when it is laser-heated.

The post analysis performed during this work consisted in cutting the gaskets along the axis of compression with a focused ion beam (FIB) milling, visualising the exposed cross section with scanning electron microscopy (SEM) to detect textural and shape changes upon heating. In one case we complemented the study with elemental analysis from energy dispersive spectrometry (EDS). The machine used is a

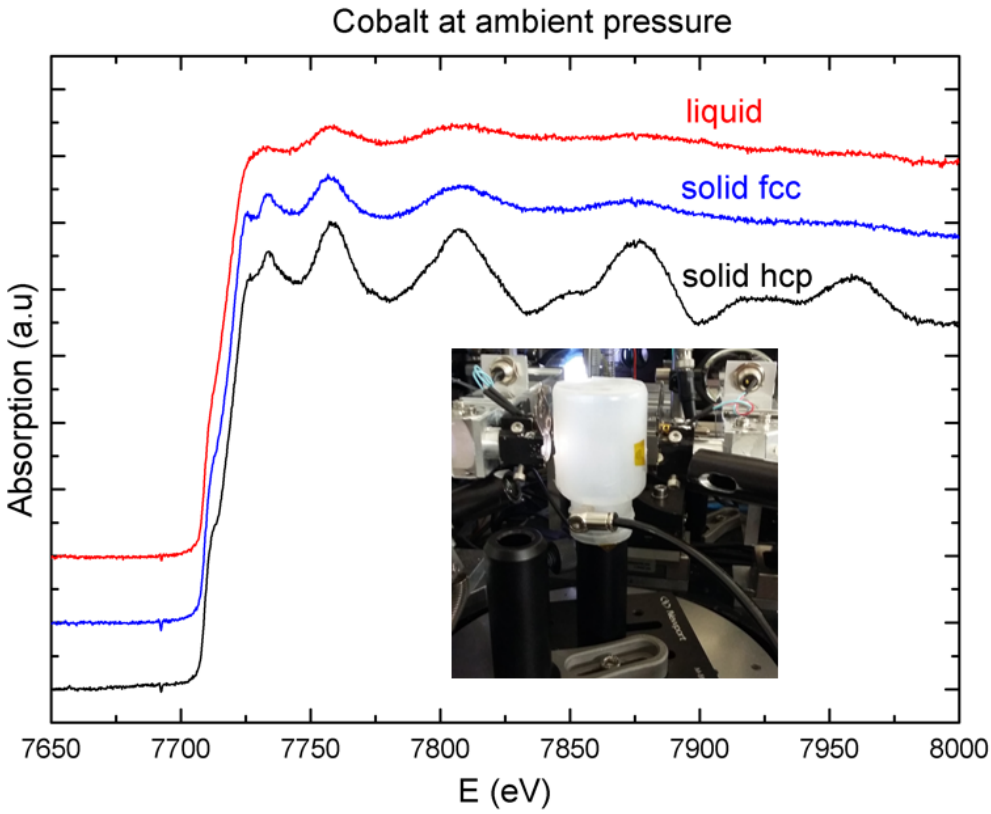

Figure 2.12 – Sequence of spectra showing solid hcp at ambient pressure, a hot solid in the fcc phase and a liquid spectrum. The integration time on the X-ray detector is 250 μs, it was not possible to measure the temperature but at this pressure the phase transitions are well known. In the insert is shown the chamber enclosing the sample.

Zeiss Neon40ESB, installed at the IMPMC (Institut de minéralogie, de physique des matériaux et de cosmochimie) in Paris.

A portion of the gasket containing the sample chamber is cut with laser drilling and separated from the remaining part of the gasket. A first rough cut of the sample close to the heated spot under analysis is then obtained with a triple ion-beam milling system (LEICA EM TIC 3X). The remaining part of the sample is then coated with a platinum strip (using the machine LEICA EM SCD500) whose function is to protect the sample, in the following steps, from beam damage and beam contamination.

Several samples are then positioned in the FIB and SEM instrument, whose scheme is represented in Figure 2.13. Here the milling is produced by a gallium beam operating at 30 kV and 2 nA - 500 pA for final surfacing. Gallium ions are in fact heavy enough to rip the sample's atoms off.

The visualization is performed by means of the SEM column, where the primary electron beam is generated in the field emission gun (FE-gun) and is focused on the sample. The surface of the sample irradiated by the primary electron beam emits electrons at different energies. The visualization of the sample is possible due to the detection of the secondary electrons (SE), i.e. those electrons that have undergone multiple scattering events and that originate from a depth of 5-50 nm. Their spectral distribution and intensity is not specific to a particular material, which explains the poor contrast between different materials. The contrast in the resulting image is instead given by differences in surface roughness and work function [101].

An accessory port is provided for energy dispersive X-ray spectroscopy (EDS), which is an analytical technique used for the elemental analysis of the sample. A high energy beam of electrons (5-25 keV) is focused on the sample and it creates core holes in the atoms. When the core hole is filled, X-rays, whose energy depend on the element, are emitted. The intensity of the emitted X-rays is measured by an energy dispersive spectrometer and the resulting spectrum contains a clear signature of the elements in the sample, thus allowing the measurement of the elemental composition.

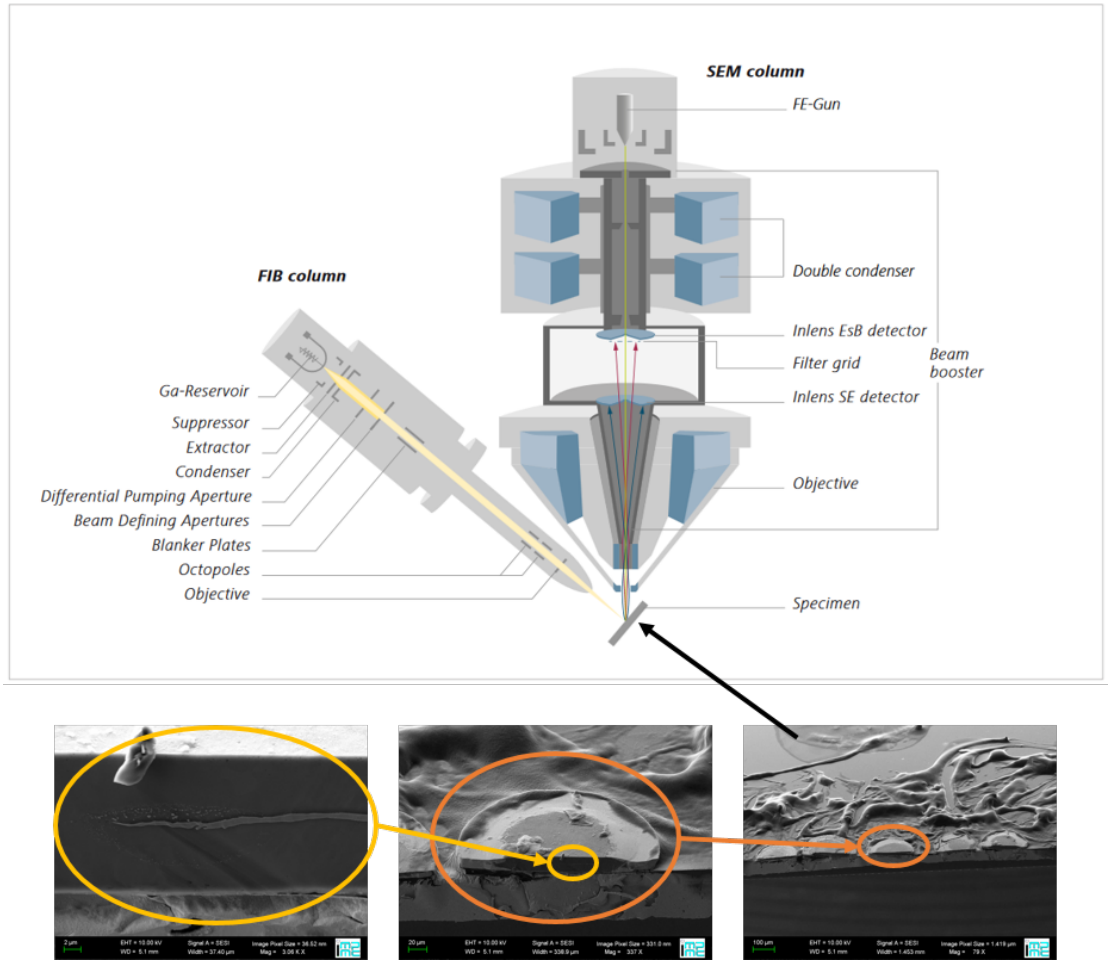

Figure 2.13 – Schematic of the Zeiss machine for milling and visualization. FIB and SEM column are arranged at an inclination angle of 54°. At the bottom, from the right to the left, a glass with several samples already roughly cut with the triple ion beam milling, zoom on one sample, zoom on the image of the exposed cross section of the sample where the foil embedded in the pressure transmitting medium is visible.

Chapter 3

Melting curves of nickel and cobalt with XAS

In this chapter, the methods used so far in the literature to detect melting of nickel and cobalt under pressure are resumed. The resulting curves are then presented and compared. The melting criterion proposed for XAS is described and validated. The melting curves for nickel and cobalt obtained using this criterion are shown and compared with the literature. Finally critical aspects in the LH-DAC experiments are discussed, paying particular attention to those prevailing in XAS techniques.

3.1 State of the art

Ever since it became possible to combine high pressure and high temperature techniques, there has been a growing interest in the scientific community towards determining the melting curves of several materials, especially those with strong geophysical or technological implications. There are many examples of structural investigations focused on the detection of the first order phase transition from solid to liquid (melting) and XAS has played an important role [41, 11]. In this section, we will focus especially on the detection of melting at high pressures, i.e. the determination of melting curves, achievable with the DAC.

The experimental methods that have been used so far in the literature for detecting the melting curves of nickel and cobalt in laser-heated diamond anvil cell experiments are: the direct observation of movements on the sample surface, X-ray diffraction (XRD) measurements and detection of slope changes in the temperature versus laser power relation. In addition to using experimental methods, it is possible to calculate the melting curves from molecular dynamics.

Visual observation (speckle)

In the visual observation of movements on the sample surface, the interference pattern of a green laser beam is observed upon laser heating. A rapid and continuous movement of the interference pattern, or speckle, can be associated to the melting of the sample. This method has been used for both nickel [92, 51, 78, 50] and cobalt [93, 51].

With this method, only the surface of the sample is examined. Critics to the speckle melting criterion state that it is impossible to distinguish the transition to the liquid state from a surface chemical reaction or from a solid-solid transition.

X-ray diffraction

The loss of constructive interference between the X-rays scattered from the atoms, i.e. the loss of sharp peaks in the diffraction pattern, is due to the loss of long range order, characteristic of the solid-liquid transition. The liquid diffuse scattering is then a probe of the short range order.

This method has been applied on nickel [100], but to our knowledge a diffraction study of the melting curve of cobalt is still missing.

The melting curves measured with XRD are very often steeper than those obtained with the visual observation of speckle for different metals such as iron, lead and tantalum, as well as nickel [37, 38, 9, 100]. For this reason, the pertinence of the visual observation has been questioned and the speckle motion was suggested to be a signature of fast recrystallisation of the solid samples rather than melting.

Temperature versus laser power

This method detects sudden changes in temperature evolution with heat input. It consists of observing the slope of the variation in temperature as a function of the provided laser power. This method does not probe directly the phase of the sample, but the presence of a plateau in the temperature with increasing laser power has been proposed as a signature of melting, since it could mean that the energy provided goes towards the latent heat of fusion instead of increasing the temperature.

This criterion, which also probes only the surface of the sample, was used for the determination of the melting curve of nickel to complement XRD measurements [100]. Here it was applied in the case of continuous exposure to the laser, with gradually increasing laser power. In this work, as explained in Section 2.6, the sample was

always heated through laser pulses about 1 s long. Thus in our case the temperature is rarely a smooth monotonic function of the laser power and this criterion is not applicable.

However the reason for the existence of such plateau in LH-DAC studies is still debated. The plateau has been proposed to be caused by a change in the sample's reflectivity, that would affect the laser absorption rather than be a signature of melting [65].

Molecular dynamics calculations

In the literature, experimental melting curves are often compared with simulated ones, generally based on molecular dynamics. Simulations differ by the potential used to describe the system and how the interactions between atoms are computed, that can be based on classical or quantum physics. We will refer to the first ones as MD and the second ones as QMD or based on density functional theory (DFT). With a procedure similar to the one described in Section 4.2.1, an atomic supercell is generated at the desired pressure and temperature conditions. Typically, the system is heated and then is left evolving.

There are several ways to describe the melting: the one-phase or hysteresis method, the two-phase or solid-liquid coexistence method, the free energy method and the Z method [173]. From these, we will discuss the first two, that are the most common ones [112] and that were used for both nickel and cobalt. In the one-phase method, the melting temperature is estimated from the average between the temperatures of the overheating and overcooling states. Here, overheating and overcooling are defined as states at which there is a jump in the volume versus temperature curve, while heating or cooling respectively. Instead, in the two-phase method only half of the cell is heated while the other half is kept frozen. When the system is left evolving, there is a subsequent freezing or melting of the supercell that releases or absorbs latent heat. As a consequence, the temperature that has been initially assigned to the system will increase or decrease and it will reach equilibrium at the melting temperature $\mathrm{T_m}$ [15].

3.1.1 Nickel

The experimental and theoretical melting curves of nickel that can be found in the literature are shown in Figure 3.1. The methods used are all those mentioned above. A large discrepancy of about 700 K at 70 GPa is observed for the experimental melting curves (represented in Figure 3.1 as dashed lines + markers) derived from visual

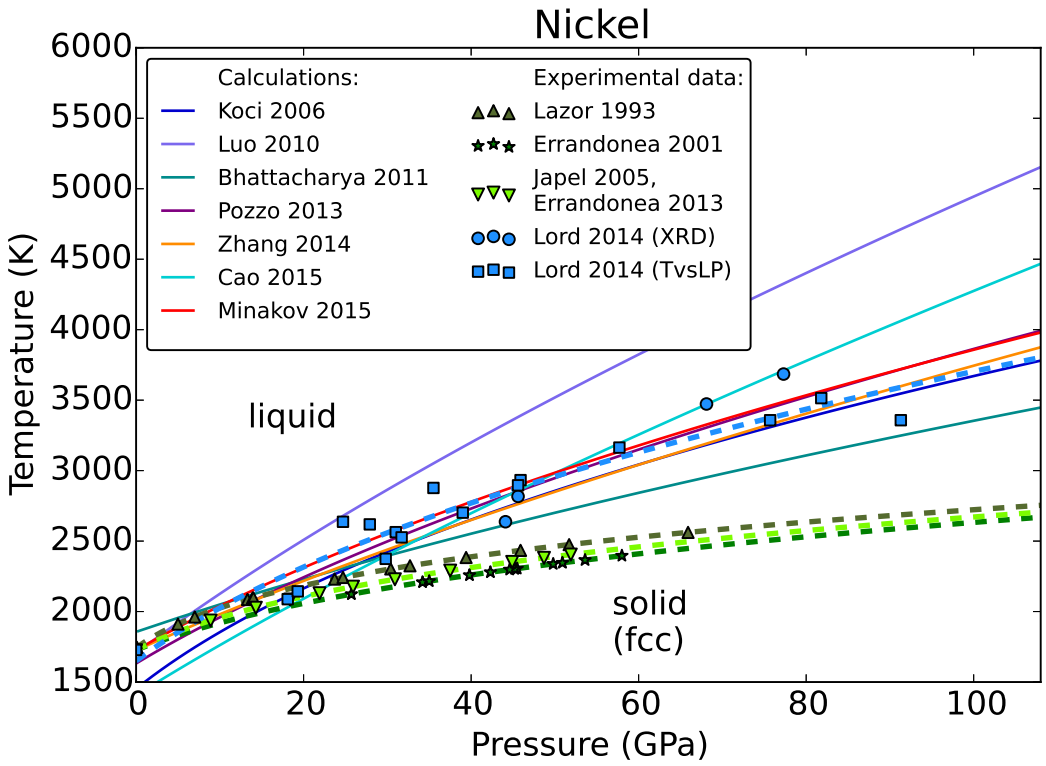

Figure 3.1 – Nickel phase diagram. Comparison between experimental data measured with different techniques (dashed lines+markers) and different theoretical calculations (continuous lines). Experimental melting curves based on speckle melting criteria such as Lazor 1993 [92], Errandonea 2001 [51], Japel 2005 [78] and Errandonea 2013 [50] are at significantly lower temperatures than the XRD experimental curve measured by Lord 2014 [100] - which is divided into melting points determined with XRD, blue circles, and with the temperature versus laser power plateau (TvsLP) points indicated with blue squares - and all the ab-initio calculations [88, 102, 19, 127, 173, 32, 112].

observation of the speckle and X-ray diffraction complemented by the temperature plateau method.

Theoretical calculations have been performed on nickel using classical molecular dynamics (MD) [88, 102, 19, 173, 32] and density functional theory (DFT) [127, 112]. Generally, a good agreement is found between theoretical and experimental curves detected with XRD and the temperature plateau method. The calculations giving the best agreement with the experimental curve of Lord [100] over the widest pressure range are obtained from molecular dynamics using the embedded atom method with Mendelev's potential (and with both the one-phase and the two-phase approach) [173], or in the case of first-principle calculations based on density functional theory [127, 112]. None of the calculated curves, though, are able to reproduce the melting detected by visual observation.

3.1.2 Cobalt

The experimental and theoretical melting curves for cobalt are shown in Figure 3.2. The studies reported in the literature are limited to two experiments, both using visual observation as melting criterion, and one theoretical calculation where the Zhou's embedded atom method potential was used with both one-phase and two-phase approach, using Zhou's and Pun's potentials.

The agreement between the existing curves is quite poor. At 60 GPa there is a difference of 400 K between the two experimental curves and between Lazor's curve [93] and the calculations using Zhou's potential [174]. Between the two theoretical curves the discrepancy is even larger.

A measurement with X-ray diffraction is still missing in the literature, as well as a temperature versus laser power study. The purpose of this work is to provide a new experimental melting curve of cobalt, based on X-ray absorption spectroscopy.

3.2 Choice and validation of the melting criterion

Another experimental method used to detect melting consists in the observation of changes - typically discontinuities - in the XANES region of an absorption spectrum at increasing temperature. A precise measurement of the absorption coefficient at a single energy as a function of temperature can be used to detect a phase transition. This is the basis of the "single energy X-ray absorption temperature scan" method (T-scan method), that was used in the past years to detect not only solid-liquid but also solid-solid phase transitions of several metals upon changes of temperature or pressure. First experiments were performed at ambient pressure and in-

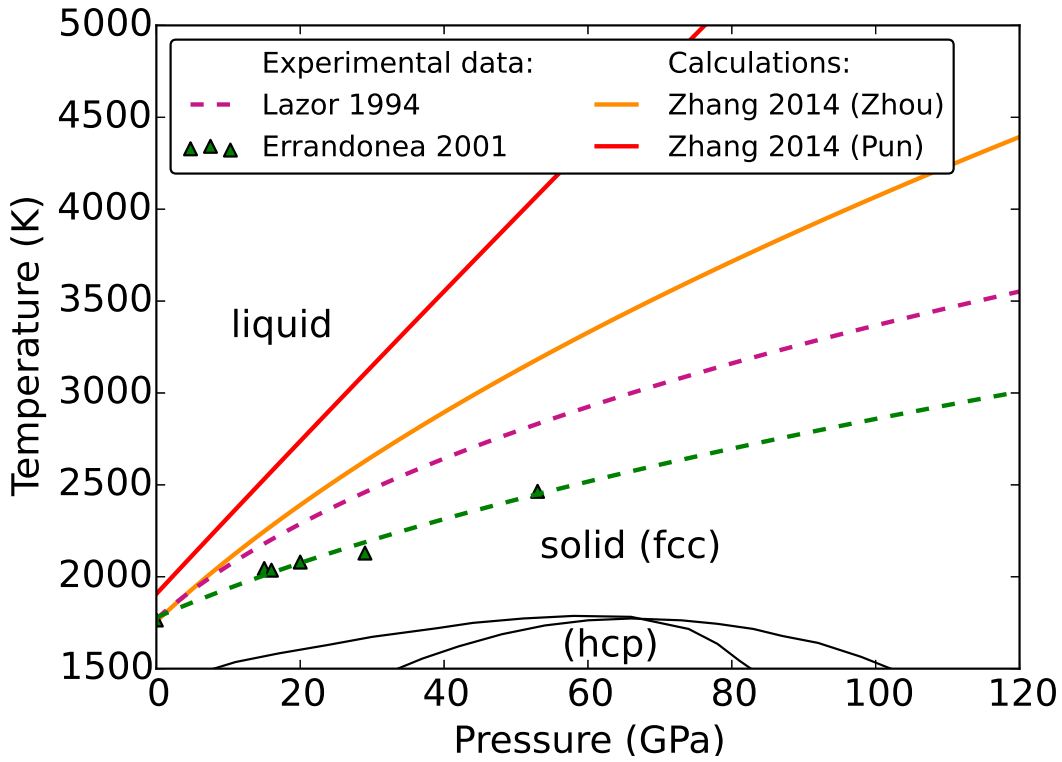

Figure 3.2 – Cobalt phase diagram. Comparison between experimental data, represented with dashed lines + markers (when available) and theoretical calculations, represented with continuous lines. In the region of the solid, the hcp-fcc transition represented by black continuous curves is the one measured by Yoo [168]. Experimental curves, Lazor 1994 [93] and Errandonea 2001 [51], are based on the visual observation of speckle. The two theoretical curves were obtained by Zhang [174] using molecular dynamics calculations averaging the one-phase and two-phases approach for two different potentials (Zhou's and Pun's potential).

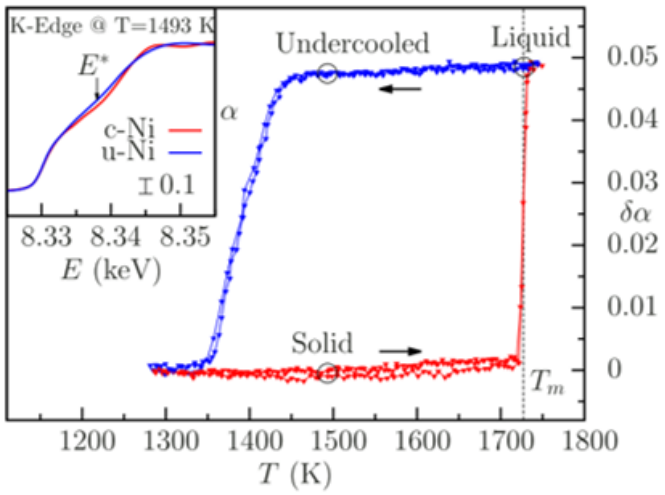

Figure 3.3 – Example of T-scan method applied to nickel at ambient pressure from the literature: Figure 1 in [41]. The variation of the absorption coefficient at 8.338 keV, indicated with $\delta\alpha$, is plotted as a function of temperature upon heating (in red), and cooling (in blue). The spectra of a solid (red) and undercooled liquid (blue) are shown in the inset.

creasing temperature on iron and germanium. The already known bcc to fcc transition of iron was detected while melting temperature of germanium was investigated [52]. The T-scan method was also used combined with X-ray diffraction to detect the melting at ambient pressure of germanium [42], lead [57], copper iodide [158], tin [44], copper [43] and nickel [41] as well as at moderate pressures and temperatures for germanium (up to 0.67 GPa and 440 K) [126] and bismuth (up to 6 GPa and 800 K) [128].

An example of T-scan method applied on the melting of nickel at ambient pressure is shown in Figure 3.3. In the inset the XAS spectra are shown, where in red it is represented a solid at 1500 K and in blue the undercooled liquid at the same temperature.

The discontinuities detected with the T-scan method at a specific energy, can be also visualized in the full XANES and in its derivative. In the case of iron at more extreme conditions, melting was in fact identified with the flattening of the edge shoulder and disappearance of the first two oscillations [23].

3.2.1 The iron controversy

XAS was used to determine the melting curve at extreme conditions for the first time in 2015 for iron, up to 100 GPa and 3800 K [11]. The result obtained is in agreement with the melting curve of iron measured using visual observation of speckle.

Since melting detection by visual observation had been questioned only a few years before (2007 for lead [37] and 2013 for iron [9]), this result became the subject of a great controversy. The ability of the XAS melting criterion to detect melting was thus questioned: the observed changes in the XANES could be due to a solid-solid transition or be a signature of fast recrystallization. Moreover, even if this method were indeed able to detect the solid-liquid transition, the discrepancy in the temperature could be given by other factors such as the heating method adopted (several short laser exposures as in Aquilanti et al. [11] or continuous laser ramp as in Anzellini et al. [9]), systematic errors in the temperature measurement (the use of refractive optics as in Aquilanti et al. [11] or reflective optics as in Anzellini et al. [9]) or chemical reactions.

Therefore one of the purposes of this thesis is to apply the same criterion to other, less reactive, 3*d* metals in order to validate it or reject it. Nickel and cobalt are the best candidates: they are 3*d* metals very close to iron in the periodic table, sharing the same face centred cubic crystal structure before melting and up to 90 GPa, and are among the elements composing the Earth's core. The laser heating system used to heat the DAC and to detect the temperature is the same one employed by Aquilanti et al.[11].

3.2.2 XAS probing melting at extreme conditions

With X-ray absorption spectroscopy the melting is identified through a clear characteristic change of the XANES region of the spectrum. When the edge shoulder flattens and the first two oscillations disappear the sample is considered molten, see the bottom panel of Figure 3.4a.

Examples of the changes occurring in the XANES and EXAFS regions at different pressures are shown for nickel in Figure 3.5. In cobalt the same changes occur, and they are shown in Figure 3.6.

In this work, the onset of melting was determined *in-situ* by observing the evolution of the XANES region of the collected spectra. The horizontal size of the beam probing the XANES at the K edge of nickel or cobalt is about 3 μm. The volume of the sample measured by X-rays and in which melting is detected is then $3\times6\times4$ μm^3 (horizontal beam $\times$ vertical beam $\times$ sample thickness).

The XANES spectra were normalized setting to 0 the absorption just below the Ni K-edge (point $\mathrm{E_b}$ in Figure 3.4), and to 1 the absorption above the edge and immediately following the first two oscillations (point $\mathrm{E_a}$ in Figure 3.4). The following

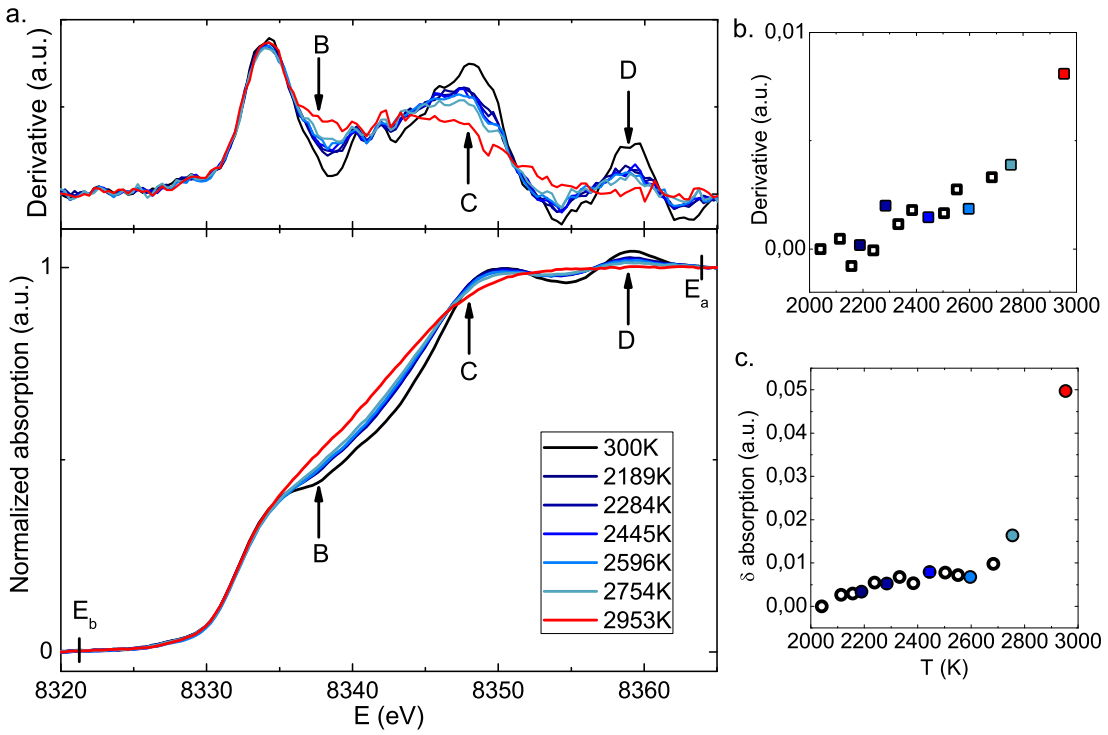

Figure 3.4 – X-ray absorption spectroscopy melting criterion shown for nickel at 52 GPa. (a.) In the bottom panel the points E_b and E_a indicate where the normalization was performed. The absorption at point E_b, below the edge, is set to 0 while the absorption at point E_a, above the edge, is set to 1. The melting criterion consists in the disappearance of the shoulder at point B and the flattening of the two oscillations at points C and D. This can also be seen in the derivative shown in the top panel. The flattening of the derivative at points B, C and D, is the signature of melting. (b.) The variation of the derivative at the energy of point B (E=8338 eV) is plotted as a function of temperature with empty squares. The filled symbols represent the spectra that are plotted in the left panel with the same colour. A discontinuity in the derivative appears in correspondence of the melting. (c.) The variation of the absorption as a function of temperature at point B (E=8338 eV) is shown as a function of temperature with empty circles. As in (b.) the filled symbols are the ones associated to the spectra plotted in the left panel. A discontinuity in the T-scan appears in correspondence of the melting, as in Figure 3.3.

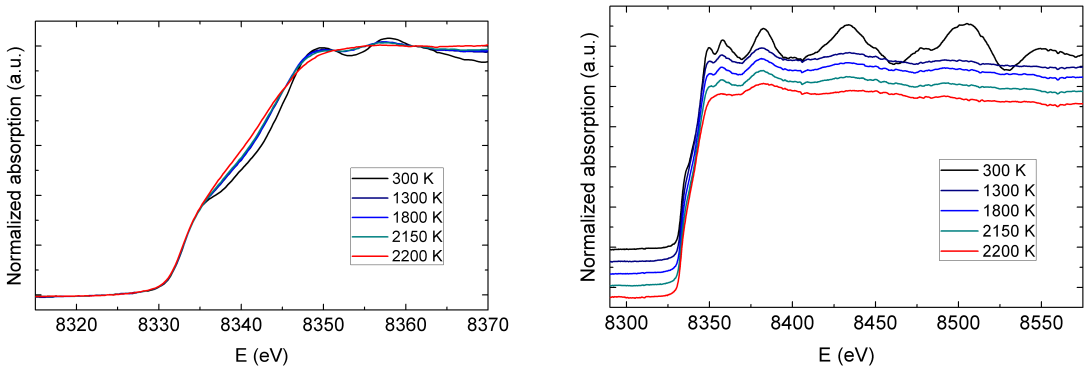

(a) XANES at 11 GPa.

(b) EXAFS at 11 GPa.

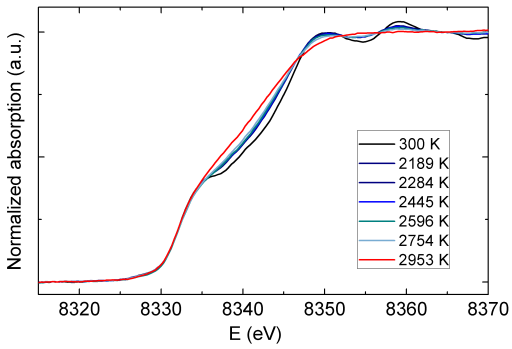

(c) XANES at 52 GPa.

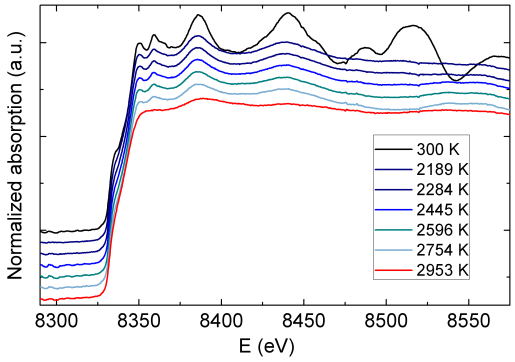

(d) EXAFS at 52 GPa.

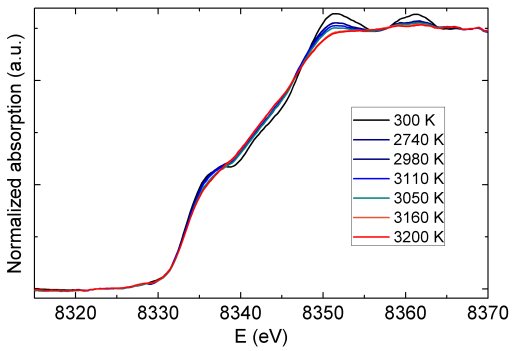

(e) XANES at 87 GPa.

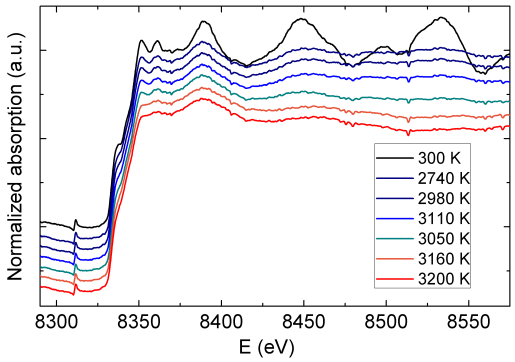

(f) EXAFS at 87 GPa.

Figure 3.5 – Melting of nickel at high pressure. Black spectra are at 300 K, blue and green spectra are hot solids, orange are a solid-liquid mix and red are liquid.

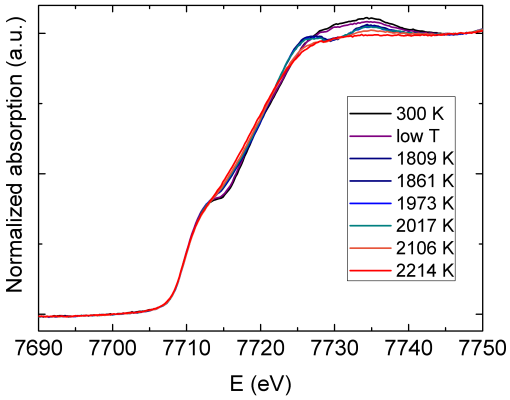

(a) XANES at 14 GPa.

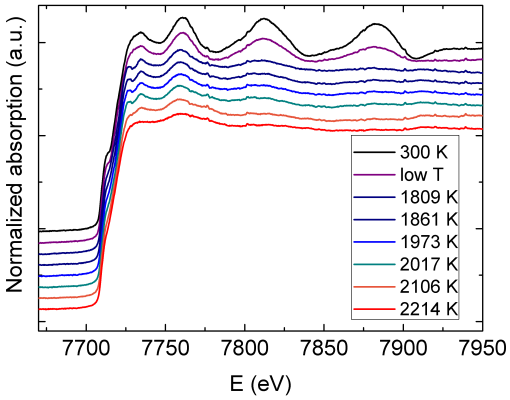

(b) EXAFS at 14 GPa.

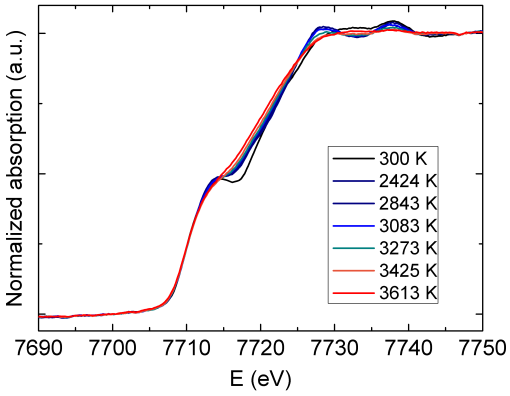

(c) XANES at 80 GPa.

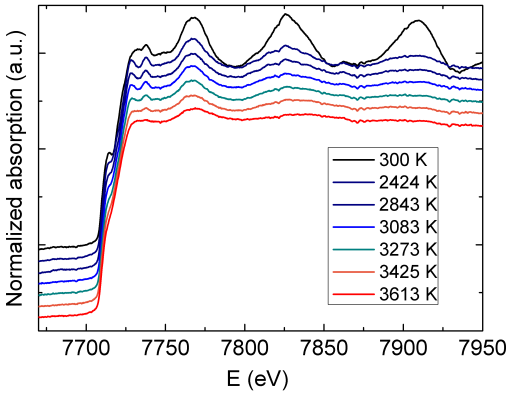

(d) EXAFS at 80 GPa.

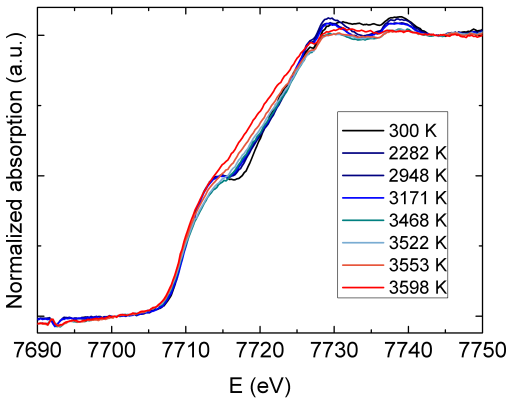

(e) XANES at 110 GPa.

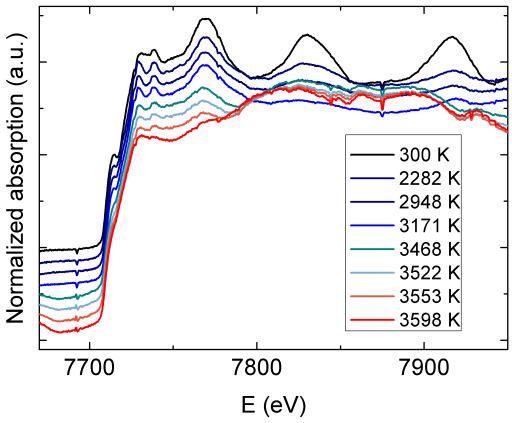

(f) EXAFS at 110 GPa. Due to the distortion of the spectra at high temperature, it is not possible to analyse the EXAFS in this run.

Figure 3.6 – Melting of cobalt at high pressure. Black spectra are at 300 K, violet are hot solids in the hcp phase, blue and green spectra are hot solids in the fcc phase, orange are a solid-liquid mix and red are liquid.

formula was used:

$$\mu_{\mathrm{normalized}}(\mathrm{E}) = \frac{\mu_{\mathrm{raw}}(\mathrm{E}) - \mu(\mathrm{E_b})}{\mu(\mathrm{E_a})}.$$

In this way, small changes in the thickness of the sample were normalized and thus neglected.

This melting criterion was applied to data from each heating run and the temperature of the first spectrum which shows these changes was considered as the melting temperature $\mathrm{T_M}$. Most of the times, even if the laser power was increased slowly, the observed transition between solid and liquid was sharp. However, in some cases, probably due to thermal gradients, the melting signature appears gradually due to a solid/liquid coexistence in the sample. The laser-matter interaction occurs at the surface of the sample and here is where the first nucleation of melting appears [65]. The temperature is measured at the surface of the sample as well. For this reason, even if X-rays probe mixed phases of the sample and the volume of the liquid is small compared to the volume of the solid, as soon as there is a small signature of liquid in the XAS spectrum, the temperature measured is the temperature of the first melting.

In this thesis, the criterion was validated experimentally and theoretically. An *ex-situ* analysis was performed using a focused ion beam (FIB) and a scanning electron microscope (SEM) on the recovered sample. The procedure is described in Section 3.2.3. Theoretically, the disappearance of the shoulder and the flattening of the two oscillations can be interpreted as the manifestation of a large number of different local atomic configurations forming in the liquid phase. The physical phenomena producing changes in the XANES will be shown in Section 4.6.

The discontinuity observed in the absorption spectrum upon melting can be used to follow the phase transition as a function of temperature. This is the basis of the T-scan method introduced at the beginning of this section.

An example of this method, applied to the data in this work, is represented in Figure 3.4c, where the variation of the absorption coefficient at point B (E=8338 eV) is represented as a function of temperature. The same is true for the derivative of the spectrum, shown in the top panel of Figure 3.4a, where the trend of point B as a function of temperature is shown in Figure 3.4b. The sudden jump of these trends as a function of temperature represents the transition to the liquid phase. However in some cases, probably due to thermal gradients, the melting signature appears gradually due to a solid/liquid coexistence in the sample. The T-scan method is very accurate if the XAS spectra are not deformed with temperature, but at the extreme pressures and temperatures used in this work, this is not always achieved and having the possibility to record the full energy range of the XAS spectrum is an asset in these difficult situations.

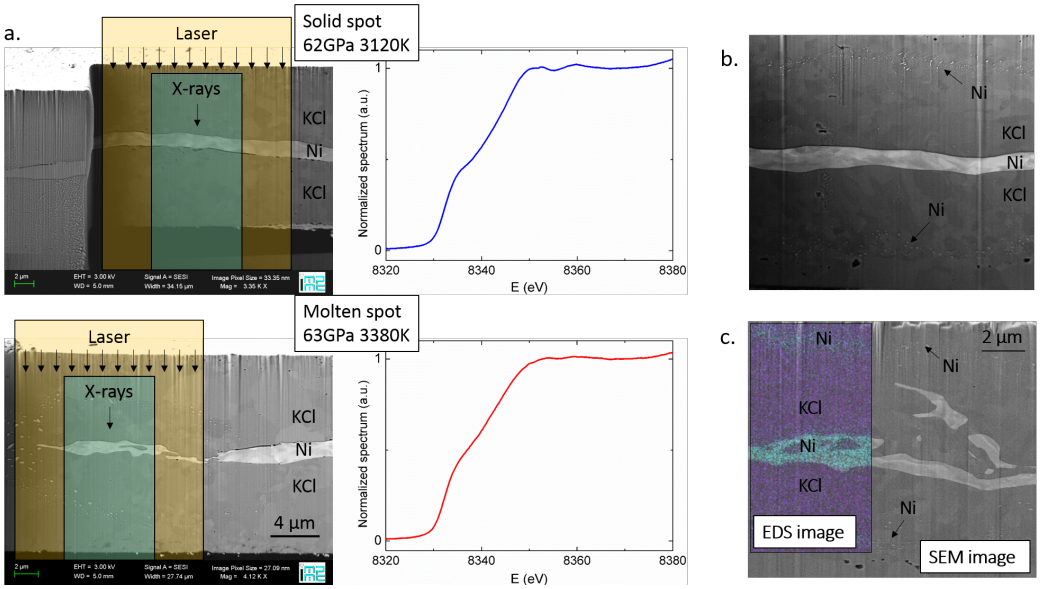

Figure 3.7 – (a.) FIB and SEM melting criterion. In the first image in the top-left panel, the borders of the sample foil are intact, corresponding to a heating temperature below the melting. In the bottom-left panel, a liquid with its characteristic irregular shape is shown. For both images, the corresponding XAS spectra are shown in the right panel. (c.) A SEM and an EDS image are superimposed to show the composition of the cut. Some nickel diffused from the sample by Soret effect [145] into the KCl both for the solid (b.) and the liquid (c.) heated spot.

3.2.3 Post analysis validation on nickel samples

Some of the nickel samples were recovered after the experiment, and cross sections of the laser-heated hotspots were prepared by focused ion beam (FIB) milling. The exposed cross sections have been imaged using the scanning electron microscope (SEM). This was done in collaboration with G. Morard [1].

This method has already been used to confirm the melting of tantalum and iron alloys [83, 113], where the shape and the texture of the exposed cross section revealed if the sample was molten or not. The shape of the cross section of a solid or liquid heated spot are indeed noticeably different, see Figure 3.7a. Performing the cut at different depths gives an idea of the three-dimensional sample texture through the heated spot. In the case of the solid, the borders of the sample foil remain the same as for the unheated sample. The section of a liquid shows a significant unevenness with, very often, a non-uniform thickness. The variation of shape is due to surface tension, which distinguishes the behaviour of liquid from solid matter. In Figure 3.7a, the X-ray spot size is indicated in comparison with the laser spot size inferred from

1. Guillaume Morard, IMPMC, Paris.

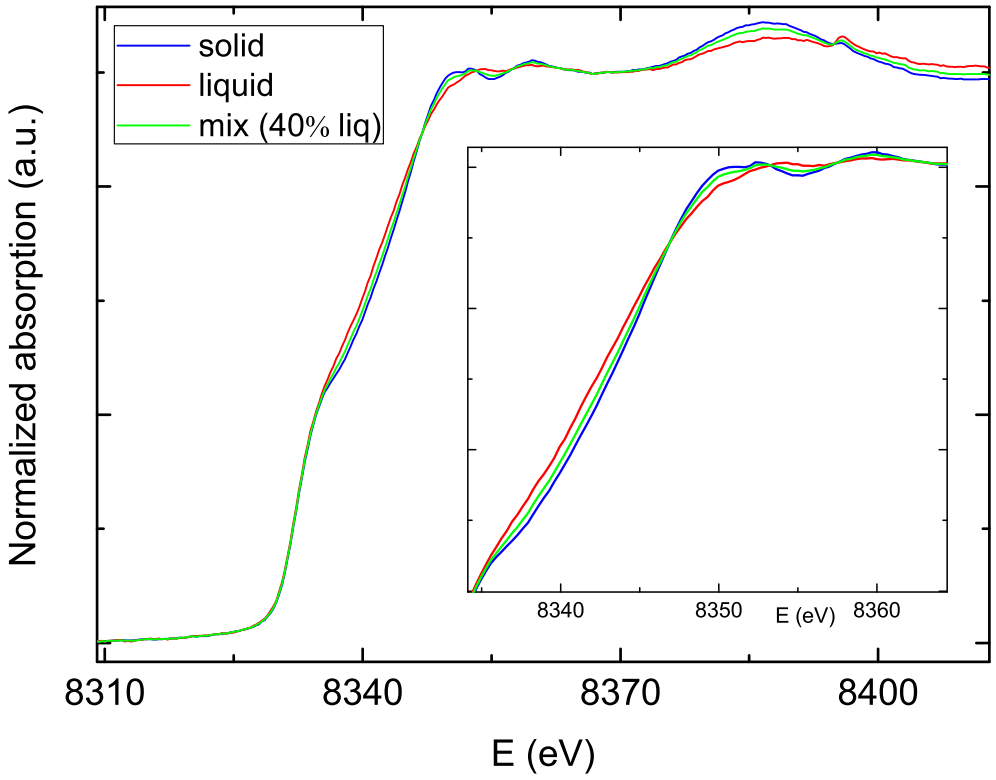

Figure 3.8 – The spectrum of solid nickel at 62 GPa and 3120 K is plotted in blue together with the first spectrum of liquid nickel at 63 GPa and 3380 K in red. The spectrum represented in green is what we would normally consider as mixed and it is generated as a linear combination of the two spectra, with a proportion of 40% liquid and 60% solid.

the shape of the sample. This represents approximately three times the X-ray beam size, minimizing temperature gradients in the measured X-ray spot area.

In both cases, the section of the heated spot is surrounded by droplets of diffused nickel, see Figure 3.7b. The nature of these diffused droplets has been verified with Energy Dispersive Spectrometry (EDS) analysis. The presence of this contour helps in recognizing the heated spot even when the sample was a hot solid. Solid migration is due to the Soret effect [145].

For the six samples post-analyzed with this method, the observed features confirmed the corresponding XAS interpretations. In some cases, the shape of the sample was only slightly deformed with respect to the solid, corresponding to a solid-liquid mix.

Thanks to this post analysis we were able to evaluate the minimum volume of liquid that would be visible in the detection of melting. With this analysis we could

in fact confirm that the two spectra shown in Figure 3.7 are as a matter of fact the spectrum of hot solid just below the melting curve, and a liquid just above the melting temperature. In Figure 3.8 is represented in green a linear combination of a hot solid and a liquid generated as

$$\mu_{\mathrm{mix}} = \mu_{\mathrm{liquid}} \cdot \mathrm{x} + \mu_{\mathrm{solid}} * (1 - \mathrm{x}),$$

where x is the proportion of liquid. We noticed that we would consider the sample mixed when the proportion of liquid is about 40%.

3.3 Melting curve of nickel

The melting curve of nickel was measured probing the sample with XAS at different pressures and temperatures. X-ray spectra were collected around the K-edge of nickel, at 8333 eV. The experiment was performed as described in Section 2.6. The results are shown in Figure 3.9, alongside those curves from the literature that show the best agreement.

The points of the pressure-temperature phase diagram probed in this study are illustrated in Figure 3.9. A melting temperature measured with a heating run is accepted only if the XANES at room temperature before and after melting are exactly the same and if the EXAFS oscillations show the same frequencies. Otherwise, the melting temperature cannot be accepted: sample modifications such as chemical reactions could have occurred.

The temperatures for the solid/mix/melt at different pressures are indicated in Figure 3.9 by blue/orange/red symbols respectively. The white square symbols correspond to the pressure and temperature conditions for which the state of the sample was confirmed with the FIB and SEM *ex-situ* analysis. All the six spots that were checked with FIB and SEM confirmed the interpretation given by XAS. Even in the case of a mixed phase it was possible to detect that the sample had liquefied, but only partially.

The two points represented in the phase diagram with triangles are points where a small reaction occurred. In Figure 3.10a the absorption spectrum before and after heating of the point at 100 GPa is shown. While the difference in the background could be due to a change in the thickness of the absorption spectrum, the change in the XANES could be indicative of a chemical reaction. XRD performed on the recovered sample showed the presence of NiO, see Figure 3.10b. It is possible to evaluate the quantity of NiO in the sample with a linear combination of reference spectra of

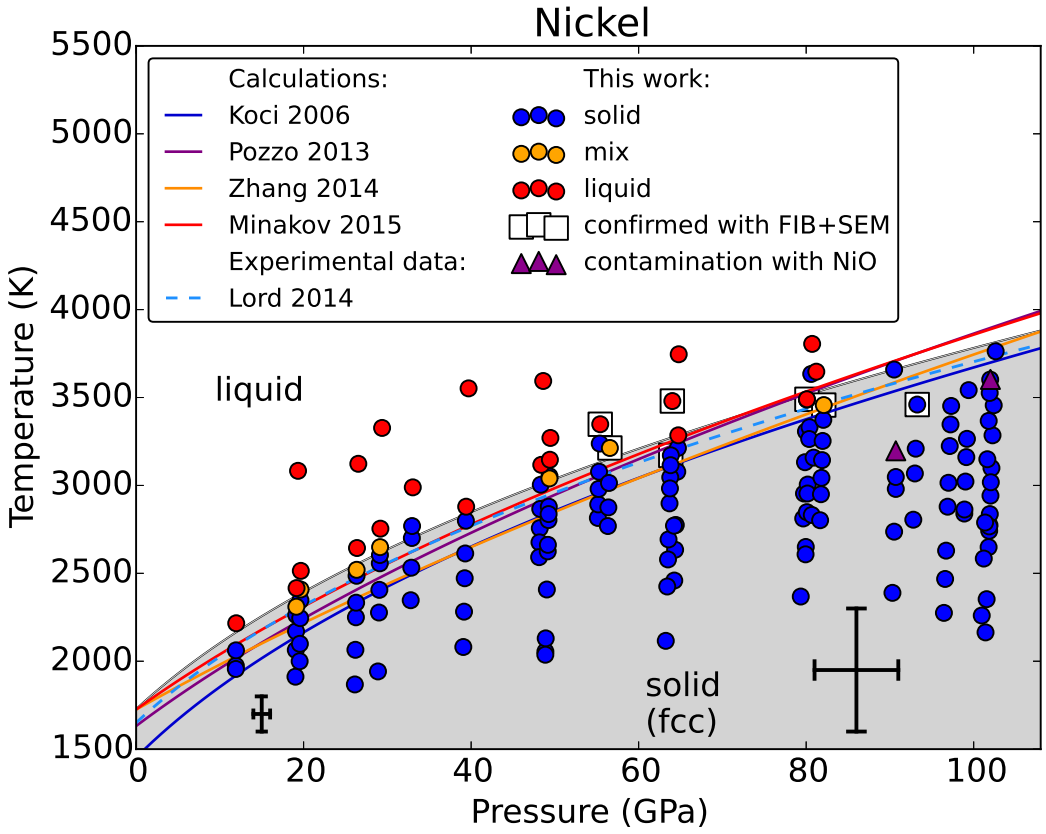

Figure 3.9 – Nickel phase diagram measured by means of X-ray absorption spectroscopy [22]. Blue, orange and red symbols represent the pressure and temperature conditions of solid, mixed and liquid phases respectively. The white squares are the pressure and temperature conditions for which the state of the sample was confirmed by FIB and SEM post analysis. The curve dividing the grey and the white regions is the Simon-Glatzel fit of the data. Only experimental and theoretical works showing a good agreement with our data set are presented [100, 88, 127, 173, 112]. The two liquid points after 85 GPa, marked with triangles, are discussed in the text.

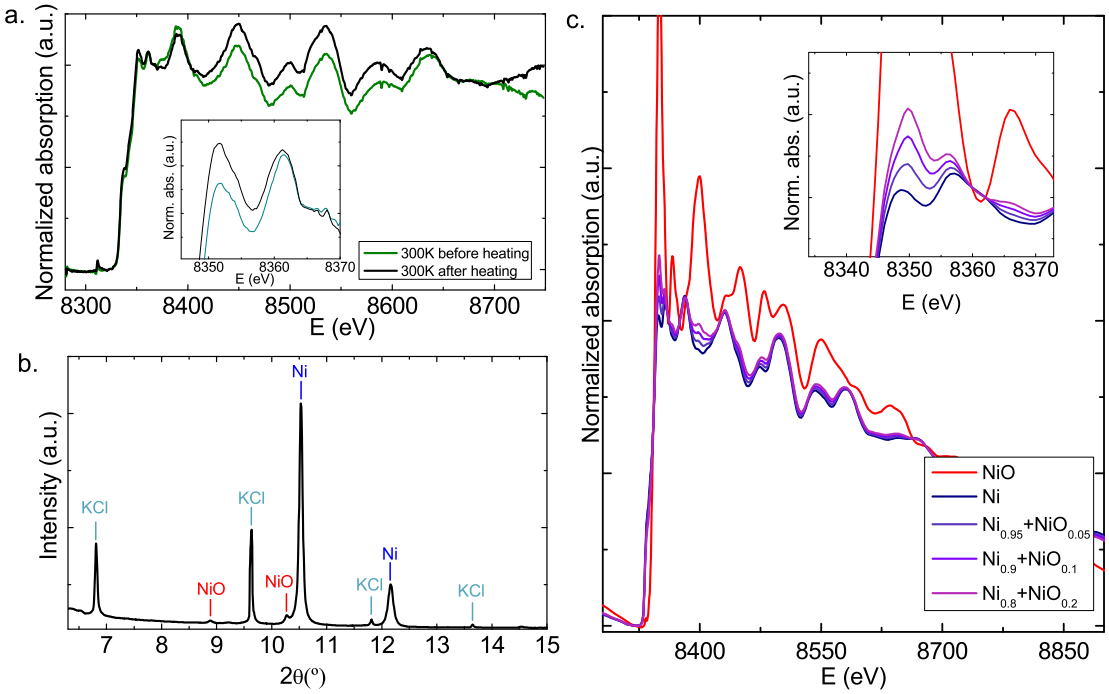

Figure 3.10 – (a.) XAS measured at 100 GPa before and after heating (and melting). The first oscillation in the spectrum after heating (highlighted in the insert) is higher than before heating. This corresponds to a content of NiO of approximately 7%. Note that this quantity of NiO does not change the main frequency of the oscillations in the EXAFS. (b.) The sample was recovered and an XRD map was performed at ambient conditions. This pattern corresponds to the point measured at 100 GPa. (c.) Combination of a pure nickel spectrum and a NiO spectrum. The two are reference spectra measured on the bending magnet beamline BM23. From the linear combination of the two spectra it is possible to evaluate the effect of a certain quantity of NiO on the spectrum.

Ni and NiO that were previously measured on the beamline BM23. By comparing the shape of the XANES in Figure 3.10a with the one in Figure 3.10c we evaluated the content of NiO in the sample to be about 7%. This quantity is enough to have an influence on the melting curve, as in the case of iron studied by Morard et al. [115], but is not enough to have an influence on the main frequency of the EXAFS.

The error in the temperature was always determined using the two-color fit, see Section 2.5.2. A linear relation between the temperature bilateral error (TE) and the melting temperature itself (T) was found:

$$\mathrm{TE} = 0.19 \cdot \mathrm{T} + 270, \tag{3.1}$$

where both TE and T are expressed in Kelvin. The points are represented in Figure

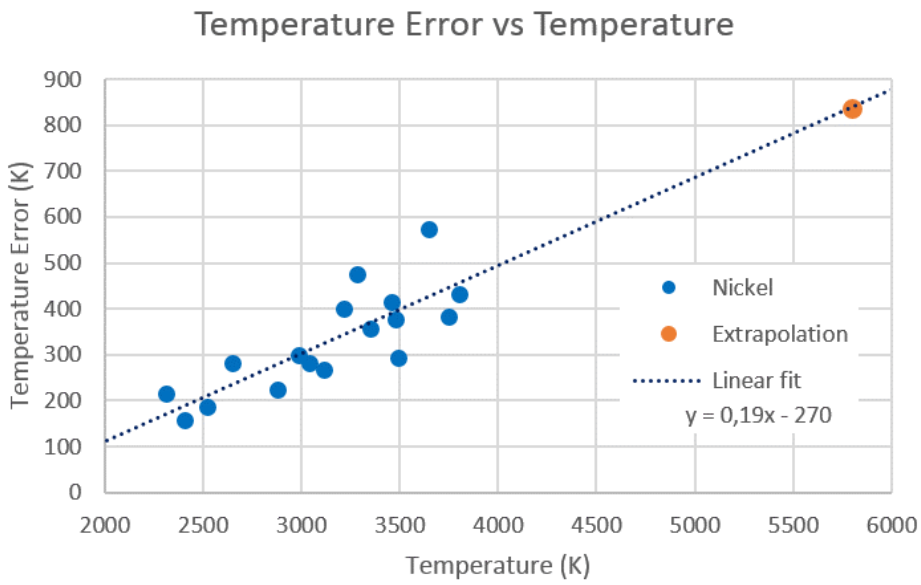

Figure 3.11 – Temperature bilateral error bar as a function of temperature. The red point represents the extrapolation at 5800 K, the melting temperature of nickel at the ICB.

3.11. In Figure 3.9 the error bars are represented accordingly.

This study is compared with previous experiments and calculations found in the literature. Within the experimental error, our data is in good agreement with the experimental data recently measured by XRD [100], where in each heating run the sample was heated continuously for 5-15 minutes at increasing temperature. There is a very good agreement also with some of the theoretical works such as molecular dynamics simulations using the embedded atom method with Mendelev's potential [173], first-principle calculations based on density functional theory [127, 112] and non equilibrium molecular dynamics simulations to study shock induced melting in nickel [88].

The good agreement between the melting determined by XRD [100] and this work shows that for nickel neither the heating method (continuous laser ramp or several short laser exposures), neither the optics used for the temperature measurement (reflective or refractive), nor the X-ray technique employed (XRD or XAS) introduce a technical bias in the determination of the melting temperature. With these techniques, two different facets of the same process are measured: XRD detects melting through the loss of long range order, whilst XAS melting is detected through the appearance of different local configurations. Unlike with XRD, with XAS no signature of

fast recrystallization is present.

A fit of the data to a Simon-Glatzel equation, presented in Appendix B.0.1, gives

$$\mathrm{T_M(K)} = 1728 \times \left[\frac{\mathrm{P_M}}{15 \pm 3} + 1\right]^{\frac{1}{2.60 \pm 0.02}}.$$

The errors in the curve are defined performing the fit of the temperature data plus or minus half of their error (the error is bilateral). The extrapolation of the melting temperature to P = 330 GPa, the ICB pressure, gives a temperature of 5800 $\pm$ 410 K. The error is given by the propagation of the temperature error along the curve in Equation 3.1. Despite the slight differences between the two data sets, our extrapolated value is the same as the one found by Lord: 5800$\pm$700 K [100].

3.4 Melting curve of cobalt

The melting curve of cobalt was determined, as for nickel in Section 3.3, by probing the phase diagram at different pressures and temperatures.

X-ray absorption spectra were collected around the K-edge of cobalt at 7709 eV. The points of the pressure and temperature phase diagram probed are represented in Figure 3.12, alongside other curves found in the literature. For cobalt as well, the melting run was accepted only if the XANES of a room temperature spectrum as well as the frequencies of the oscillations of the EXAFS were the same before and after the melting. The temperatures for the solid/mix/melt at different pressures are indicated by blue/orange/red symbols respectively. The temperature error of the liquid points is determined with the two-color fit and gives the following linear relation with temperature:

$$\mathrm{TE} = 0.155 \cdot \mathrm{T} + 171, \tag{3.2}$$

where TE is the temperature bilateral error and T is the melting temperature, both expressed in Kelvin.

A fit of the data to a Simon-Glatzel equation gives

$$\mathrm{T_M(K)} = 1775 \times \left[\frac{\mathrm{P_M}}{29 \pm 4} + 1\right]^{\frac{1}{1.93 \pm 0.05}}$$

The errors in the curve are defined in the same way as for nickel. The theoretical curve by Zhang using Zhou's potential shows the best agreement with our experimental result. An extrapolation of the melting curve to 330 GPa, the ICB pressure, gives a temperature of 6500$\pm$420 K, 700 K higher than the one obtained with nickel. The error was found by extrapolating the linear relation in Equation 3.2.

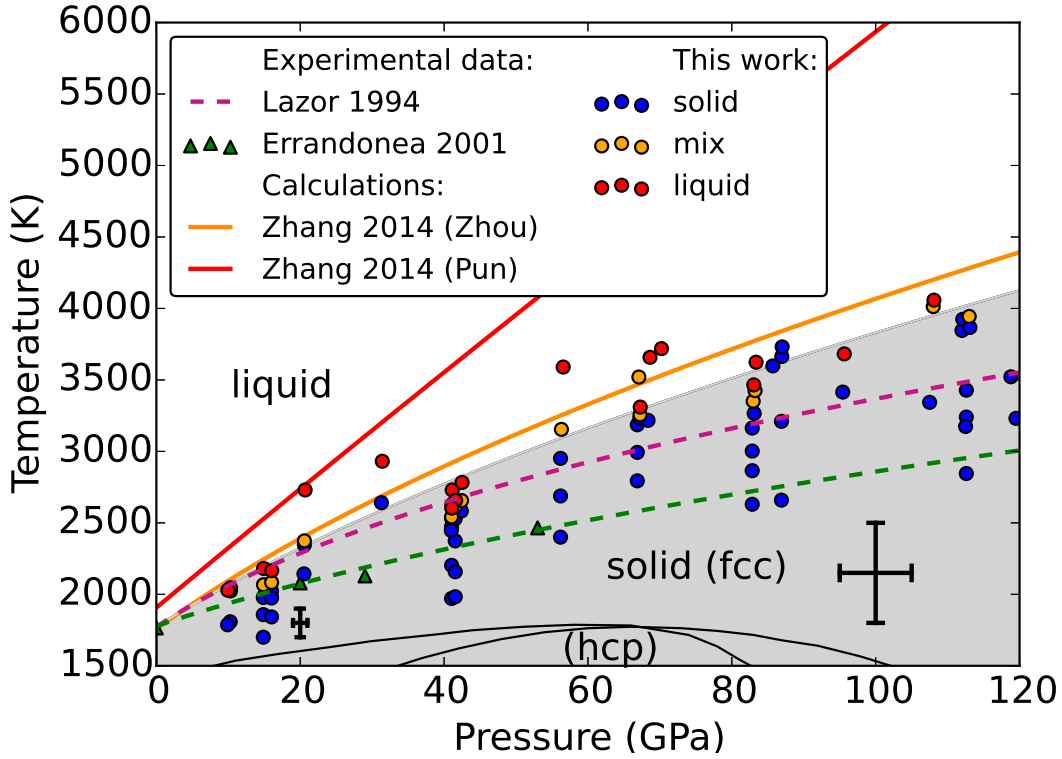

Figure 3.12 – Cobalt phase diagram measured by means of absorption spectroscopy. Blue, orange and red symbols represent pressure and temperature conditions of the solid, mixed and liquid phases respectively. The curve dividing the grey and white regions is the Simon-Glatzel fit of the data. Our melting curve is in between Zhang's calculations using Zhou's potential [174] and Lazor's curve measured using visual observation of speckle movements [93].

3.5 Details on the effect of melting on XANES and EXAFS spectra

With the purpose of finding other melting criteria by X-ray absorption spectroscopy, we looked for other reproducible changes that occur during melting.

Derivative of the absorption spectrum

A sharp change in the XANES is reflected by a change in its derivative. In Figure 3.13c the value of the derivative is shown as a function of temperature for the energy corresponding to point B of Figures 3.4 and 3.13b. The percent variation of the derivative between the solid and the liquid is system dependent and for nickel it is equal to 62±3 %. It was calculated as

$$\frac{\mathrm{d}(\mathrm{T_{molten}}, \mathrm{P}) - \mathrm{d}(300\ \mathrm{K}, \mathrm{P})}{\mathrm{d}(\mathrm{T_{molten}}, \mathrm{P}) + \mathrm{c}(\mathrm{P})}$$

where $\mathrm{d}(\mathrm{T}, \mathrm{P})$ is the value of the derivative and $\mathrm{c}(\mathrm{P})$ is a pressure dependent constant. This constant, calculated as $\mathrm{c}(\mathrm{P}) = \mathrm{d}(300\ \mathrm{K}, 0\ \mathrm{GPa}) - \mathrm{d}(300\ \mathrm{K}, \mathrm{P})$, takes into account that the shape of the edge region changes with pressure, in particular the shoulder becomes more prominent as the pressure increases. The value of $\mathrm{d}(300\ \mathrm{K}, \mathrm{P})$ goes from 0.004 at 10 GPa to -0.007 at 100 GPa.

These values, even if they can give an indication of the phase of the sample, are not enough for a blind determination of the phase.

Fourier transform of the EXAFS signal

The analysis of the EXAFS is not always possible since in some cases, during melting, the absorption data has uneven background due to changes in the sample shape. While changes in the XANES, whose range in energy is shorter, are still appreciable, changes in the EXAFS are harder to detect.

When the background of the spectrum remains smooth, as in Figure 3.13a, it is possible to extract the EXAFS signal and perform a Fourier transform, see Figure 3.13d. Figure 3.13e shows the value of the maximum of the Fourier transformation as a function of temperature. The smooth decrease in intensity observed as the solid heats up (due to the increased thermal variations) is abruptly interrupted by a sharp dip.

This criterion works well when the background of the XAS spectrum is smooth,

but it becomes impractical in the case of more complicated backgrounds or backgrounds changing with temperature. In practice this method could become useful if the XANES region is hidden by a big glitch. In the other cases it can be considered complementary to the XANES melting criterion.

3.6 Critical issues

In this chapter were shown examples of melting runs that are relatively straightforward to interpret. However it is fair to mention the critical issues that can be encountered when performing laser heating experiments with X-rays and especially when using absorption spectroscopy as a probe.

Alignment

The alignment of X-rays, laser hot spot and pinhole for the pyrometry has to be very precise and must be maintained throughout the experiment. A misalignment of a few microns could lead to misreading the temperature and thus to an underestimation or an overestimation of the melting temperature [66]. For this reason the melting temperature obtained can be accepted only if before and after the heating run X-rays, hot spot and pinhole are still aligned. The maximum misalignment accepted is $3\ \mu$m. We noticed that the alignment is better preserved during the heating run if the DAC is cooled down with a chiller to about 17 °C.

Background

During laser heating the sample can lose its uniformity and become very inhomogeneous, leading to an uneven background. This not only causes non-negligible difficulties in the extraction and interpretation of the EXAFS, see Section 5.7, but also makes it more difficult to interpret the melting. Normally the problem can be overcome by choosing suitable points $\mathrm{E_b}$ and $\mathrm{E_a}$ for the normalization, but in some - fortunately rare - cases the heating run has to be discarded.

Temperature measurement

It is very difficult to obtain the same melting temperature on the same spot after the first melting. When the laser power is decreased and then increased again, after the first melting the sample melts again but very often at different temperatures. This

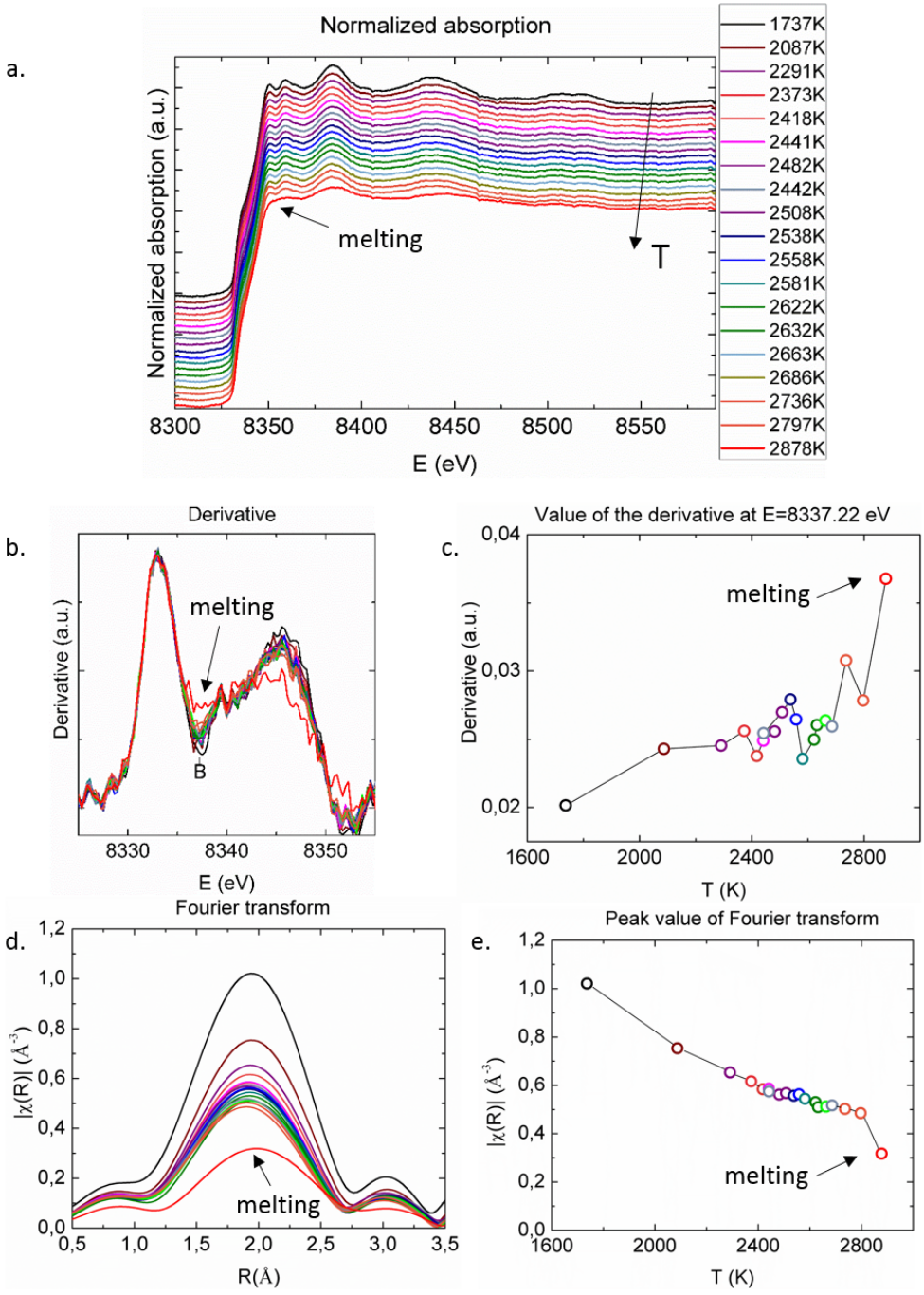

Figure 3.13 – Melting signatures for nickel at 35 GPa. The normalized absorption (a.), the derivative of the normalized absorption (b.) and the Fourier transform of the EXAFS signal (d.) are shown. In plot (c.) the trend in temperature of the value of the derivative (b.) at the energy value E=8337.22 eV is highlighted. In (e.) the value of the peak of the Fourier transform (d.) is plotted as a function of temperature.

discrepancy could be due to sample modifications or to a change in emissivity. In the first case a lower melting temperature could mean that the sample became thinner. If only the superficial part of the sample melts, the portion of hot solid in the bulk would be smaller in a thinner sample, leading to an earlier detection of melting.

Insulation

If the pressure medium (KCl) embedding the sample is not perfectly homogeneous, the differences of thermal insulation at different positions could lead to a non-homogeneous laser hot spot. Fortunately this problem can be overcome using KCl discs of the needed size cut with a femtosecond laser [2]. The diameter of the disk is normally equal to the one of the gasket hole, and its thickness typically $\sim$10 μm.

Moreover, in other cases it becomes very difficult to increase the temperature, even when not associated to a melting signature in the XAS (as it should be according to the temperature versus laser power melting criterion). We interpret this as a thinning of the insulating material. The lack of insulation could lead to difficulties in heating the sample.

Sometimes the melting signature appears after the temperature starts decreasing. In these cases we consider the highest temperature reached to be the melting point.

For all these reasons it is very important to pay particular attention to the alignment, check with the two-color fit the thermal gradients and heat every time a new and intact part of the sample. The use of FIB and SEM can be very useful not only as melting diagnostics but also to be aware of the sample conditions after heating.

3.7 Conclusions

In conclusion, XAS has been proven to be a suitable method for detecting melting for 3d metals whose crystalline structure in the hot solid phase is face centred cubic.

The discrepancy found in the melting curve of iron between X-ray diffraction and X-ray absorption is thus not due to the criteria themselves. The effect of reflective and refractive optics has been extensively examined at the ESRF as a side project in collaboration with a master student R. Giampaoli [3]. Differences between the two optics are observed for T $>$ 3000 K, but are much smaller than the ones measured for iron and in the opposite direction [66, 67]. We thus conclude that the melting curve

2. KCl discs were prepared and provided by Guillaume Morard, IMPMC, Paris.
3. Ruggero Giampaoli, Politecnico di Milano, Italy

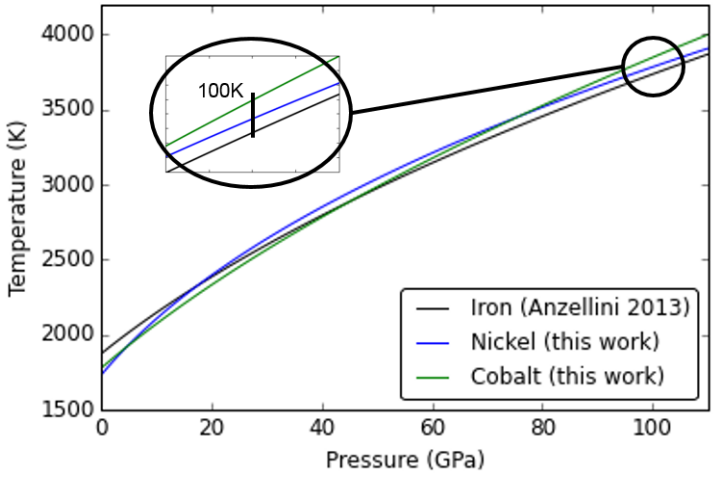

Figure 3.14 – The melting curve of iron obtained with X-ray diffraction is compared with the melting curve of nickel and cobalt obtained with X-ray absorption in this work.

discrepancy is not due to the optics used either.

Finally, it is possible to compare the melting curves of iron, nickel and cobalt. For iron it was chosen the melting curve obtained by X-ray diffraction measurements [9], while for nickel and cobalt the ones presented in this work. In Figure 3.14 the three curves are plotted in the same graph. In the range of pressure studied they follow quite closely one another and at 100 GPa they differ by only 100 K, which is much lower than the error bar in our measurements (about $\pm$500 K for nickel at 3800 K).

In our measurements we do not notice any dependence of the number of 3d electrons on the slope of the melting curve. The experimental evidence that gave rise to the semiempirical models connecting the number of *d* electrons to the slope of the melting curve (see 1.2) is thus questioned. Moreover, it is known that nickel content in the Earth's outer core is $\sim$5-10wt%, we can thus compare our experimentally determined melting temperature of nickel to the one of pure iron at 90 GPa, in order to check the effect of nickel in the determination of the temperature at the ICB. Assuming a linear relation between the two endmembers, as supported by the existence of solid solution in the Fe-Ni binary system [90], we obtain an increase of 2 K/wt% Ni of the melting temperature of pure Fe, therefore the effect of Ni may be to increase the melting temperature of the Earth's core of $\sim$10-20 K. This is one order of magnitude lower than the effect of light element such as S, C or O [113] at 90 GPa and in the opposite direction, and is, again, much lower than the sensitivity of our measure-

ments. In conclusion, the effect of nickel can be neglected during the discussion of temperature profile and melting relations under Earth's core conditions.

Chapter 4

Ab initio calculations of X-ray absorption on cobalt

Ab-initio calculations were performed to support and understand our experimental findings and are presented in this chapter. After a brief section on the state of the art of calculations reproducing X-ray absorption near edge structures on iron, the theoretical methods adopted in this work to generate atomic supercells of cobalt and simulate spectra are presented. The validation of the XAS melting criterion is shown and explained. The same atomic supercells are used to calculate and compare the density of states of a hot solid and a liquid at the same pressure.

4.1 State of the art

Performing *ab initio* calculations provides a very powerful tool to understand the structural and electronic modifications that take place in a phase transition at specific pressure and temperature conditions.

Since X-ray absorption was proposed to be a suitable technique to study melting at high pressure [23], several theoretical studies were performed on iron, with the aim of reproducing and understanding the changes in the XANES region that occur in the bcc to hcp, hcp to fcc and in the solid to liquid transitions [129, 130, 105, 107, 157]. The main result of these studies is that due to the very different features of bcc, hcp, fcc and liquid spectra, XANES can detect solid-solid and solid-liquid transitions of iron under pressure. In particular, an experimental resolution of $\sim$1 eV is enough to discriminate between the different phases at pressure-temperature conditions such as the ones at the Earth's core [107]. According to the calculations, XAS can thus be accepted as a suitable technique to detect melting in iron [129, 130, 107].

The purpose of this work is to perform *ab initio* calculations on cobalt to reproduce the changes in the absorption spectra that occur in the solid-liquid transition, with the aim of validating for cobalt the melting criterion used in this work and discussed in Section 3.2. Theoretically validating the criterion for another transition metal allows to extend it to other similar materials. It is known that materials with analogous atomic properties sharing the same structure have very similar absorption spectra [146].

AIMD calculations on cobalt also provide the radial distribution function at different pressure and temperature conditions and a theoretical evaluation of the compression of cobalt under pressure, as shown in Chapter 5.

Moreover, in the above mentioned theoretical studies on iron, only the absorption spectra and the density of states already averaged on several atomic sites are shown. In order to have a deeper understanding of the structural and electronic changes associated to the phase transition, we believe that showing the spectra associated with different photoabsorbers can help in unravelling the local transformations that occur during melting.

4.2 Methods

In order to understand the changes at the atomic scale that occur in the transition between the solid and the liquid phase, density functional theory (DFT) based ab initio molecular dynamics (AIMD) simulations have been performed and statistically independent samples of the resulting structures were used as input to many-body theory spectral calculations.

The purpose of this section is not to enter into too much detail of the calculations, but to give a general overview of the procedure adopted. The case of cobalt will be used to illustrate the method.

AIMD simulations were performed in the NVT ensemble on cobalt supercells for several points in the temperature-pressure space. Statistically independent samples of the equilibrated ensembles were used to generate radial distribution functions, calculate the K-edge XANES spectra and the projected density of states for the absorption final-state. In the following sections, the different steps are more fully described.

4.2.1 Molecular Dynamics Simulations

The first step consists of the definition of an initial supercell containing a chosen number of atoms of the desired species ordered with an initial crystallographic phase; periodic boundary conditions are enforced. The simulation is done in the NVT thermodynamics ensemble such that the number of atoms (between 32 and 128) is conserved and specified volume and temperature are maintained. The atoms positions are evolved in time according to Newtonian dynamics with forces obtained from a DFT calculation at each time step. The temperature enforced during the simulation provides thermal disorder. For a given density-temperature, the pressure was obtained as result of the simulation. This procedure can be repeated as many times as needed (between 100 and 1000 times) and each of the configurations will be referred to as thermodynamic configuration.

In AIMD, the interactions between nuclei obey classical mechanics, but the interactions between electrons are calculated *ab-initio* by means of DFT. MD calculations based on DFT require more computing power than those using classical effective potentials, but they give a more accurate result.

This work was done in collaboration with the theoretician V. Recoules [1]

4.2.2 Radial distribution function

The set of coordinates from the molecular dynamics simulation were used to calculate the radial distribution function (RDF) or g(r) that describes the distribution of distances between pairs of particles, in this case atoms, contained in a given volume. In other words, the g(r) describes the probability of finding an atom in a shell dr at a distance r from another atom chosen as reference. The number of atoms that are enclosed in a shell with internal radius r and external radius $\mathrm{r} + \mathrm{dr}$ can be expressed as

$$\mathrm{dn(r)} = \frac{\mathrm{N}}{\mathrm{V}}\mathrm{g(r)}4\pi\mathrm{r}^2\mathrm{dr}$$

and thus

$$\mathrm{g(r)} = \frac{\mathrm{dn(r)}}{\mathrm{dr}}\frac{\mathrm{V}}{\mathrm{N}}\frac{1}{4\pi\mathrm{r}^2} \tag{4.1}$$

where N is the total number of atoms in a volume V and their ratio is the number density.

The calculation of radial distribution functions does not require much computing power and in the framework of this work was performed with a home-made python script. For each thermodynamic configuration the box was replicated 26 times around

1. Vanina Recoules, CEA/DAM-DIF in Arpajon, France

the original one, in order to have a supercube made of 3x3 boxes. The distances between each of the atoms in the central box and all the other atoms in the supercube are calculated and saved in a vector. At this point a matrix is generated whose first vector is **r**, the second is **dn** and the third is the **g(r)**. The vector **r** is a discretization of the space between 0 Å and the size of the box. In a generic element of vector **dn**, for example **dn[i]**, are counted the number of distances whose value is between r and $\mathrm{r} + \mathrm{dr}$, meaning how many distances have been found in the box that fit in the discretized space **r[i]**. The vector **g(r)** is then calculated using Equation 4.1. The g(r)s obtained for each thermodynamic configuration are then averaged in order to give the g(r) for that supercell. With this script the calculation of the g(r) from the given supercells could take few hours.

Alternatively the radial distribution function was calculated with the program Travis [27].

It is normally good practice to test several box sizes before proceeding with the generation of the atomic supercells at all the desired pressure and temperature conditions. Finding the smallest atomic supercell that still gives the same description of a system as one with more atoms would help in saving computing power and time. A way to determine if two atomic supercells are describing a system in the same way is to compare their radial distribution function; this is the way that was adopted in this work.

4.2.3 Calculations of XANES using the OCEAN code

The existing approaches to calculate absorption spectra can be divided into two categories: the ones that use single particle theories and the ones based on the treatment of many-body effects. The first approach, used by the well known code FEFF [131], is less demanding in terms of computing power. It is able to well reproduce the extended region of absorption, but it normally loses accuracy at the edge region. In order to describe the XANES region, where the many-body interactions are important, the second approach is required. The code used in this work, OCEAN (Obtaining Core Excitations form *Ab initio* electronic structure and NBSE) [162, 68], is based on this second approach and considers a two-particle picture.

For a basic understanding of the mode of operation of OCEAN two aspects have to be mentioned and are going to be briefly developed. The first one is that, while solving Equation 2.1, the final states are not calculated directly, but the problem is moved to an operator, called the propagator, whose function is to describe the probability amplitude for a particle to travel from one place to another in a given time, i.e. to propagate the excitation. The second one is that in the two-particle picture the

absorption is described including the single particle terms of the core hole and the excited photoelectron and the interaction between them.

The formalism that allows to describe the absorption process as a propagator acting on the initial states follows. Equation 2.1 in the dipole approximation can be rewritten with a slightly lighter formalism where $|\mathrm{i}>$ and $|\mathrm{f}>$ are the initial and final states, $\hat{\mathrm{d}}$ is the dipole operator, and where the density of states is described as a delta function.

$$\mu(\mathrm{E}) \propto \sum_{\mathrm{f}} |<\mathrm{f}|\,\hat{\mathrm{d}}\,|\mathrm{i}>|^2 \delta(\hbar\omega - (\mathrm{E_f} - \mathrm{E_i})) =$$

$$= \sum_{\mathrm{f}} <\mathrm{i}|\,\hat{\mathrm{d}}^{\dagger}\,|\mathrm{f}\times\mathrm{f}|\,\hat{\mathrm{d}}\,|\mathrm{i}>\delta(\hbar\omega - (\mathrm{E_f} - \mathrm{E_i})) \tag{4.2}$$

where the square has been expanded. The delta function can be written as the limit for $\gamma \to 0$ of a Lorentzian function [2], where γ is the inverse of the core-hole lifetime that gives the broadening of the features in the absorption spectrum. Equation 4.2 can thus be written as

$$\mu(\mathrm{E}) \propto -\mathrm{Im}\sum_{\mathrm{f}} \frac{<\mathrm{i}|\,\hat{\mathrm{d}}^{\dagger}\,|\mathrm{f}\times\mathrm{f}|\,\hat{\mathrm{d}}\,|\mathrm{i}>}{\hbar\omega - (\mathrm{E_f} - \mathrm{E_i}) + \mathrm{i}\gamma} = -\mathrm{Im} <\mathrm{i}|\,\hat{\mathrm{d}}^{\dagger}\,\hat{\mathrm{G}}(\omega)\,\hat{\mathrm{d}}\,|\mathrm{i}> \tag{4.3}$$

where

$$\hat{\mathrm{G}}(\omega) = \sum_{\mathrm{f}} \frac{|\mathrm{f}\times\mathrm{f}|}{\hbar\omega - (\mathrm{E_f} - \mathrm{E_i}) + \mathrm{i}\gamma}$$

is the Green function that propagates the excitation. It can be written as [143]

$$\hat{\mathrm{G}}(\omega) = \frac{1}{\hbar\omega - \mathrm{H_{BSE}} - \Sigma(\hbar\omega)}$$

where $\hbar\omega$ is the energy of the X-ray photon, $\Sigma(\hbar\omega)$ accounts for the self energy and lifetime effects of the electron and core hole, and $\mathrm{H_{BSE}}$ is the Bethe-Salpeter Hamiltonian (BSH), given by the sum of the hole term $\mathrm{H_h}$, the electron term $\mathrm{H_e}$ and the electron-hole interaction $\mathrm{H_{eh}}$.

The terms describing the hole and the electron are diagonal in the basis used. The

2. The general expression of a Lorentzian function is

$$\mathrm{L}(\omega) = \frac{1}{\pi}\frac{\gamma}{[\hbar\omega - (\mathrm{E_f} - \mathrm{E_i})]^2 + \gamma^2},$$

where

$$\pi\mathrm{L}(\omega) = -\mathrm{Im}\Big(\frac{\omega - \mathrm{i}\gamma}{\omega^2 + \gamma^2}\Big) = -\mathrm{Im}\Big(\frac{1}{\omega + \mathrm{i}\gamma}\frac{\omega - \mathrm{i}\gamma}{\omega - \mathrm{i}\gamma}\Big) = -\mathrm{Im}\Big(\frac{1}{\omega + \mathrm{i}\gamma}\Big)$$

if for simplicity we refer to $\hbar\omega - (\mathrm{E_f} - \mathrm{E_i})$ as ω.

H_h, with a Hartree Fock method, gives core-level eigenvalues E_h and eigenstates Ψ_h of single atoms and that do not change with the environment. This calculation is performed once and the result is the same for all atoms of the same species, independent of local environment.

The H_e term gives the eigenvalues E_e and the eigenstates Ψ_e of conductive states all over the supercell. The calculation is performed for each thermodynamic configuration by means of density functional theory (DFT) with the codes ABINIT or Quantum ESPRESSO.

The calculation that requires the most of the computing power is the one that involves the electron-hole interaction. The H_{eh} is not diagonal and it can be written as the sum of a Coulomb interaction (called the direct term), corrected by the screening of the other electrons, and an exchange term. The exchange term is important only around the absorber, while the direct term has to be calculated all over the supercell. The eigenvalues and eigenvectors have to be calculated for each supercell, and for each atom in the supercell considering every time a different site for the core-hole. As with the radial distribution function, periodic boundary conditions are applied to the atomic supercell.

In this work the XANES spectra have been calculated from the atomic supercells as follows. 11 out of the 100 or 1000 thermodynamic configurations have been chosen in order to sample the evolution of the system every 9 or 90 steps. For each thermodynamic configuration the XANES is obtained by averaging the absorption spectra calculated for every atom in the supercell with three orthogonal polarizations. At a given pressure and temperature condition the spectrum is then the average of the XANES obtained from each sampled supercell. Simulating an absorption spectrum takes a couple of days.

This was done in collaboration with the theoretician K. Gilmore [3]

4.2.4 Density of states

The calculation of the density of states is performed with density functional theory as well. The total electron density obtained by ABINIT or Quantum ESPRESSO is used to calculate the effective particle eigenvalues and eigenstates all over the supercell that allows to construct the density of states (DOS). For each site, the eigenstates are projected onto atomic orbitals to give the projected density of states for that site (PDOS).

The PDOS is calculated in the final-state picture, with a core-hole on the absorbing site. For this reason a separate calculation is required for each atom in the su-

3. Keith Gilmore, Theory Group at the ESRF in Grenoble, France

percell. To limit computational expense, the calculation was performed on 10 atomic sites randomly chosen among the sites in the supercell. The same is repeated for 11 thermodynamic configurations and the results are averaged. Simulating the density of states takes a couple of weeks.

This work was done in collaboration with the theoretician K. Gilmore [3].

4.3 Atomic supercell size

The calculations of the X-ray absorption near edge structure and the density of state require non-negligible computing power. For this reason finding the smallest atomic supercell that still describes the system under analysis is required. At first, several atomic supercells with different sizes were tested.

In Figure 4.1 are represented in a phase diagram the different pressure temperature conditions of the generated atomic supercells with their sizes in terms of number of atoms. In the insets the radial distribution functions of the atomic supercells are compared. In the one in the left structures from atomic supercells with 128 and 54 atoms and 32 atoms are compared. The g(r) calculated from the smaller atomic supercell are slightly more noisy, but the position and the shape of the peaks is the same as the one with more atoms. The same result is obtained for the first peak of the liquid with 128, 54 or 32 atoms, as shown in the right inset. The inset in the centre shows the comparison between the radial distribution function of solid fcc and the liquid. In these examples the g(r) is calculated as the average of all the thermodynamic configurations available (between 100 and 1000).

As a result of these preliminary tests, several atomic supercells were generated at different pressure temperature conditions in the solid and liquid phase with 32 atoms and 1000 thermodynamic configurations.

4.4 Validation of the melting criterion

Several XANES spectra have been calculated at most of the pressure temperature conditions shown with symbols in Figure 4.1. Spectra are thus calculated for the three phases: solid fcc, solid hcp and liquid.

The main result obtained is the theoretical validation of the melting criterion proposed in Section 3.2. XANES spectra calculated for the fcc solid and the liquid are compared at different pressures. The results are shown in Figure 4.2 for $\sim$25 GPa, $\sim$45 GPa and $\sim$65 GPa. Even if the pressure is different the change of phase between

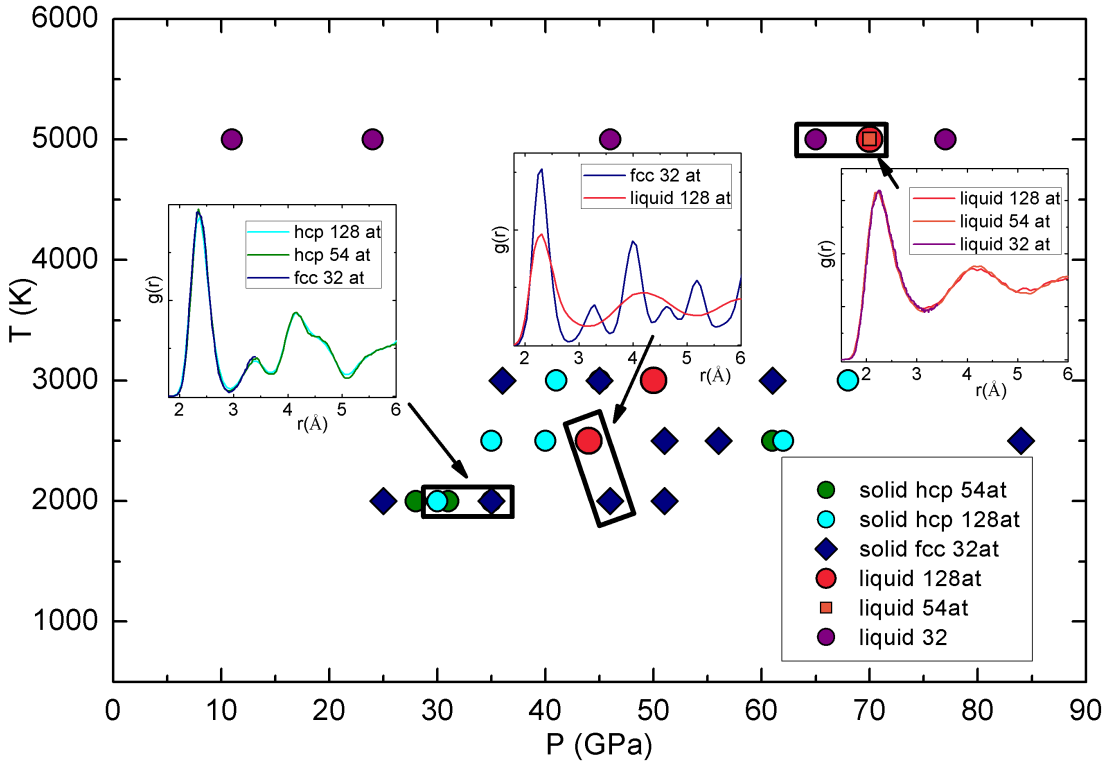

Figure 4.1 – Pressure temperature conditions of the atomic supercells calculated with different sizes. Radial distribution functions are calculated for different configurations in order to find the atomic supercell with the smaller amount of atoms that still contains the correct structural information.

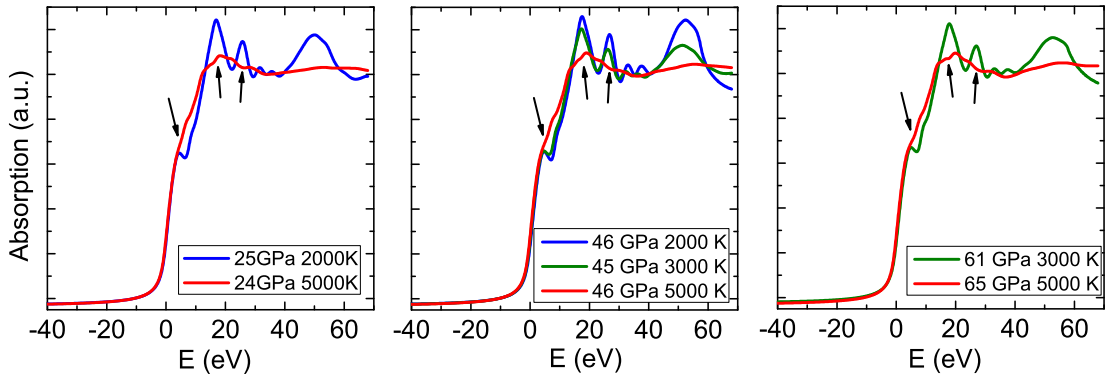

Figure 4.2 – Solid and liquid spectra at different pressures.

the solid fcc and the liquid can be detected always in the same way: the shoulder disappears and the first two oscillations flatten. The criterion used in this work to detect the melting from an fcc solid phase to the liquid phase is thus validated not only for nickel with *ex-situ* analysis on the recovered samples, but for cobalt as well, with the support of theoretical calculations.

Moreover, these theoretical calculations allow to investigate the electronic and structural modifications that influence the detected changes in the XANES. The electronic and atomic structure are deeply interconnected, but their effect is probed with theoretical calculations in two different ways, that are thus here presented separately.

4.4.1 Atomic structure: contribution of the environment

The atomic structure of a liquid is very different from that of a solid. More details about this will be given in Chapter 5, but to understand the following it is sufficient to know that in the transition from solid to liquid the long range order typical of a crystalline solid is lost, in favour of a dense quasi-random packing of atoms.

In a crystalline solid each atom sees the same coordination shell. The crystalline order is disrupted only by thermal disorder. An example of atomic supercell representing a thermodynamic configuration for the solid fcc at 45 GPa and 3000 K is shown in the left panel of Figure 4.3(a). In the right panel are plotted the XANES spectra calculated imposing each time a different atom as photoabsorber. The XANES in magenta in the right panel is calculated imposing as photoabsorber the atom that in the atomic supercell shown in the left panel is indicated with the colour magenta. Periodic boundary conditions are applied to the atomic supercell and each atom is surrounded by the same crystalline structure. The XANES spectra calculated for the different atoms of the supercell thus exhibit the same features. Averaging over all the

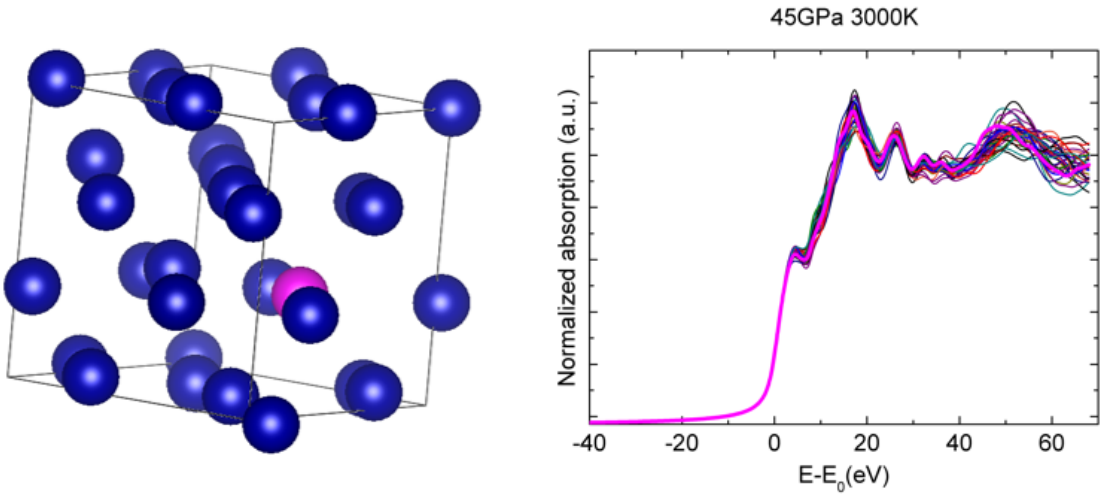

(a) Solid fcc atomic supercell representation and XANES at 45 GPa and 3000 K. Atoms are displaced from crystallographic fcc sites due to thermal vibrations.

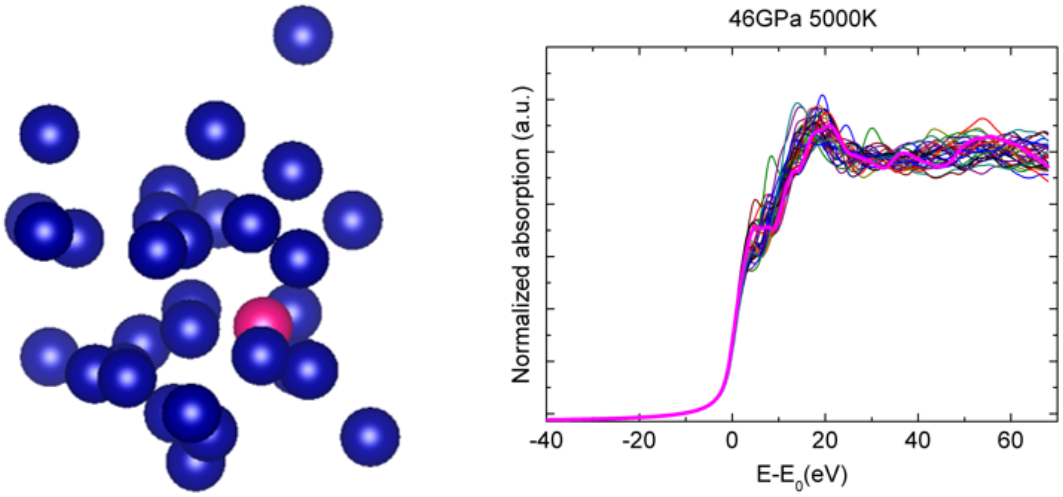

(b) Liquid atomic supercell representation and XANES at 46 GPa and 5000 K. Atoms are displaced not only due to thermal disorder, but due to dynamical disorder as well.

Figure 4.3 – Solid and liquid configurations. Both for the solid and the liquid configuration, the XANES spectra are calculated for each of the atoms of the atomic supercell representations shown in the left. The spectrum in pink is the one associated to the atom illustrated in pink in the atomic supercell representation.

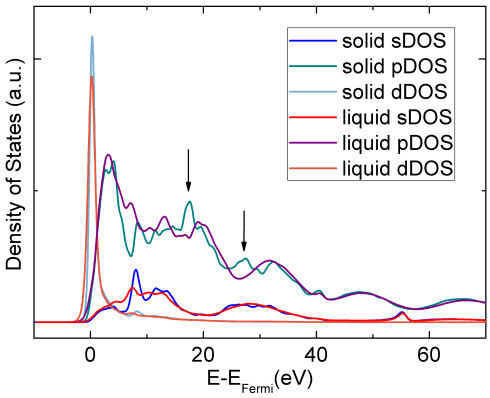

(a) Density of states of cobalt at about 45 GPa for the solid fcc and the liquid phase.

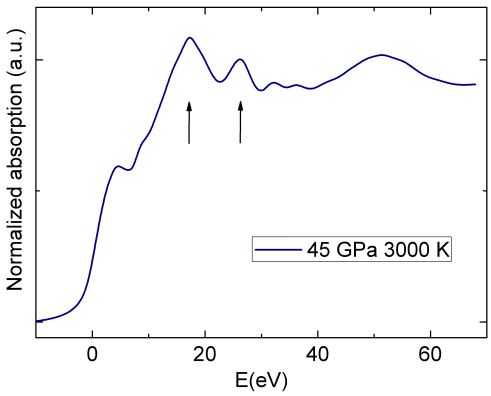

(b) Calculated XANES spectrum of fcc cobalt at 45 GPa and 3000 K.

Figure 4.4 – Density of states of solid and liquid cobalt. The arrows point at the features which change between the solid and the liquid in the DOS and in the XAS.

atoms and 11 configurations will give as a result a XANES spectrum showing these same features.

In a liquid, instead, due to the quasi-random displacement of atoms, each atom is surrounded by different atomic structures. In this case, there are two factors disrupting the periodic order: the thermal disorder, as in the hot solid, and the dynamical disorder. An atomic supercell representing a liquid at 46 GPa and 5000 K in one thermodynamic configuration is shown in the left panel of Figure 4.3(b). In the same way as for the solid, the XANES imposing each different atom as a photoabsorber are plotted in the right panel. However, in this case each atom is surrounded by a different structure. As a consequence the leading frequencies are different for each photoabsorber and each XANES shows different features. The average over these XANES and over 11 configurations gives a XANES which is almost featureless. For this reason the transition to the liquid phase can be identified with the loss of those oscillations that are typical of the fcc XANES.

4.4.2 Electronic structure: DOS simulations

The density of states have been calculated for the two configurations shown in Figure 4.3. The results are shown in Figure 4.4(a) and the changes occurring to the PDOS of the *s*, *p* and *d* atomic orbitals are due to the phase transition.

The atomic orbitals responsible for the flattening of the first two oscillations in the XANES are the *p* orbitals. In Figure 4.4(a) the two peaks responsible for the first two oscillations in the XANES, Figure 4.4(b), are highlighted with black arrows. These

two peaks disappear in the PDOS of the liquid, meaning that the flattening of the first two oscillations can also be explained by the change of the DOS.

In conclusion the first two oscillations in the XANES are more influenced by the *p* states, while the shoulder is more influenced by the *d* states (probably hybridized with the *p* states).

4.5 Discussion

The main purpose of these theoretical calculations was to validate the melting criterion used in this thesis. However they also allowed to formulate other observations that deserve to be mentioned.

4.5.1 Changes with pressure

Observing the differences in the XANES occurring in the solid and in the liquid upon increasing pressure can also give some insights on the behaviour of the system at high temperature at increasingly higher pressure.

Calculations

In Figure 4.5(a) and 4.5(b) are represented XANES spectra calculated for several fcc solids and liquids respectively. As a general remark we observe that the oscillations after the whiteline are shifting to the right as pressure increases. It is interesting to notice that the shift starts at about 4 eV from the E_0 for both solids and liquids structures.

Experiment

In Figure 4.5(c) and 4.5(d) are represented the experimental XANES measured at similar temperatures. In Figure 4.5(c) is shown the trend at increasing pressure of the XANES at about 2000-2300 K. In the solid, Figure 4.5(c), the first half of the whiteline does not change with pressure, while the second half shifts to the right. The shoulder becomes more evident at increasing pressure, while in the first two oscillations we notice a gradual transition between a mixed hcp-fcc phase to a situation where the fcc structure dominates. In the liquid as well, Figure 4.5(d), there are no differences with pressure in the first half of the whiteline while the second half shifts to the right.

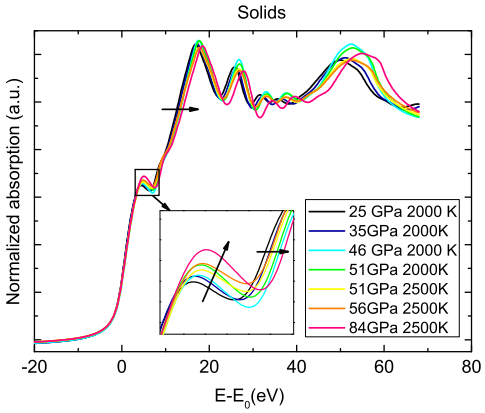

(a) Calculated XANES spectra of fcc solids at 2000-2500 K at increasing pressure.

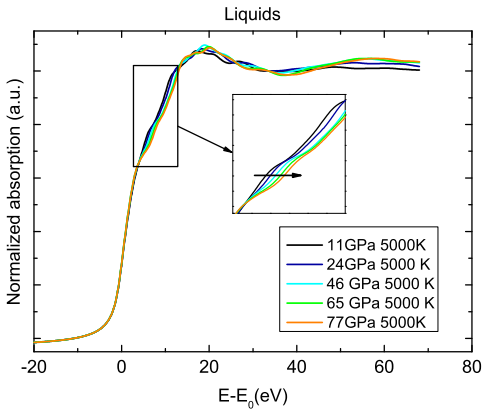

(b) Calculated XANES spectra of liquids at 5000 K at increasing pressure.

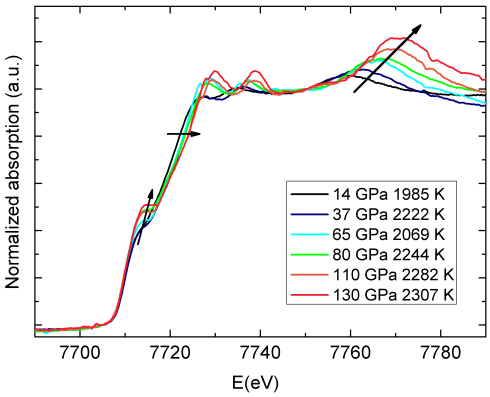

(c) Measured XANES spectra of solids at 2000-2500 K at increasing pressure. Between 37 and 65 GPa there is a transition from a mixed hcp-fcc phase to a situation where fcc dominates.

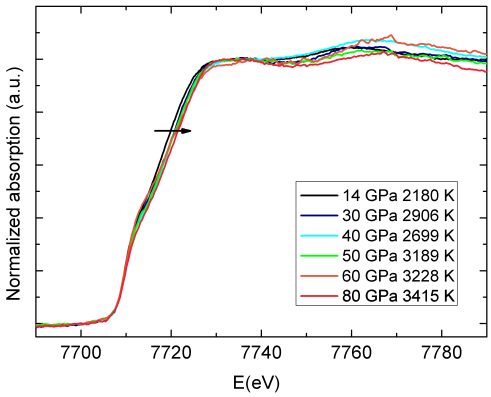

(d) Measured XANES spectra of liquids along the melting line at increasing pressure.

Figure 4.5 – The first half of the whiteline does not change with pressure, while the second half shows a shift to the right for both the solid and the liquid.

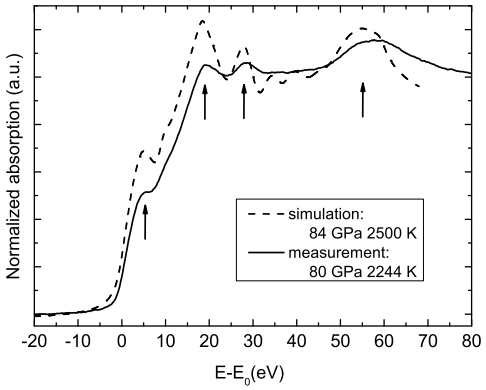

Figure 4.6 – Direct comparison between measured and simulated spectra at similar pressure-temperature conditions.

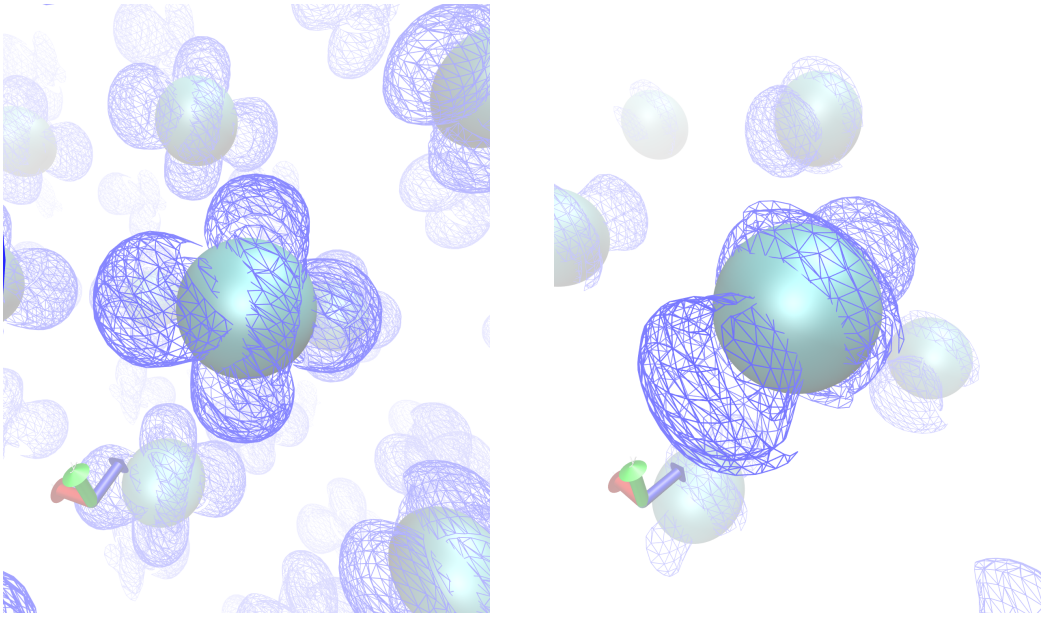

(a) E_{Fermi} (b) E_{Fermi}+4 eV

Figure 4.7 – Graphical representation of the Bloch functions in the 3D space. In the reference system the red arrow represents the *x*, the green the *y* and the blue the *z* direction.

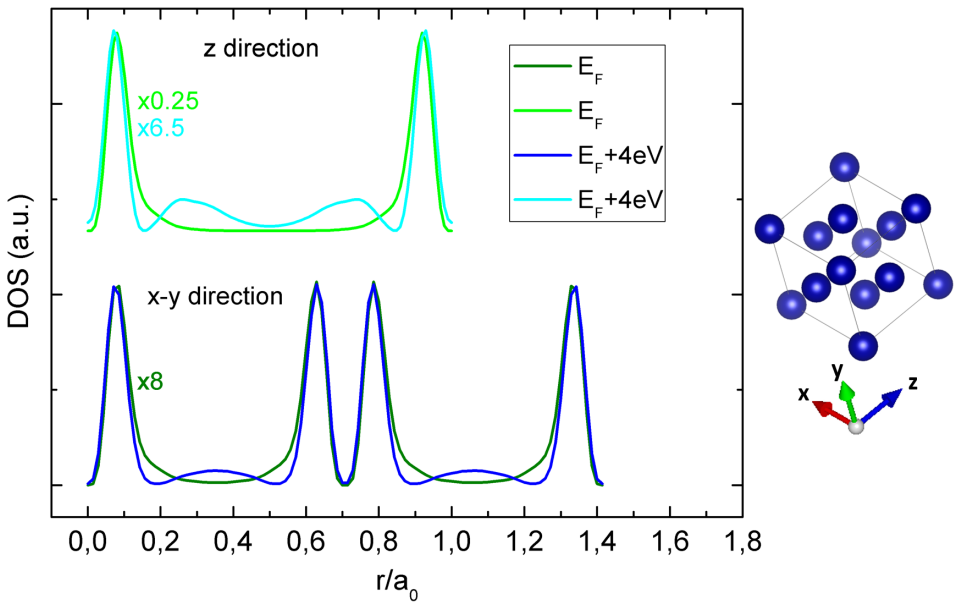

Figure 4.8 – Spatial distribution of the atomic orbitals for an fcc structure in its ground state.

The qualitative agreement between the results obtained with the calculations and the measurements is good. A direct comparison of measured and simulated spectra at similar pressure-temperature conditions, Figure 4.6, shows that the features are the same: a shoulder at about 5 eV, first two oscillations at about 19 eV and 28 eV and a third oscillation at about 55-60 eV. The energy scale is not perfectly reproduced in the calculations, as can be noticed in the position of the third oscillation, that in the calculation appears at lower energies than in the measurement. Another difference between the two spectra is given by the resolution, which is much higher in the calculations, showing sharper oscillations.

Going back to the comparison between changes at different pressures for solid and liquid, shown in Figure 4.5 we notice that overall the changes consist in a shift to the right of the oscillations, in agreement with a general compression of the system. The first and the second half of the whiteline, though, seem to be affected differently by the variation of pressure. Our interpretation for this is provided here. Figure 4.7(a) shows isosurfaces of the square modulus of selected Bloch wavefunctions. Figure 4.7(a) presents the wavefunction of a Bloch state at the Fermi energy at the Γ point in the Brillouin zone. The spatial distribution of this Bloch function resembles the shape of a *d* orbital. We can thus affirm that at the Fermi energy the orbitals have mainly a *d* character. Figure 4.7(b) gives a Bloch state at an energy about 4 eV higher

than the Fermi energy. In this case, the orbitals have mainly a *p* character, with some d_{z^2}.

Figure 4.8 shows a 1D cut of the same wavefunction probability distributions along the edge and the face diagonal direction for the two energies. The probability densities are re-scaled for better clarity. The results show that in both directions the orbitals with mainly *d* character are more localized around the atomic positions, while the orbitals with some *p* character exhibit some intensity in the interstitial region.

In conclusion, the *p* orbitals have a larger extension in space and are therefore more sensitive to the changes in the structure driven by the increase of pressure. The *d* orbitals are instead more localized around the atoms and less affected. This could explain why the region of the XANES associated with final states with greater *p* character changes more with pressure than features originating from final states with more *d* character.

4.5.2 Changes with temperature

Calculated and experimental spectra can also be compared as a function of temperature. An example is shown in Figure 4.9, where calculations and experiments are compared.

In Figure 4.9(a) are shown two calculated spectra of solid cobalt at about 45 GPa and a temperature of 2000 K and 3000 K. In Figure 4.9(b) instead is shown an experimental run in temperature at 80 GPa. In the represented spectra the temperature spans from 1850 K and 3600 K, with the exception of the spectrum represented in black which is at ambient temperature. In both the calculated and measured XANES it is clear that: the shoulder becomes less pronounced at increasing temperature, the second half of the whiteline shifts to the left (contrary to the effect of the increase of pressure), the first two oscillations damp. In the measured spectra in Figure 4.9(b) the damping is even more evident in the EXAFS.

Liquid spectra can be compared as well as a function of temperature. In Figure 4.9(c) are shown three measured liquids 40 GPa. The damping of the first oscillations is highlighted in the inset of Figure 4.9(c), while the small difference in temperature does not allow to notice if there are relevant changes in the whiteline.

4.5.3 Polarization

The difference between the hcp and the fcc solid structure is visible not only in the radial distribution function, as shown in Figure 4.1, but in the XANES spectra as well. An example of XANES of hcp cobalt at 33 GPa is plotted with a black solid line

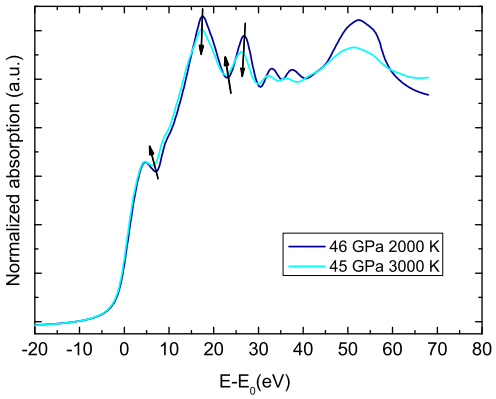

(a) Calculated XANES spectra of solids at 45 GPa at increasing temperature: 2000 K and 3000 K.

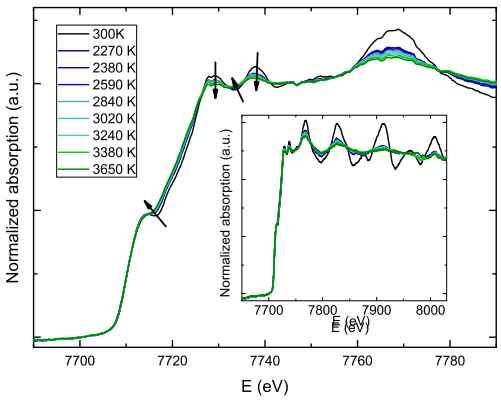

(b) Measured XAS spectra of solids at 80 GPa and increasing temperature. The black spectrum is measured at ambient temperature, the temperatures of the others vary from 2270 K to 3650 K. In the inset the XAS is highlighted for comparison with the calculations.

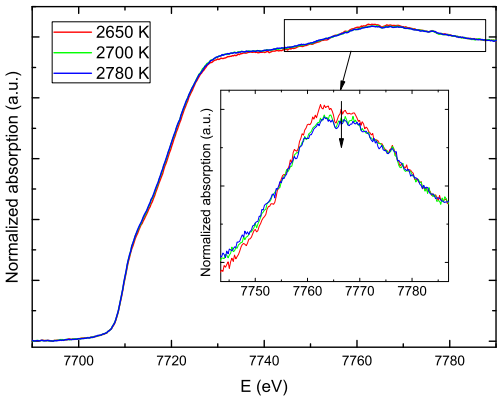

(c) Measured XANES spectra of liquids at 40 GPa and increasing temperature, from 2650 K to 2780 K. In the inset is highlighted the damping of one of the oscillations due to the increase of temperature.

Figure 4.9 – The first half of the whiteline does not change with temperature, while in the second half the there is a gradual shift to the left. The shoulder becomes less and less visible when the temperature is increased.

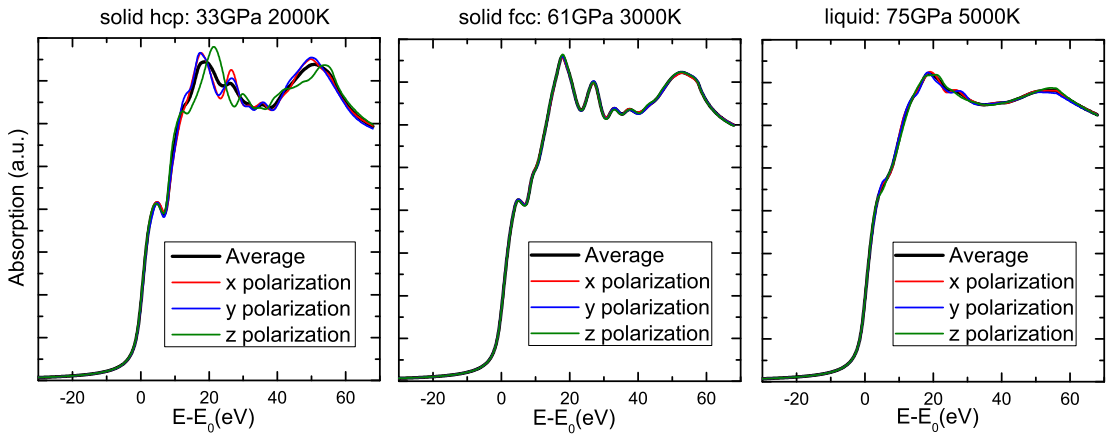

Figure 4.10 – The polarization for the three axes is shown for the simulated XANES of the two solids (hcp and fcc) and the liquid configuration.

in the left panel of Figure 4.10. A XANES spectrum calculated for fcc cobalt at 61 GPa and 3000 K is instead shown with a black solid curve in the middle panel of the same Figure. Finally, the XANES of liquid cobalt at 75 GPa and 5000 K is shown in the right panel.

In Figure 4.10 the contribution to the XANES of the three polarization directions is highlighted for the two solids and the liquid configuration. In the fcc solid and in the liquid the three polarization directions give the same XANES. Instead, in the hcp solid the XANES calculated in the polarization direction 1 and 2 is different to the one calculated in the polarization direction 3, as shown in the left panel of Figure 4.10. This is not surprising, as that the three directions are equivalent for fcc solid and liquid. In the case of the hcp solid, as expected, the structure probed along one of the three axes is different from the other two.

4.6 Conclusions

To conclude, *ab-initio* calculations provide an excellent tool that allows not only to understand the experimental data, but to have some insight on the physical phenomena taking place at the atomic scale.

In this work the AIMD calculations coupled with simulations of the XANES spectra allowed to validate the XAS melting criterion used in this work. Moreover, the calculations allowed to highlight that the observed changes in the data upon melting can be interpreted in terms of modification of the structure of electronic states, two views of the same physical phenomenon.

Chapter 5

Local structure of liquid nickel and cobalt under pressure

In this chapter the structure of a liquid is discussed, with particular attention to the structure of liquid nickel at ambient pressure that was subject of several theoretical and experimental studies. Calculations showing the compression of nickel and cobalt follow. The methods used for the EXAFS analysis of liquids are presented, with particular attention to the approach used on the data collected in this work. Finally the results are compared with the literature and discussed.

5.1 Structure of a liquid

The structure of a liquid or an amorphous solid is quite complex, far from the periodicity of a solid crystal but still not purely random. The first theories to describe the structure of a liquid were formulated in the mid-twentieth century. In the theory proposed by Born and Green in 1946 it was considered as an imperfect gas. The mathematical description associated was too complex to be handled computationally and the theory was soon discarded. According to Kirkwood and his followers (1939 to 1950) instead a liquid had to be considered as an imperfect solid. Even if this model was accurately describing the variation of density in the phase transition, it failed in understanding properties of entropy and pressure. A third model was then formulated, associated with the name of Eyring (1958), in which the liquid was treated as a mixture of submicroscopic crystals. The crystals themselves are ordered but they are disposed in a disordered fashion ([18] and references therein). This third model embodies the principal characteristic of liquids that is the lack of long range order but the presence of short range order [95].

In solids the radial distribution function g(r), representing the probability of finding another atom at a distance r from the origin atom at $\mathrm{r} = 0$, can be described as the sum of independent isolated shells (each with its specific position, width, intensity and asymmetry). In liquids instead it is characterized by a continuous distribution of distances. In an homogeneous monoatomic system with macroscopic density ρ, the number of atoms dN that can be found in a shell of width dr at a distance r from the absorber atom can be written as

$$\mathrm{dN} = 4\pi \mathrm{r}^2 \rho \mathrm{g}(\mathrm{r}) \mathrm{dr} \tag{5.1}$$

where the radial distribution function g(r) has three distinctive properties:

- $\mathrm{g}(\mathrm{r}) = 0$ for $\mathrm{r} < \sigma$: the probability of finding an atom too close to the absorber is zero below a certain approach distance σ that corresponds to the repulsive part of the interaction potential. σ is as well the hard sphere diameter.
- $\lim_{\mathrm{r}\to\infty} \mathrm{g}(\mathrm{r}) = 1$: at long distances the number density equals the macroscopic density $\mathrm{dN}/(4\pi \mathrm{r}^2 \mathrm{dr}) = \rho$
- $\mathrm{g}(\mathrm{r}) > 0$ for $\mathrm{r} > \sigma$: due to the continuous distribution of distances the radial distribution function is always strictly positive after the approach distance σ

Even if from the radial distribution function it is not possible to define univocally the actual disposition of atoms in 3D space, it is possible to check if a structural model is in agreement with a specific radial distribution function [18]. The g(r) depends only on the distance from a given atom, different configurations of atoms would in fact lead to the same radial distribution function. An equivalent way commonly used to describe the local structure of a liquid is the structure factor S(Q), which is the Fourier transform of the radial distribution function.

The most common model used in the literature to describe a local arrangement of atoms in a liquid is based on a dense random packing of hard-spherelike atoms [164, 18]. The structure is mainly determined by the form of the repulsive part of the pair potential at short distances. Atoms in fact cannot approach closer than the sum of their atomic radii. Actually since in liquid metals the bare atoms are only partially screened by the electron gas, the effective interaction distance (or hard sphere diameter) is larger than the diameter of bare ions [164]. In this model the liquid is treated as a heap of atoms, the interactions between the atoms (that govern chemical short range order, CSRO [119]) are to a first approximation ignored and the local structure is described only by statistical geometry [18] (that govern topological short range order (TSRO) [119]). This model was adopted in several works devoted to the study of

the local structure of liquid metals, both theoretical [18, 71, 58] [1] and experimental [164, 141].

The hard sphere model is sometimes considered too simplistic to describe the atomic interactions in metallic liquids, but a complete theoretical understanding of the structures of liquid metals seems to be still missing [95]. Liquid structures obtained with molecular dynamics using different and more complicated pair potentials sometimes agree with the experimental results for late transition metals but fail for the early ones [95]. The promising point is that regardless the model adopted, the most common tile found in the liquid structures is the icosahedral cluster.

The presence of icosahedral structures in liquids was proposed for the first time in 1952 by Frank [64]. According to his study the presence of icosahedral short range order (ISRO) would hamper nucleation during the cooling of the liquid, and this would explain the undercooling properties studied by Turnbull two years before [160]. Since then many theoretical [58, 76, 77, 49, 103] and experimental [140, 95, 41] studies have been performed to verify Frank's hypothesis, many of them on nickel and mainly with the aim of understanding the solidification process. Molecular dynamics, diffraction and absorption all confirm the presence of icosahedral short range order in the liquid metals at ambient pressure.

The common-neighbour analysis (CNA) has been performed both by ab-initio molecular dynamics (AIMD) [103] and by a combination of X-ray absorption spectroscopy, reverse Monte Carlo and molecular dynamics [41]. The result of the AIMD study performed by Ma et al. [103] is that the most common configuration is the one with Honeycutt-Andersen indexes 1551, shown in Figure 5.1(a), which is the necessary unit for the icosahedron. The other two most common structures are faulty units shown in Figure 5.1(b) and 5.1(c). In this study the Voronoi's tesselation method was employed as well. It was found that the cluster formed only by 1551 pairs, the regular icosahedron (ICOS) shown in Figure 5.1(d), is the one with the longest average lifetime but is not the most abundant. The most abundant one is instead a distorted icosahedron (DICOS), shown in Figure 5.1(e). The presence of fcc type clusters is excluded. The result of CNA shown in the study performed by Di Cicco et al. [41] reaches as well the conclusion that highly distorted or defective icosahedra are the most frequent configurations. Unlike the previous study some structures reminiscent of the fcc crystalline structure are found, that are slightly more abundant than the perfect icosahedral structures.

1. The study by Bernal is considered as theoretical because it does not involve measurement on liquid metals. In his study he performed a statistical analysis of the distribution of balls, that model hard spheres.

(a) 1551 (b) 1541 (c) 1431 (d) ICOS (e) DICOS

Figure 5.1 – The first three images represent the most common nearest neighbours pairs in nickel [103]. In the captions are reported the Honeycutt-Andersen indexed. The last two images are a regular icosahedral cluster (ICOS) and a distorted one (DICOS) [103].

Experimental studies of the behaviour of liquids under pressure are more challenging. To our knowledge the only ones performed on 3d metals are limited to iron up to 5 GPa [137] and up to 58 GPa [141]. In the first study a change in the structure of the liquid was detected in the vicinity of the δ-γ-liquid triple point upon increase of temperature and pressure [137]. The other study [141] was focused on higher pressures and no significant changes in the structure were detected. Iron resulted to be well described by the hard-sphere model. However the authors did not perform a detailed analysis on the g(r).

Liquid-liquid phase transitions normally appear in correspondence of a solid-solid phase transition below the melting curve or in case of changes in slope of the melting curve, as in the cases of sodium and bismuth [70, 167]. However it was recently found that liquid-liquid transitions can as well appear in a metal with a positive slope of the melting curve and in the absence of solid-solid phase transitions just below the melting curve [94]. The presence of the strong bond directionality that occurs in early transition metals such as titanium, could lead to Jahn-Teller effects that can cause a liquid-liquid structural transition. According to Lee et al. [94] in late transition metals the bond directionality is negligible, thus preventing liquid-liquid transitions.

Nickel and cobalt are late transition metals and they exhibit a smooth melting curve, for these reasons we do not expect liquid-liquid transitions upon increase of pressure. The liquid structure of iron, their neighbour in the periodic table, was recently measured along the melting curve in X-ray diffraction [141], and no phase transition was observed. Moreover, due to the directional nature of the unfilled d orbitals, we can expect deviations from the behaviour of a hard sphere like liquid.

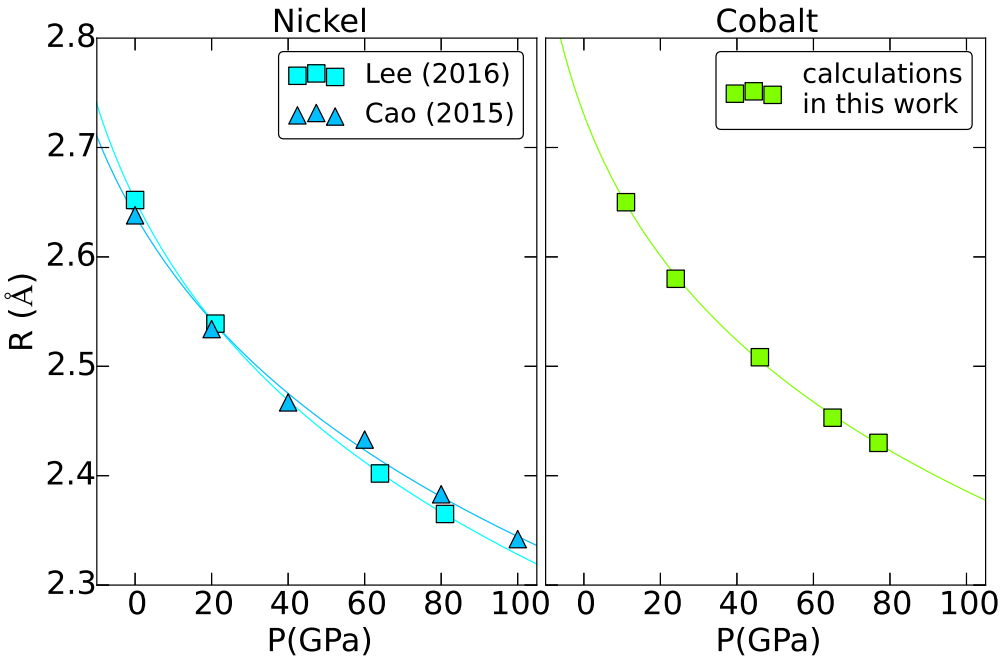

Figure 5.2 – Compression of the first neighbour distance R in nickel calculated with MD in Cao et al. [32] and AIMD in Lee et al. [94]. Cao's points are calculated along the melting curve, Lee's points along the isotherm at 3000 K. The points were fitted with a Vinet equation of state that serves mainly as guide for the eyes. *Right panel*: compression of the first neighbour distance in cobalt calculated in this work with AIMD. These points in the pressure-temperature phase diagram were calculated along an isotherm at 5000 K.

5.2 Calculated compression of liquid nickel and cobalt

The compression of liquid nickel was recently calculated by Cao et al. in 2015 [32] and by Lee et al. in 2016 [94]. The literature about compression of liquid cobalt is instead quite scarce. The volume as a function of pressure was calculated by Zhang et al. in 2014 [174] by means of MD simulations performed with a Zhou's EAM potential. Since the radial distribution functions were not provided, the results of this paper will be compared with ours only in paragraph 5.6.

Liyuan et al. performed in 2011 first-principle calculations with aim to study the microstructure of liquid cobalt under pressure, up to 110 GPa. Their result shows that the short range order increases with pressure, i.e. the number of icosahedra and distorted icosahedra increases with pressure and temperature [99].

Nickel

Cao et al. performed simulations along the melting curve, shown in Figure 3.1, by means of molecular dynamics. Lee et al. instead simulated the structures along the isotherm at 3000 K with ab-initio molecular dynamics. The resulting radial distribution functions at different pressure-temperature conditions are provided up to 7 and 8 Å respectively. A fit of the calculated radial distribution functions was performed with a gamma distribution model [34, 53, 55] in order to extract the compression of the first neighbours as a function of pressure. The bond length probability in its general formulation, for $(\mathrm{R}-\mathrm{r})\beta < 2\sigma$, is

$$\mathrm{p(r)} = \frac{2}{\sigma|\beta|\Gamma(\frac{4}{\beta^2})}\Big(\frac{4}{\beta^2} + \frac{2(\mathrm{r}-\mathrm{R})}{\sigma\beta}\Big)^{\frac{4}{\beta^2}-1} \times \exp\Big[-\Big(\frac{4}{\beta^2} + \frac{2(\mathrm{r}-\mathrm{R})}{\sigma\beta}\Big)\Big], \tag{5.2}$$

where $\Gamma(\mathrm{z})$ is Euler's gamma function [2] calculated for $\mathrm{z} = \frac{4}{\beta^2}$ defined on the positive real axis, R is the average distance, σ^2 is the variance and β the skewness parameter that defines the asymmetry of the distribution. The Gaussian limit is obtained for $\beta = 0$. The fit was performed using the package *grfit* of the program GnXAS [56]. Note that the probability density $\mathrm{p(r)}$ of finding a bond with length r is related to the g(r) through the expression $\mathrm{Np(r)} = 4\pi\rho\mathrm{r}^2\mathrm{g(r)}$; the density ρ has to be known and the result of the fit will give the parameters N, R, σ^2 and β [54].

The resulting trends are represented in the left panel of Figure 5.2. The points are fitted with a Vinet equation of state, that is normally used for solids but that serves here as a guide for the eyes. Its formulation is presented in Appendix B.0.2. In the case of Lee's data [94] the densities were provided by the author [3]. The coordination number can be calculated as

$$\mathrm{N_C} = 4\pi\rho\int_0^{\mathrm{r_{min}}} \mathrm{g(r)r^2dr}, \tag{5.3}$$

where $\mathrm{r_{min}}$ is the first minimum of the g(r). The densities, the values of the integrals at the different pressures, the calculated coordination numbers and the fit results are displayed in Table 5.1. We note that:

1. The ambient pressure value of $\mathrm{N_C}$ is > 12.
2. $\mathrm{N_C}$ is practically constant throughout the full pressure range 0-80 GPa: $\frac{\Delta \mathrm{N}}{\mathrm{N}} < 0.005$.
3. the mean square relative displacement σ^2, reflecting the disorder, decreases

2. $\Gamma(\mathrm{z}) = \int_0^\infty \mathrm{x^{z-1}e^{-x}dx}$

3. Geun Woo Lee, Korea Research Institute of Standards and Science, Daejon 34114, Republic of Korea

very strongly. Since calculations are at constant T, this reduction reflects the stiffening of the bonds (increase in force constants) due to compression.

4. β decreases, meaning that the distribution becomes more symmetric with pressure.

In the case of Cao's data, shown in Table 5.2, the coordination number is provided, the density is thus calculated inverting the Equation 5.3. We note that:

1. The ambient pressure value of N_C is > 12.
2. N_C decreases in the pressure range 0-100 GPa: $\frac{\Delta N}{N} \sim 0.05$.
3. σ^2 decreases along the melting curve, indicating that the stiffening of the bonds due to compression is larger than thermal effects, which increase the vibration amplitude. The total decrease is ∼25%.
4. β stays approximately constant, meaning that the temperature and pressure effect compensate.

The absolute value of the g(r) first peak's position calculated by Cao or Lee differs by 0.014 Å. The curve by Cao shows less compression, and this is reasonable since in these calculations points at higher pressure are also at higher temperature.

Cobalt

The compression of liquid cobalt was calculated exploiting the radial distribution functions extracted from the atomic supercell generated with ab initio molecular dynamics, see Section 4.2. About 1000 thermodynamical samples of supercells containing 32 atoms were used; the g(r) here were calculated with the program Travis [27]. The radial distribution functions were fitted with a gamma distribution model in order to extract the compression along the isotherm at 5000 K. In this case the density was calculated as the number of atoms in an atomic supercell divided by the size of the supercell. The compression, shown in the right panel of Figure 5.2, is comparable with the one found by Lee in nickel (∼0.4 Å over 100 GPa). Table 5.3 lists parameters derived from the fit of the g(r). We note that:

1. The ambient pressure value of N_C is > 12.
2. The N_C increases with pressure in the pressure range 11-77 GPa: $\frac{\Delta N}{N} \sim 0.08$. This is in contrast with the case of nickel.
3. The σ^2 follows the same trend of those obtained form the calculations of Lee for nickel, although the values are larger due to the different temperature. The total decrease is 40%.

Nickel at 3000 K, calculated by Lee et al.:

P (GPa)	ρ(at/Å^3)	N_C	N	R(Å)	σ^2(Å^2)	β
0	0.07924	13.36	11.1	2.652	0.148	0.987
21	0.09111	13.31	11.5	2.539	0.102	0.886
64	0.10547	13.41	11.4	2.402	0.066	0.815
81	0.10952	13.42	11.1	2.365	0.054	0.735

Table 5.1 – Density and coordination numbers of the g(r) calculated by Lee as a function of pressure [94]. The densities ρ were provided by the author; they are used to calculate the N_C and imposed in the fit. The N_C where provided in the paper, the densities were calculated exploiting the Equation 5.3. The fitting parameters (N, R, σ^2 and β) follow.

Nickel along the melting curve, calculated by Cao et al.:

P (GPa) - T (K)	ρ(at/Å^3)	N_C	N	R(Å)	σ^2(Å^2)	β
0 - 1400	0.08461	14.65	10.7	2.638	0.077	0.750
20 - 2100	0.09450	14.32	10.9	2.534	0.074	0.778
40 - 2700	0.10060	14.28	11.0	2.467	0.071	0.791
60 - 3250	0.10820	14.22	11.4	2.433	0.073	0.819
80 - 3770	0.11182	13.99	11.1	2.383	0.063	0.750
100 - 4300	0.11196	13.93	10.9	2.342	0.058	0.729

Table 5.2 – Density ρ and coordination numbers N_C of the g(r) calculated by Cao as a function of pressure [32]. The N_C where provided in the paper, the densities were calculated exploiting the Equation 5.3. The fitting parameters (N, R, σ^2 and β) follow.

Cobalt at 5000 K, calculated in this work:

P (GPa)	ρ(at/Å^3)	N_C	N	R(Å)	σ^2(Å^2)	β
11	0.07585	12.28	10.06	2.65	0.19	0.87
24	0.08397	12.41	10.37	2.58	0.16	0.87
46	0.09329	12.69	10.91	2.51	0.13	0.84
65	0.09956	13.01	10.05	2.45	0.11	0.79
77	0.10267	13.26	10.25	2.44	0.11	0.81

Table 5.3 – Density and coordination numbers of the g(r) calculated as a function of pressure from AIMD. The densities ρ were calculated dividing the number of atoms in the supercell for the volume of the supercell and are then imposed in the fit. Coordination numbers are calculated by means of Equation 5.3. The fitting parameters (N, R, σ^2 and β) follow.

5.3 EXAFS data analysis for disordered systems

Here we present how to perform EXAFS data analysis on liquids, where the configurational disorder is significant and the Gaussian shell model adopted to obtain Equation 2.4 is no longer valid. To extract information about the local structure of a liquid a completely different approach to the one presented as general case in Section 2.1.2 is required.

If γ is the EXAFS signal produced by one atom at a distance r from the absorber, the total EXAFS signal $\chi(\mathrm{k})$ for a liquid, or a disordered system, is given by

$$\chi(\mathrm{k}) = \int_0^\infty 4\pi \mathrm{r}^2 \rho \gamma(\mathrm{k},\mathrm{r}) \mathrm{g}(\mathrm{r}) \mathrm{dr}. \tag{5.4}$$

Due to the integral that relates the total EXAFS signal $\chi(\mathrm{k})$ and the radial distribution function it is not possible to obtain the g(r) directly from Equation 5.4 [17, 165].

A procedure to overcome this problem was proposed by Filipponi [53, 55] together with the realization of a program to perform the analysis: GnXAS [56]. The starting point is a model g(r) describing the liquid system under the pressure and temperature conditions of interest. It can be calculated with molecular dynamics or measured by X-ray diffraction.

At first (step 1 in Figure 5.3) the model g(r) is decomposed in one (or two) short distance peak(s) and a tail. The fit is performed using the package *grfit* that fits the first peak with one (or two) gamma distributions, see Equation 5.2 [34, 53, 55]. The fit gives parameters such as the position R, the width σ^2, the intensity (strictly related to the coordination number N) and the asymmetry β of the gamma distribution.

The EXAFS theoretical signal is calculated starting from R and N using the package *gnxas* (step 2).

The package *fitheo* is then used to fit the calculated EXAFS signal to the experimental one (step 3) including also the parameters σ^2 and β. In this way the structural parameters are refined.

The tail remains unvaried, since it refers to long range order to which EXAFS is not sensitive. The experimental g(r) can finally be reconstructed by means of the package *grrec* (step 4). The reconstructed radial distribution function best describes the system under analysis.

The choice of fitting the radial distribution function with one or two peaks depends on the quality of the data. If the experimental EXAFS signal is short ($\mathrm{k}_{\max} < 8$ $\mathrm{\AA}^{-1}$) and the signal to noise ratio is poor, like in our case, the fit with two model EXAFS signals could be very unstable or lead to unphysical results. Therefore we have adopted the procedure shown in Figure 5.3 using one peak to reproduce the first peak

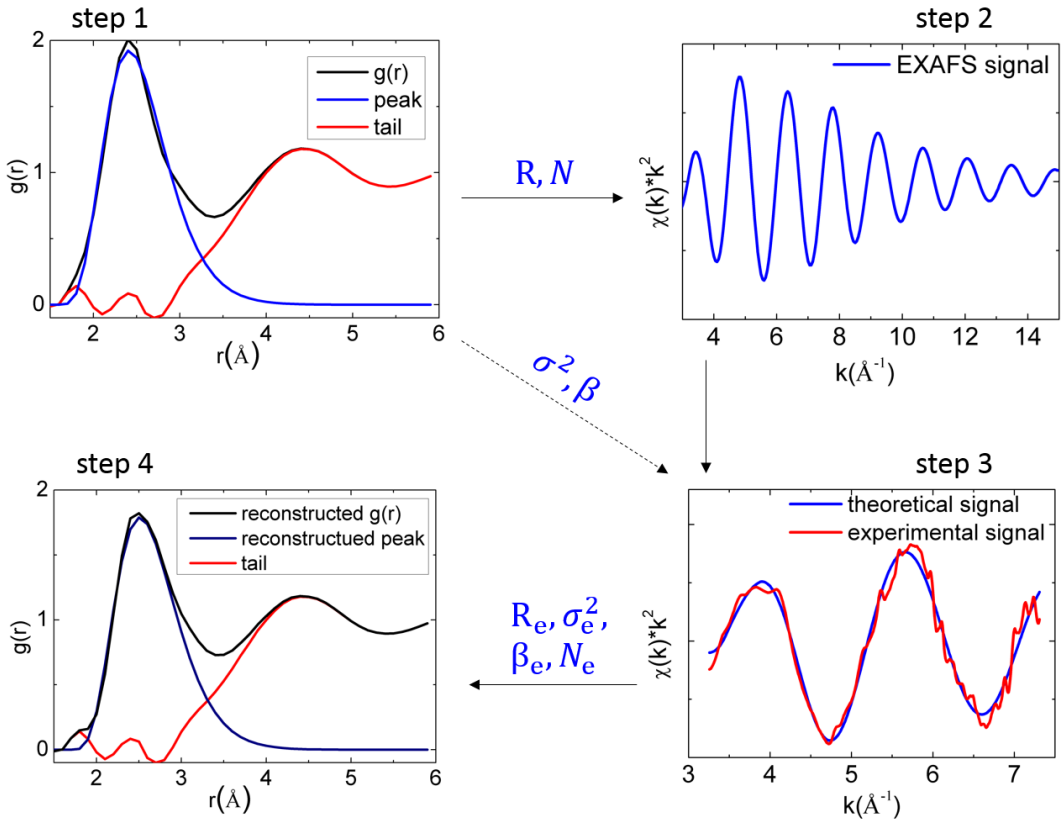

Figure 5.3 – With the program GnXAS [56] the fitting procedure for a liquid is performed in four steps.

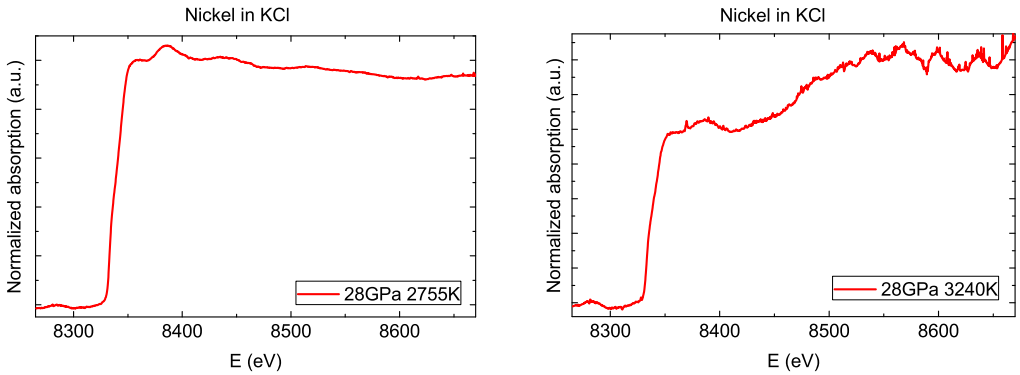

(a) Spectrum with smooth, physical background.

(b) Spectrum with distorted, unphysical background.

Figure 5.4 – Liquid nickel spectra.

of the g(r).

A first treatment of the liquid nickel data with this approach gave very unstable fits. The k range of the data obtained in the diamond anvil cell under extreme conditions is in fact shorter than data that can be collected at ambient pressure. Moreover due to the presence of the DAC and the higher pressure and temperature involved (and thus the smaller samples) the data are more noisy than the ones previously obtained by Di Cicco et al. [41]. In addition, sometimes the liquid is not homogeneous, and this results in a distorted background. An example of treatable and non-treatable spectra is shown in Figure 5.4. Only the best spectra can thus be selected for the analysis; fast measurements under extreme conditions come with a price.

5.3.1 Special approach for data under extreme conditions

Since fitting our data with the approach described could not provide stable fit results, we adopted a more crude method that allows to evaluate the first neighbour distance in the liquid. With this method the structural parameters are not fitted, but several model signals are compared with the experimental data; the model giving the best agreement defines the distance between first neighbour atoms. This analysis though is insensitive to the mean square relative displacement and the asymmetry of the radial distribution function.

More sophisticated analysis methods used in previous studies of liquids, such as the EXAFS analysis on nickel or copper at ambient pressure [43, 41], are not possible on these short and noisy data. The short range is a result of measurements recorded on an energy dispersive beamline, which for the time being is however the only way

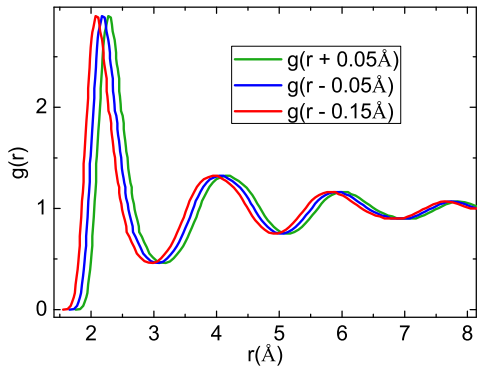

(a) Radial distribution function calculated by Lee at 81 GPa and 3000 K [94] was rigidly translated to several distances.

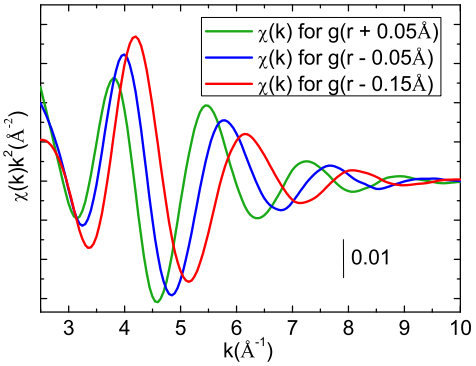

(b) The EXAFS signal associated to the translated radial distribution functions was calculated through Equation 5.4.

Figure 5.5 – The radial distribution function is translated to several distances and the EXAFS signal is calculated for each of them.

to record spectra in the seconds time scale. The noise is instead of non-statistical nature, due to the size of the beam. The size of the beam specified is in fact the full width half maximum (FWHM). The size including the tails of the Gaussian describing the intensity of the beam in space would then be ∼10 μm. If the sample is very small (20 x 20 μm^2) and the measurement is not performed exactly in the centre, there will be a portion of the transmitted intensity that cannot be correctly normalized, thus giving this non-statistical noise.

The method consists of several steps. At first a radial distribution function g(r) is chosen, and it is rigidly translated to several distances, see Figure 5.5(a) for an example. The program *grxas* then calculates the EXAFS signals associated to the radial distribution functions exploiting Equation 5.4 and it provides the distances corresponding to the leading frequency of the resulting $\chi(k)$. The calculated EXAFS signals are shown in Figure 5.5(b). The density has to be provided, as well as the phase shifts and cross sections, that have to be previously calculated for each material with the package *phagen*.

The background extraction and the Fourier transform of the measured EXAFS are performed with the package *fitheo*, that also allows to compare the theoretical EXAFS signal with the extracted experimental one. The "atomic" background subtraction and the match between the model $\chi(k)$ and the experimental data is simultaneous. The presence of double electron excitations [60] was considered in the background extraction. The same procedure is repeated for several translated radial distribution functions. Only the radial distribution function whose associated EXAFS signal is able to reproduce the data is the one that describes the system. In Figure 5.6(a) an

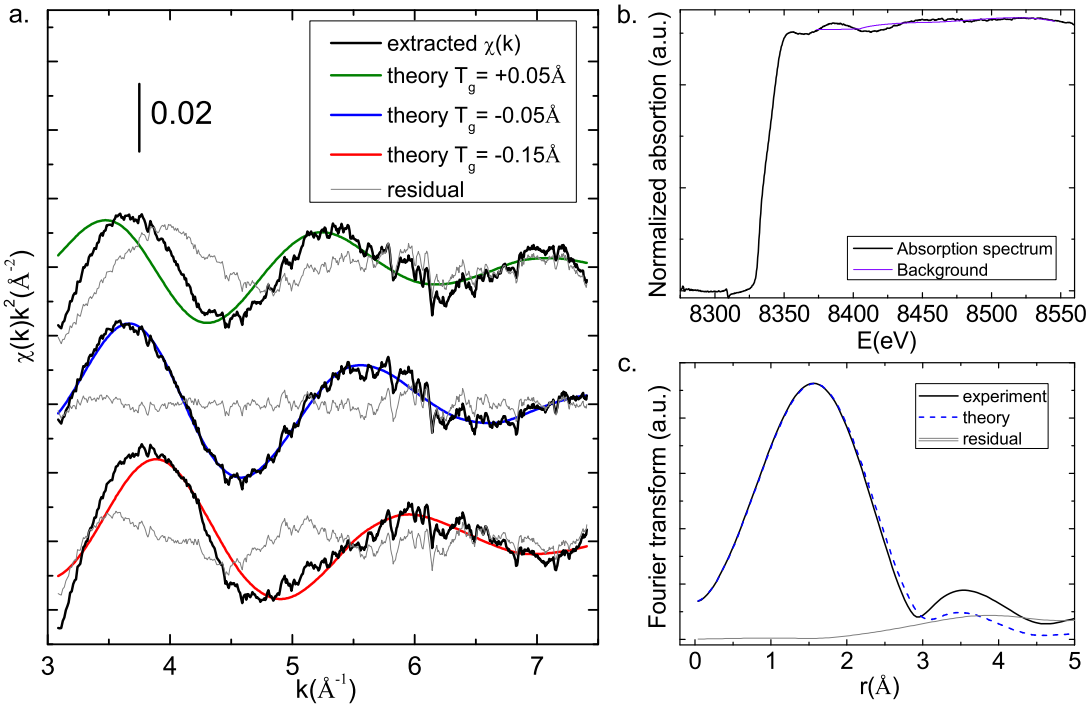

Figure 5.6 – (a.) The experimental EXAFS signal extracted from an absorption spectrum measured at 19 GPa and 2410 K is compared with the three theoretical EXAFS signals calculated from the radial distribution functions in Figure 5.5. T_g indicates the translation of the g(r). The theoretical signal in blue, corresponding to a translation of -0.05 Å of the original g(r), gives the best agreement with the experimental EXAFS. (b.) and (c.) Background extraction of the absorption spectrum at 19 GPa and 2410 K and Fourier transform of the signal giving the best agreement (the one in blue).

example is shown, where it is clear that the experimental EXAFS signal matches well with the theoretical one calculated from the g(r) translated by -0.05 Å. The background extraction of the absorption spectrum and the Fourier transform of the signal are shown in Figure 5.6(b and c).

A fit with a gamma distribution model, such as in Equation 5.2, of the g(r) that shows the best agreement with the EXAFS spectrum defines the first neighbours distance. The closest translated radial distribution functions whose agreement with the experimental signal is poor gives an overestimation of the error bar.

Nickel:

P (GPa)	0	11	19	28	33	45	51	90	102
T (K)	-	2220	2420	2750	2990	3120	3350	3200	3600
T_g (Å)	0.05	0.0	-0.05	-0.05	-0.1	-0.1	-0.1	-0.175	-0.175
R (Å)	2.41	2.36	2.32	2.32	2.27	2.27	2.27	2.19	2.19

Cobalt:

P (GPa)	0	10	31	41	56	68	83
T (K)	-	2020	2930	2730	3590	3658	3624
T_g (Å)	0	0	-0.1	-0.1	-0.15	-0.2	-0.2
R (Å)	2.41	2.41	2.31	2.31	2.26	2.21	2.21

Table 5.4 – Pressure and temperature conditions of the spectra of liquid nickel and cobalt whose EXAFS was analysed and the measured distance of the first neighbour distance. Note that with 0 GPa we actually mean ambient pressure: $1.013 \cdot 10^{-4}$ GPa. At this pressure the temperature is not known. $T_g(\text{Å})$ is the translation of the radial distribution function that gave the best match with the experimental data and R(Å) the resulting position of the first peak. The error on the distance is 0.05 Å, which is an overestimation of the error bar for the two materials, see Figure 5.6.

5.4 Measured compression of nickel

The procedure for data analysis described above was applied to several absorption spectra of liquid nickel at different pressures along the melting curve. The starting radial distribution function was the one calculated by Lee at 81 GPa and 3000 K and it was translated at several distances with steps of 0.05 Å.

In Table 5.4 the pressure and temperature conditions of the liquid spectra analysed are shown, with the resulting translations of the radial distribution function and the corresponding distances as a function of pressure.

The match between experimental and theoretical EXAFS signals is shown in the left panel of Figure 5.7(b). In the right panel the resulting compression of the first neighbours distance is shown in comparison with the literature. The last two points at high pressure (about 90 and 100 GPa) were discussed in Section 3.3. They are liquids even if their temperature is below the accepted melting curve. They were found to be contaminated with about 7% of NiO. This amount of NiO is enough to affect the melting temperature, but is too low to have an influence on the first shell distance, see Figure 3.10c. As additional proof we performed a fit of the data with a Vinet equation of state, see Appendix B.0.2, including or excluding the last two points. The two fits are shown in the right panel of Figure 5.7(b); the purple curve includes the last two points, while the blue one does not. The difference between the two curves in

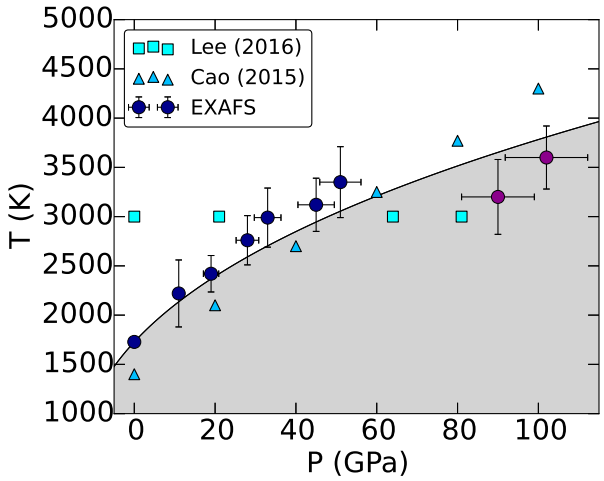

(a) Pressure-temperature conditions for the data of liquid nickel shown here below.

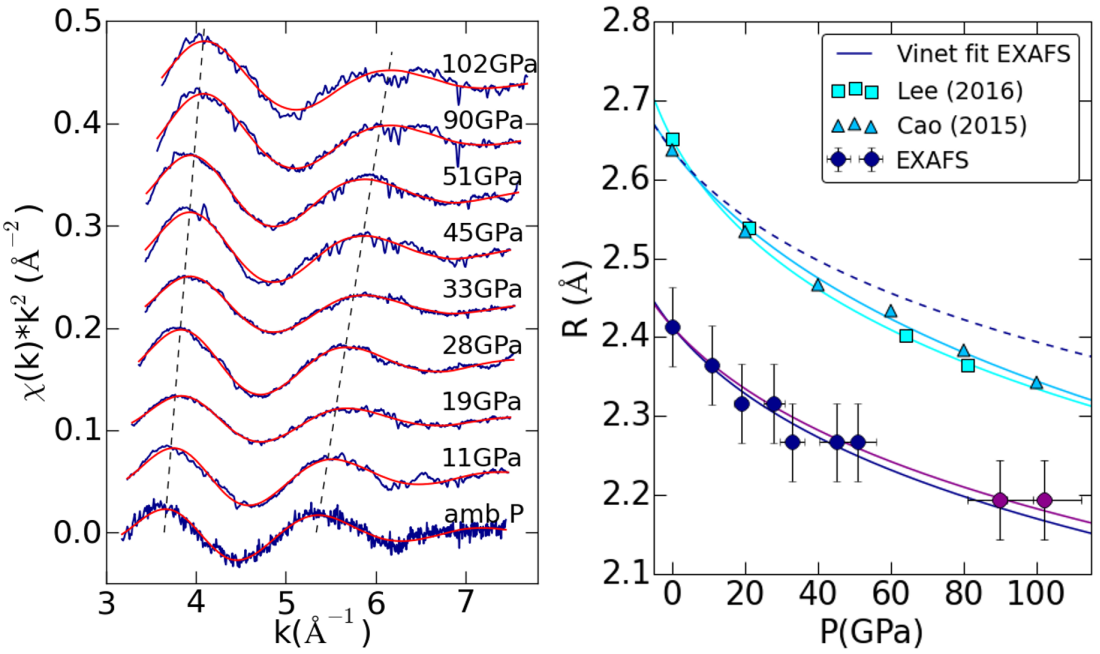

(b) Left panel: liquid nickel EXAFS signals of the analysed spectra (blue curves) at the different pressures compared with the theory (red curves). Right panel: measured first neighbours distances as a function of pressure. The last two points, in purple, are contaminated with 7% of NiO. The points are fitted with a Vinet equation of state that serves as a guide for the eyes. The purple curve includes the last two points, the blue curve does not. For easier comparison with the literature the Vinet curve fitting the data up to 60 GPa was translated on the first neighbour distance calculated by Cao at ambient pressure and is represented as a dashed curve.

Figure 5.7 – Data analysis of nickel data in the liquid phase measured with EXAFS and compare with calculations.

negligible, but the last two points will always be shown but not considered in the fits in the discussion that follows in this chapter.

The blue curve is then translated (blue dashed curve) upon the theoretical calculations of the distance performed by Cao [32] for better comparison with the literature. Moreover it is known that the distance in EXAFS is correlated to the E_0 parameter, the energy mismatch between theory and experiment, not known *a priori* but imposed during the data analysis. For this reason EXAFS is reliable for relative changes of the distances but not for their absolute values. The results often have to be slightly translated to be in agreement with the literature.

The resulting trend shows, as expected due to the temperature differences, less compression than the theoretical curve calculated by Lee [94]. While in the case of Lee the temperature is constant (3000 K) in our measurements the temperature varies from 1730 K to 4000 K. Our result, though, is not in agreement with the compression found by Cao [32] either, even if both curves are calculated along the melting line.

5.5 Measured compression of cobalt

The same procedure used for nickel was applied on spectra of liquid cobalt along the melting curve. The radial distribution function used here was calculated with the procedure presented in Section 4.2.2 from 510 different thermodynamic configurations of a supercell containing 128 atoms, calculated at 44 GPa and 2500 K. The resulting g(r) was translated at several distances with steps of 0.05 Å.

The conditions of the liquid cobalt spectra analysed are summarized in Table 5.4, together with the translations of the radial distribution function that give a good agreement with the data and the resulting first shell distances.

The EXAFS signals matching with the ones calculated from the radial distribution functions are presented in Figure 5.8(b). In the right panel of the same figure the resulting compression is shown compared to theoretical calculations. The data derived from EXAFS are fitted with a Vinet equation of state up to 80 GPa. For an easier comparison the curve is translated as a dark green dashed curve upon the Vinet equation of state that fits the calculations at ambient pressure.

Liquid cobalt along the melting curve shows a compression that is very similar to the one of nickel (about 0.2 Å over 80 GPa). If compared with calculated values along the isotherm at 5000 K it shows much less compression. A direct comparison with theoretical calculations along the melting curve is, for the time being, not possible.

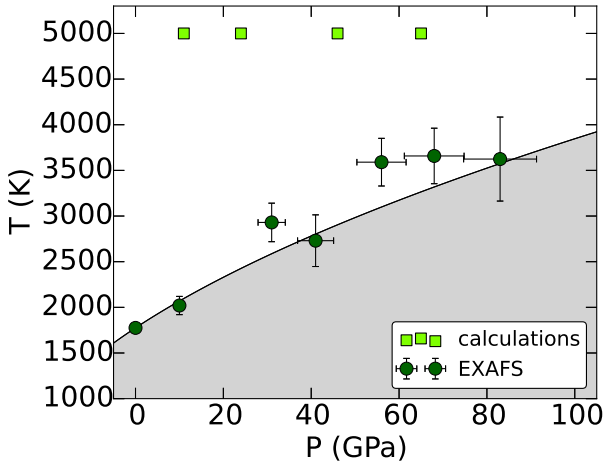

(a) Pressure-temperature conditions for the data of liquid cobalt shown here below.

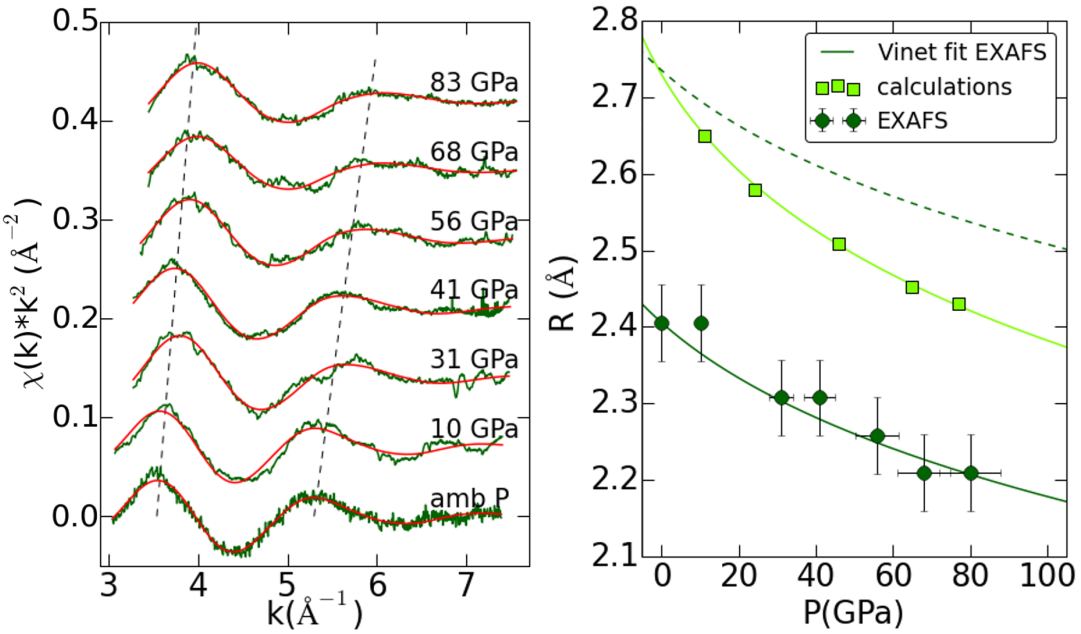

(b) Left panel: liquid cobalt EXAFS signals of the analysed spectra (green curves) at the different pressures compared with the theory (red curves). Right panel: measured first neighbours distances as a function of pressure. The points are fitted with a Vinet equation of state that serves as a guide for the eyes. The dashed line is the Vinet curve translated on the Vinet fit of the calculated distance at ambient pressure.

Figure 5.8 – Data analysis of cobalt data in the liquid phase measured with EXAFS and compare with calculations.

By analogy with the case of nickel, see Figure 5.7(b), we expect that the calculations of R(P) along the melting curve will not differ significantly from those at constant T=5000 K.

5.6 Discussion

The results presented in this chapter to our knowledge provide for the first time a measurement of the compression of the bond between first neighbour atoms in liquid nickel and cobalt under pressure. Due to the quality of the data, we adopted a method of analysis that allows to extract only the bond distance, while other parameters, such as the coordination number, remain hidden. The aim of this section is to open a discussion based on a qualitative evaluation of the volume and the coordination number.

To understand the discrepancy between experiment and theory, shown in the trend of the first neighbour distance as a function of pressure, we evaluated the volume as a function of pressure from the EXAFS data and compare it to the theoretical compression of the volume.

The evaluation of the volume from the first neighbours distance is straightforward for a crystalline solid whose structure is well known and characterized by a unit cell that is repeated in space. In a liquid however, the structure is much more complex, as described at the beginning of this chapter in Section 5.1. The volume can be calculated from the experimental radial distribution function in ways that will be presented at the end of this section.

In the following, the volume compressions of the liquid obtained with different methods are presented and compared.

5.6.1 Volume from theoretical calculations

The theoretically calculated atomic volumes, defined as the ratio between the supercell volume and the number of atoms in the supercell, are here presented. Studies on the compression of nickel can be found in the literature at a constant temperature and at a temperature following the melting curve. These calculations were performed by Lee [94] and Cao [32] respectively, and the volume is calculated as the inverse of the density ρ reported in Tables 5.1 and 5.2.

The compression of cobalt at constant temperature was calculated in this work by means of AIMD; the volumes are calculated as the inverse of the density reported in

Table 5.3. The compression at a temperature following the melting curve was instead calculated by Zhang et al. [174].

5.6.2 Volume evaluated with Clausius-Clapeyron equation using the melting curve obtained in this work

The volume of the liquid along the melting curve can be estimated using the Clausius-Clapeyron relation, discussed in Appendix B.0.3 and reported here

$$\frac{\mathrm{dT_m}}{\mathrm{dP}} = \frac{\Delta \mathrm{V_m}}{\Delta \mathrm{S_m}}. \tag{5.5}$$

The volume of the liquid along the melting curve is evaluated in the same way for both nickel and cobalt. The steps followed are here presented:

1. $\frac{\mathrm{dT_m}}{\mathrm{dP}}$ is obtained from our measured melting curves
2. $\Delta \mathrm{S}$ is assumed constant with pressure (assumption commonly adopted in the literature [89])
3. the volume of the solid as function of pressure, $\mathrm{V_{solid}(P)}$, is evaluated using known V(P) equations from $\frac{\Delta \mathrm{V}}{\mathrm{V_0}} = \alpha_{\mathrm{V}} \Delta \mathrm{T}$
4. the volume of the liquid as a function of pressure, $\mathrm{V_{liquid}(P)}$, is calculated as

$$\mathrm{V_{liquid}} = \mathrm{V_{solid}} + \frac{\mathrm{dT_m}}{\mathrm{dP}} \cdot \Delta \mathrm{S} \tag{5.6}$$

In the literature several measurements and calculations have been performed to determine the compression of solid nickel and cobalt along different isotherms. The equation of state at ambient temperature up to 150 GPa was measured by Dewaele for the two metals by means of X-ray diffraction [40]. Zeng [171] instead calculated the EOS for solid nickel at different temperatures up to 180 GPa and 3000 K. EOS at different temperatures were measured for fcc cobalt with X-ray diffraction up to 60 GPa and 2500 K [12].

Using the equation of thermal expansion

$$\alpha_{\mathrm{V}} = \frac{1}{\mathrm{V}} \Big(\frac{\partial \mathrm{V}}{\partial \mathrm{T}} \Big)_{\mathrm{P}} \tag{5.7}$$

and in the hypothesis that at these temperatures the volume coefficient of thermal expansion does not change with temperature, the $\alpha_{\mathrm{V}}(\mathrm{P})$ was calculated as a function of pressure. For nickel it is derived using the EOS at 2000 K and 3000 K, for cobalt between 1500 K and 2000 K. The values at some of the pressures are reported in Table 5.5; the volume coefficient of thermal expansion decreases with pressure and is

P (GPa)	0	25	50	75	100
α_V(P) nickel	4.99e-05	2.96e-05	2.15e-05	1.66e-05	1.32e-05
α_V(P) cobalt	5.62e-05	3.94e-05	3.14e-05	2.63e-05	2.27e-05

Table 5.5 – Volume coefficient of thermal expansion for nickel and cobalt as a function of pressure.

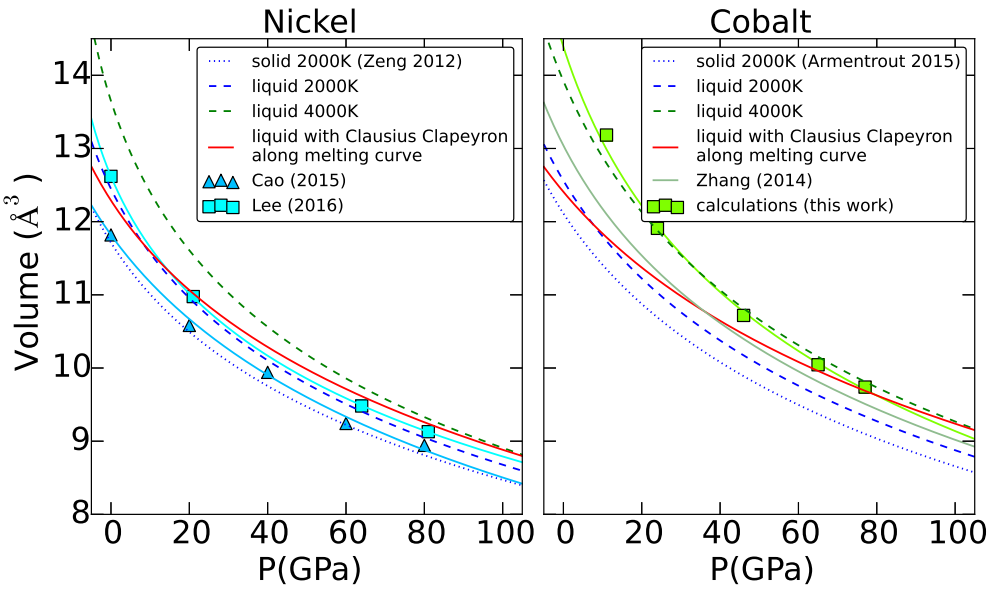

Figure 5.9 – Equation of states of the liquid at different temperatures evaluated from the equation of states of the solids calculated by Zeng [171] for nickel and measured by Armentrout [12] for cobalt. The red curve is the evaluation of the volume of the liquid at the melting temperature, using Equation 5.6 with our experimental melting curves.

smaller for nickel. With the volume coefficient of thermal expansion and knowing the melting temperatures for the two materials, the volume of the solid along the melting curve can be calculated using Equation 5.7.

This is a very strong approximation, and as further development we plan to obtain a more realistic estimation of the high pressure and high temperature solid phase using a Mie-Gruneisen-Debye model [176, 12].

Using the Clausius-Clapeyron equation (Equation 5.5) and in the assumption that the variation of entropy does not change as a function of pressure the volume of the liquid along the melting curve is evaluated. The value considered for the variation of entropy is 10.1 J/mol·K for nickel [73] and 8.55 J/mol·K for cobalt [174]. Figure 5.9 represents for the two materials the equation of state of the solid at 2000 K (dotted curve), the equation of state of the liquid calculated with the Clausius-Clapeyron re-

lation at 2000 K and 4000 K (dashed curves), and the evaluation of the liquid volume trend as a function of pressure and temperature along the melting curve (red solid curve). The volume along the melting curve is lower than the curve at 2000 K ad low pressure (as expected, since $T_m <$ 2000 K at ambient pressure) and reaches the one at 4000 K around 100 GPa. The trend of the volume along the melting curve is in agreement with Cao [32] for nickel (except between 80 and 100 GPa). Our calculations for cobalt at 5000 K follow closely the estimated curve ad 4000 K. In the case of cobalt it is in disagreement with Zhang [174].

The approximation used here that the melting entropy ΔS_m does not change with pressure is commonly used in the literature [89]. It is justified by calculations performed on cobalt and iron by Zhang [174, 172], where it is proposed that there could be a slight decrease over pressure, but it was never measured due to experimental difficulties associated to the measurement of the volume of the liquid as a function of pressure.

5.6.3 Volume and coordination number calculated from the g(r) derived from EXAFS measurements in this work

A way to determine the volume of a liquid starting from a radial distribution function was already introduced in this chapter and it exploits Equation 5.3 resulting in

$$V = \frac{4\pi \int_0^{r_{min}} g(r) r^2 dr}{N_C}. \tag{5.8}$$

This approach is a zero order approximation because the radial distribution function used in the analysis is always the translation of the same g(r). The shape of first peak is thus always the same for all the pressure and temperature conditions (see Figure 5.5(a)).

As discussed in Section 5.4, EXAFS is not sensitive to the absolute values but only to relative changes. For this reason for nickel all the radial distribution functions in agreement with our EXAFS data were translated in order to obtain at ambient pressure a first neighbours distance of the same value of the one calculated by Cao [32] at ambient pressure. Nickel EXAFS data were thus translated by 0.22 Å, see also Figure 5.7(b). The integral $\int_0^{r_{min}} g(r) r^2 dr$ is then calculated at the different pressures and is shown in the top left panel of Figure 5.10. The situation is more complicated in the case of cobalt, where the only available distance is at 5000 K. As a first approximation the radial distribution functions were translated in order to obtain at ambient pressure a first neighbour distance in agreement with the AIMD calculations we performed on cobalt at 5000 K. This is a very strong approximation, and we plan as

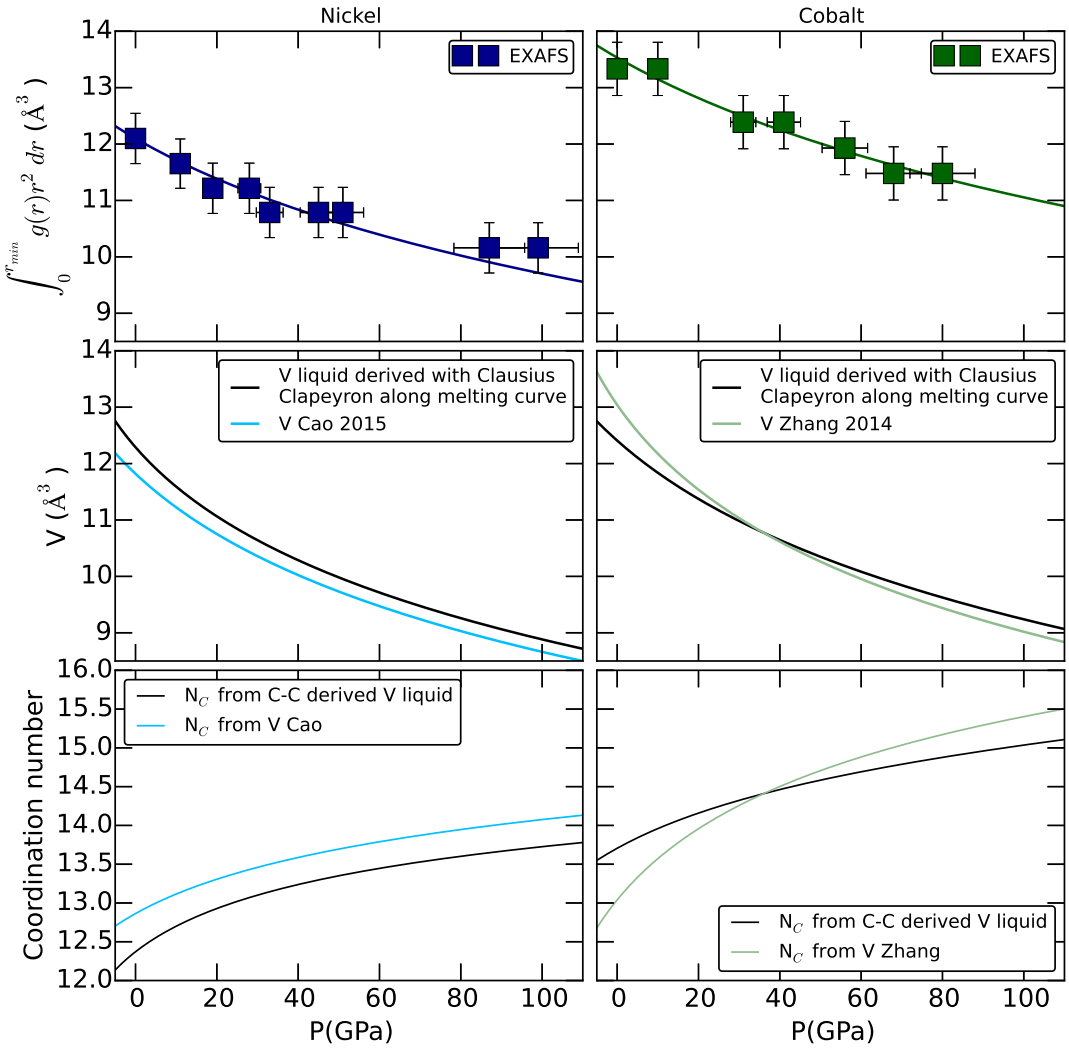

Figure 5.10 – Top panels: The integral of the radial distribution function multiplied by r^2 up to the first minimum is shown in comparison with the evaluated volume of the liquid along the melting line. Bottom panels: Coordination number as a function of pressure for nickel and cobalt.

further development to perform AIMD calculations at 2000 K, in order to obtain a more realistic distance along the melting curve, but this is not yet available for the time being. Cobalt EXAFS data were thus translated by 0.33 Å. The integral was then calculated for the different radial distribution functions and the results are shown in the top right panel of Figure 5.10.

Since the coordination numbers nor the volumes are known *a priori*, in Equation 5.8 one of the two variables has to be imposed from the literature. In this work the volume is imposed equal to the theoretical value and the coordination number is derived. For nickel the The volume is thus at first imposed to be the one calculated by Cao and Zhang, for nickel and cobalt respectively, and then to the one evaluated using the Clausius-Clapeyron relation coupled to the melting curves measured in this work.

In Figure 5.10 the results for nickel and cobalt are shown. In the middle panel the theoretical values of the volume are represented as a function of pressure. In the bottom panel the calculated coordination numbers are represented. In both cases we find an increase of the coordination number with increasing pressures, 12% for nickel and 10-25% for cobalt.

In the case of nickel this results is in disagreement with the theoretical calculations performed by Lee [94] and [32], where the coordination number is constant or decreases with pressure respectively.

In the case of cobalt instead the result agrees with the AIMD calculations performed on cobalt in this work, where the coordination number slightly increases (8%).

5.6.4 Volume in the hard sphere model

Another way of calculating the volume is in the framework of a hard sphere model [13]

$$\eta = \frac{\pi\rho\sigma^3}{6},$$

where the compacity or packing factor η, representing the percentage of the total volume occupied by hard spheres, is written as a function of the density ρ and the hard sphere diameter σ. From this equation the volume can thus be expressed as

$$\mathrm{V} = \frac{\pi\sigma^3}{6\eta}. \tag{5.9}$$

The packing factor η for liquid nickel and cobalt is 0.45 at ambient pressure [164].

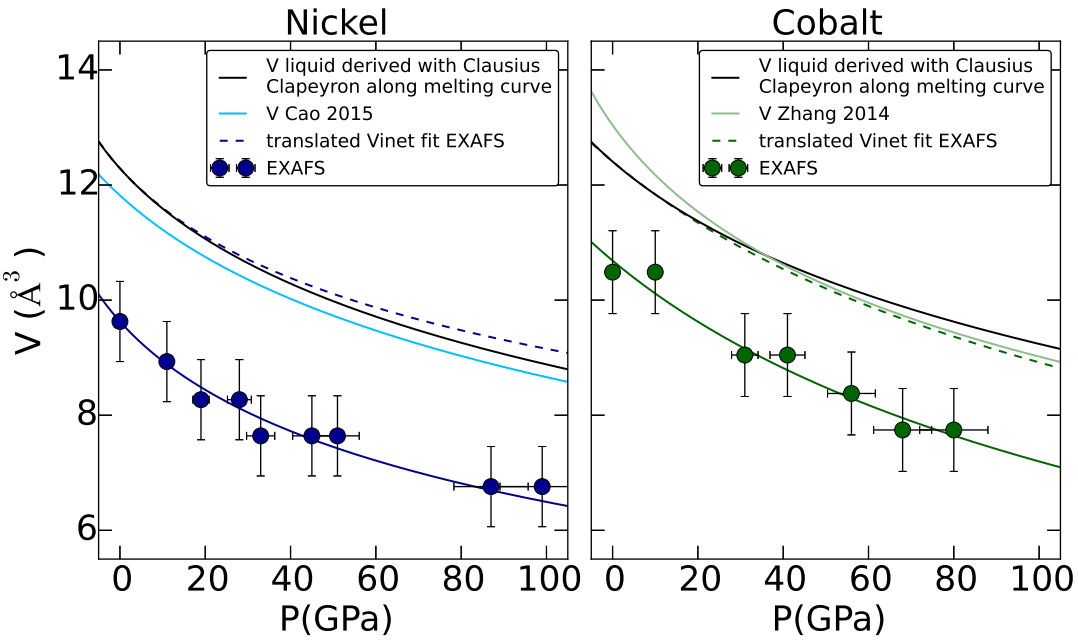

Figure 5.11 – The experimental volume calculated as a function of pressure by means of Equation 5.9 is represented in comparison with the calculated and the evaluated volume of the liquid along the melting curve. The dashed curve is the fit of experimental volume translated upon the evaluated volume at ambient pressure.

The hard sphere diameter σ as a function of pressure was determined as

$$\sigma(\mathrm{P}) = \sigma_0 + \mathrm{T_g}(\mathrm{P}), \quad \text{where} \quad \sigma_0 = \left(\frac{6\eta \mathrm{V}_0}{\pi}\right)^{\frac{1}{3}},$$

$\mathrm{T_g}(\mathrm{P})$, that is reported in Table 5.4, represents the translation of the reference radial distribution function $\mathrm{g_{ref}}(\mathrm{r})$ applied in order to obtain an agreement with the experimental data and V_0 is the volume associated to the reference radial distribution function. The $\mathrm{g_{ref}}(\mathrm{r})$ is the radial distribution function calculated by Lee at 81 GPa and 3000 K for nickel and in this work at 44 GPa and 2500 K.

The results for nickel and cobalt are summarized in Figure 5.11 in comparison with the evaluated volume of the liquid along the melting curve in the assumption of:

1. validity of the hard sphere model
2. packing factor η pressure independent

The dashed curve, representing the translation of the experimental volume on the theoretical one shows a very good agreement for nickel.

Our $V_{liq}(P)$ curve is smooth, as the calculated ones, consistent with the statement that in late transition metals there are no liquid-liquid phase transitions [94]. In the case of cobalt the agreement is poorer with both the theoretical and the evaluated volume.

5.7 Critical issues

The data shown in this chapter provide the first measurement of the compression of liquid nickel and cobalt up to about 1 Mbar. The challenges encountered in the analysis of the data are mainly due to the quality of the data that do not allow a standard fitting procedure.

The main problems are due to the short k-range of the data, the low amplitude of the EXAFS oscillations that makes the background extraction more challenging and the non statistical noise in the data that appears at higher pressures when the sample is smaller.

Background

The distortion of the background provides a significant limitation for the extraction of an EXAFS signal. It was shown in Section 3.2.3 that spectra of melts obtained by laser heating a sample in a DAC often show an irregular shape. As a consequence it is very rare to obtain data with smooth, physical background, and this is the reason why only few spectra of liquids can actually be analysed to extract a bond length.

The results obtained on the few spectra that could be analysed are however very promising and allow to give for the first time a measurement of the first neighbours distance as a function of pressure, whose trend shows a slight difference with respect to calculations.

Entropy evaluation

Thermodynamic parameters such as the entropy of melting, can in principle be derived from the Clausius-Clapeyron relation:

$$\Delta S_m = \frac{dT_m}{dP} \cdot \Delta V_m, \tag{5.10}$$

where the variation of volume upon melting is $V_m = V_{liq} - V_{solid}$. While V_{liq} is the volume of the first liquid after the melting, V_{sol} is the volume of the solid just before

melting. This implies precise knowledge of:

1. $\mathrm{dT_m/dP}$
2. $\mathrm{V_{sol}}$
3. $\mathrm{V_{liq}}$

In the previous chapter we evaluated the volume of the solid along the melting curve exploiting the experimental and theoretical equation of states in the literature. Using Equation 5.10, where the volume of the liquid is calculated with the hard sphere model, $\mathrm{V_{liq}} = \pi\sigma^3/(6\eta)$, we can evaluate the melting entropy as a function of pressure by imposing on the experimental data a translation that allows to obtain a melting entropy of 10.1 J/mol·K at ambient pressure [73]. In Figure 5.11 is represented the EXAFS derived volume using the hard sphere model (blue dashed curve) translated upon the Clausius Clapeyron derived volume of the liquid evaluated imposing a constant entropy (black curve). Using the dashed curve to evaluate $\Delta\mathrm{S_{100GPa}}$ from Equation 5.10 gives 23 J/mol·K, whereas the black curve is calculated using 10 J/mol·K. However, the difference between these two curves at P=100 GPa is much less than the error bar. We therefore conclude that we do not have the sensibility to evaluate $\Delta\mathrm{S_m}$. A reduction of a factor 10 of the error bar would be required.

5.8 Conclusions

In this work we extracted for the first time information on the local structure of liquid nickel and cobalt under pressure, namely the first neighbour distance as a function of pressure. Moreover, the comparison of the experimental liquid volume compression with the theoretical one suggests an increase of the coordination number with pressure of about 15% for nickel and 10-20% for cobalt.

The present quality of the data does not allow to extract directly structural parameters other than the distance between first neighbours. The present experimental limitations will partially be overcome with the EBS (Extremely Brilliant Source) project of the ESRF. The smaller horizontal source size and the reduced emittance will allow the construction of an upgraded ID24 beamline, where one of the two branches will be transformed in a fast scanning XAS beamline. It will be possible to record an EXAFS spectrum in one second with a longer k-range and a smaller X-ray spot (1 μm full size in both directions). This will provide higher quality data and the possibility to work on smaller samples. With a spot of this size it will be possible to probe the full outer core down to the ICB.

Chapter 6

Conclusions

This Thesis consists of a systematic study of the melting curves and the local structure properties of compressed liquid nickel and cobalt: i.e. 3d metals with important technological and geophysical implications. The investigation has been carried out with X-ray absorption spectroscopy, coupled with *ab-initio* calculations. X-ray absorption spectroscopy, with its short order sensitivity, is a suitable technique to probe the local structure in condensed matter. The aim of the theoretical calculations is to validate the melting criterion adopted to define the transition to the liquid phase, to supply a theoretical radial distribution function that provides a starting point for the analysis of the liquid and finally to evaluate a theoretical compression to compare the experimental results with.

The experimental techniques nowadays available for studies of extreme conditions were fully exploited: nano polycrystalline diamond anvils that do not produce sharp diffraction peaks in the spectra, a laser heating system that allows to reach temperatures up to 4000 K, an X-ray beam that probes a small region of the sample where the temperature can be considered uniform, and finally a fast detection of the absorption spectrum that allows to limit the exposure of the sample to the laser. By combining these technologies it was possible to measure, for the first time with X-ray absorption spectroscopy, the melting curve of nickel and cobalt, up to 1 Mbar and 4000 K, and the compression of the first neighbour bond.

In the following, the main results obtained in this work will be summarized and finally the outlook and some general conclusions will be drawn.

Melting curves

The criterion recently adopted to measure the melting curve of iron with X-ray ab-

sorption spectroscopy was reproposed in this work for nickel and cobalt with the aim of providing a systematic validation for all the 3d metals showing similar electronic and crystal structures.

The criterion was validated for nickel, by a FIB and SEM analysis on the recovered samples, where the difference in the shape of a heated sample that remained solid compared to one that was molten is noticeable.

The criterion was applied systematically and the melting temperature was detected at several pressures, thus providing the melting curve up to 1 Mbar for the two materials. The melting curve of nickel measured by XAS is in good agreement with the one previously measured by XRD, finally proving that the two techniques probe the same phenomenon. The melting curve of cobalt proposed in this work instead provides a first experimental measurement performed with an X-ray technique.

The melting curves obtained in this work were compared with the melting curve of iron measured by XRD, finding a negligible difference between the three at 100 GPa. As a result it is thus possible to state that the presence in the outer core of Earth of about 5.6 $\%$ and 0.27 $\%$ in weight of nickel and cobalt respectively, gives a minor contribution to the determination of the temperature at the inner core boundary. Therefore the presence of nickel and cobalt can be neglected.

Ab-initio calculations

Ab-initio calculations and simulations of the XANES were performed. Starting from MD generated atomic supercells XANES were calculated with the aim of providing an additional validation of the melting criterion adopted. The calculations confirmed the melting criterion, but they also allow to understand why the detected changes occur. The disappearance of the shoulder and the flattening of the first two oscillations in the XANES reflects two related aspects: from an electronic point of view the structures in the density of the p-states (those that give the recognisable shape in the K-edge XANES of an fcc or hcp material) smear out in the transition to the liquid phase. From the point of view of the atomic structure, the cause of the flattening of the oscillations is given by the different environment that surrounds each absorbing atom in a liquid.

As additional result the evolution of the first neighbour bonds of the liquid under pressure at 5000 K was calculated from the clusters generated at different pressures.

Study of the local structure

XAS data were analysed with the aim to measure the first neighbour distance as a function of the applied pressure, for the liquids along the melting curve. The quality of the data did not allow to obtain directly from the fit other structural parameters such as the mean square relative displacement, indication of the static and thermal disorder, and the coordination number.

The obtained experimental trend of the first neighbour distance compared to theoretical calculations shows that the first neighbour bond compresses less than predicted. This can be due to a bond that at higher pressures becomes more rigid than foreseen, or to a gradual and slight increase of coordination number.

The volume is calculated from the data and it is compared to theoretical calculations. From the comparison it is possible to evaluate the coordination number. Our finding is that the data collected in this work are in agreement with an increase of coordination number of about 10-20 $\%$ for both nickel and cobalt.

Outlook

With this work we made the most of the present experimental techniques available to investigate two "model" systems (nickel and cobalt) for structural studies at extreme conditions. The results are nevertheless not completely satisfying, since structural factors such as the coordination number cannot yet be extracted directly from the data but their variation with pressure can only be evaluated *a posteriori*.

With the Extremely Brilliant Source and the construction of the new branch of the beamline ID24 some of the constraints that limited this work will be eliminated and new perspectives for the analysis initiated with this work will be opened.

A beam size of 1 μm full width will allow to extend these investigations to higher pressures, spanning the full outer core and up to the inner core boundary, with obvious geophysical implications. Moreover a smaller beam size coupled with a fast scanning will allow to record EXAFS spectra on molten matter with a longer k-range, less sensitive to changes in the background, thus leading to a more robust data analysis, which will lead to more accurate structural information and, perhaps, to the evaluation of thermodynamic parameters such as the melting entropy.

The laser heating system will be improved as well by the insertion of a flat-top beam shaper and the use of new objectives with higher spatial resolution. The flat-top beam shaper has the function to transform the circular Gaussian shape of the infrared laser beam into a circular beam with uniform intensity. The new objectives,

now in phase of design, will allow to reduce the spatial resolution from few micrometers to less than 1 μm.

All of these changes will allow to measure spectra in regions with lower temperature gradients and to obtain more precise temperature measurements with a smaller error bar.

In conclusion, with this work we proved that X-ray absorption spectroscopy is a valuable technique for the determination of the melting curve of 3d metals and their alloys with fcc or hcp structure before melting. Melting criteria for materials with different solid structures could be established by following protocols developed in this work.

X-ray absorption spectroscopy, because of its element selectivity, provides a probe complementary to X-ray diffraction for the analysis of liquids under extreme conditions. This will be important in the study of multi-element, more complex, systems. With this work we lay the foundations for the study of more relevant systems such as Fe alloys with light elements and all iron-containing minerals in our planet. The investigation of these materials, at relevant pressure and temperature conditions, with the methods described in this work, will provide valuable knowledge for the understanding of the properties of the Earth's interior, nowadays still obscure.

Appendices

Appendix A

Dipole approximation

In this appendix derivation of Equation 2.2 from Equation 2.1 is illustrated. Considering only the wavefunction of the photoelectron the matrix element can be written as

$$< \psi_f | \hat{\epsilon} \cdot \vec{p}\, e^{i\vec{k}\cdot\vec{r}} | \psi_i > . \tag{A.1}$$

It is known that

$$[\vec{r}, \hat{H}_I] = \frac{i\hbar\vec{p}}{m_e}.$$

This can be easily derived writing the Hamiltonian as the sum of potential and kinetic energy

$$[\vec{r}, \hat{H}_I] = [\vec{r}, \hat{V} + \hat{T}] = [\vec{r}, \hat{V}] + [\vec{r}, \hat{T}].$$

If we calculate the two terms separately we find

$$[\vec{r}, V(r)]f(r) = \vec{r}\,\hat{V}(r)f(r) - \hat{V}(r)\vec{r}f(r) = -\vec{r}\,\frac{Zq^2}{r}f(r) + \frac{Zq^2}{r}\vec{r}f(r) = 0$$

and

$$[\vec{r}, \hat{T}] = [\vec{r}, \frac{\hat{p}^2}{2m_e}] = \frac{1}{2m_e}[\vec{r}, \hat{p}^2] = \frac{1}{2m_e}\Big([\vec{r}, \hat{p}]p + p[\vec{r}, \hat{p}]\Big).$$

Where the property of commutators $[a, bc] = abc - bac + bac - bca = [a, b]c + b[a, c]$ was used.

We derive now the commutator of $\vec{r}$ with the momentum operator $\hat{p}$

$$[\vec{r}, \hat{p}]f(r) = \vec{r}\,\hat{p}f(r) - \hat{p}\vec{r}f(r) = -\vec{r}\,i\hbar\,\frac{\partial}{\partial r}f(r) + i\hbar\frac{\partial}{\partial r}\Big(\vec{r}\,f(r)\Big) =$$

$$= -\vec{r}\,i\hbar\,\frac{\partial f(r)}{\partial r} + i\hbar\frac{\partial\vec{r}}{\partial r}f(r) + i\hbar\vec{r}\frac{\partial f(r)}{\partial r} = i\hbar\frac{\partial\vec{r}}{\partial r}f(r) = i\hbar f(r)$$

hence $[\vec{r}, \hat{p}] = i\hbar$ and

$$[\vec{r}, \hat{H}_I] = \frac{1}{2m_e} i2\hbar\hat{p} = \frac{i\hbar\vec{p}}{m_e}. \tag{A.2}$$

The momentum operator can then be obtained from Equation A.2 and substituted in Equation A.1.

$$< \psi_f|\hat{\epsilon} \cdot \vec{p}\, e^{i\vec{k}\cdot\vec{r}}|\psi_i >= -i\frac{m_e}{\hbar} < \psi_f|e^{i\vec{k}\cdot\vec{r}}\hat{\epsilon} \cdot [\vec{r}, \hat{H}_I]|\psi_i >=$$

$$= -i\frac{m_e}{\hbar}\Big(< \psi_f|e^{i\vec{k}\cdot\vec{r}}\hat{\epsilon} \cdot \vec{r}\,\hat{H}_I|\psi_i > - < \psi_f|\hat{H}_I\hat{\epsilon} \cdot \vec{r}\, e^{i\vec{k}\cdot\vec{r}}|\psi_i > \Big) =$$

$$= -i\frac{m}{\hbar}\Big(< \psi_f|e^{i\vec{k}\cdot\vec{r}}\hat{\epsilon} \cdot \vec{r}\, E_i|\psi_i > - < \psi_f|E_f\hat{\epsilon} \cdot \vec{r}\, e^{i\vec{k}\cdot\vec{r}}|\psi_i > \Big) =$$

$$= i\frac{m_e}{\hbar} < \psi_f|\hat{\epsilon} \cdot \vec{r}\, e^{i\vec{k}\cdot\vec{r}}(E_f - E_i)|\psi_i >= im_e\omega_{fi} < \psi_f|\hat{\epsilon} \cdot \vec{r}\, e^{i\vec{k}\cdot\vec{r}}|\psi_i > . \tag{A.3}$$

Moreover we assume that the wavelength of the electromagnetic radiation associated to the transition between different atomic energies is generally much larger than the size of the atom. This means that $\vec{k} \cdot \vec{r} \ll 1$ and thus the exponential term $e^{i\vec{k}\cdot\vec{r}}$ can be expanded as $1 + i\vec{k} \cdot \vec{r} + \ldots$. The corresponding expansion of Equation A.3 gives the dipole term, the quadrupole term etc.. In the dipole approximation only the first order is considered leading to

$$< \psi_f|\hat{\epsilon} \cdot \vec{p}\, e^{i\vec{k}\cdot\vec{r}}|\psi_i > \propto < \psi_f|\hat{\epsilon} \cdot \vec{r}\,|\psi_i >$$

as in Equation 2.2.

Appendix **B**

Useful equations

Some of the equations that are commonly used in high pressure physics and that were used in this work for the interpretation of the experimental results are here briefly presented.

B.0.1 Simon-Glatzel equation

The Simon-Glatzel equation is an empirical way of describing the trend of the melting temperature of a solid as a function of pressure. It was proposed for the first time by Simon and Glatzel in 1929 [144], and since then it described satisfactorily the melting curves of different substances [125].

It is usually written as

$$\frac{P - P_0}{a} = \left(\frac{T_M}{T_0}\right)^c - 1$$

where T_0 and P_0 are the temperature and the pressure of the triple point and a and c are parameters that depend on the substance. The pressure of the triple point is for most of the substances very close to zero and thus neglected, making T_0 the melting temperature at ambient pressure.

The formulation used in this work is then

$$T_M(P) = T_0 \times \left(\frac{P}{a} + 1\right)^{\frac{1}{c}}. \tag{B.1}$$

B.0.2 Vinet Equation of State

The Equation of State (EOS) is a thermodynamic equation that relates volume, pressure and temperature of a particular phase of a substance. The effect of pressure

along an isotherm on a material can be quantified with the Bulk modulus K_0 as

$$\mathrm{K}_0 = \rho\Big(\frac{\mathrm{dP}}{\mathrm{d}\rho}\Big)_{\mathrm{T}},$$

where $\mathrm{d}\rho$ is the variation of density caused by the variation dP of pressure applied [39] and from which it is possible to write

$$\mathrm{P(V)} = -\mathrm{K}_0\frac{\mathrm{V}-\mathrm{V}_0}{\mathrm{V}_0}.$$

The Bulk modulus, however, is not constant with pressure and a new parameter such as the pressure derivative of the Bulk modulus K_0' can be introduced for a better description. Among the EOS available to describe the relationship between P and V that use parameters such as K_0 and K_0' we used the one derived by Vinet [161]. Vinet EOS already gave good results for several transition metals among which nickel and cobalt [40] and its formulation is

$$\mathrm{P} = 3\mathrm{K}_0\Big(\frac{\mathrm{V}}{\mathrm{V}_0}\Big)^{-\frac{2}{3}}\Big[1-\Big(\frac{\mathrm{V}}{\mathrm{V}_0}\Big)^{\frac{1}{3}}\Big]\exp\Big\{\frac{3}{2}(\mathrm{K}_0'-1)\times\Big[1-\Big(\frac{\mathrm{V}}{\mathrm{V}_0}\Big)^{\frac{1}{3}}\Big]\Big\}. \tag{B.2}$$

B.0.3 Clausius-Clapeyron relation

In case of transition between two phases, the Clausius-Clapeyron relation is a way to relate the slope of a coexistence curve in the pressure-temperature diagram to the variation of volume and entropy that occur in the transition. In case of transition between a solid and a liquid phase the coexistence curve is the melting curve and the variation of volume and entropy are the melting volume $\Delta\mathrm{V_m} = \mathrm{V_L} - \mathrm{V_S}$ and the melting entropy $\Delta\mathrm{S_m} = \mathrm{S_L} - \mathrm{S_S}$ [124].

The equilibrium between solid and liquid along the coexistence curve can be expressed imposing the total differential change in Gibbs energy to zero:

$$\mathrm{dG} = (\mathrm{V_L} - \mathrm{V_S})\mathrm{dP} - (\mathrm{S_L} - \mathrm{S_S})\mathrm{dT} = 0.$$

The Clausius-Clapeyron relation is:

$$\frac{\mathrm{dT_m}}{\mathrm{dP}} = \frac{\Delta\mathrm{V_m}}{\Delta\mathrm{S_m}} \tag{B.3}$$

The melting entropy is generally positive, since the liquid is more disordered than the solid, which means that some energy has to be absorbed by the system in the phase transition. In case of negative melting slope the melting volume is then nega-

tive, meaning that the liquid is denser than the solid.

The importance of the Clausius-Clapeyron relation is that it allows to give a thermodynamic description of a system starting from parameters that can be experimentally measured such as the melting volume and the slope of the melting curve.

List of Abbreviations

AIMD	Ab-initio Molecular Dynamics
BSE	Bethe-Salpeter Equation
CNA	Common-Neighbour Analysis
DAC	Diamond Anvil Cell
DICOS	Distorted Icosahedral Structures
DOS	Density of States
DFT	Density Functional Theory
EBS	Extremely Brilliant Source
EDS	Energy Dispersive Spectrometry
EDXAS	Energy Dispersive X-ray Absorption Spectroscopy
EOS	Equation of State
EXAFS	Extended X-ray Absorption Fine Structure
FIB	Focused Ion Beam
FWHM	Full Width Half Maximum
ICB	Inner Core Boundary
ISRO	Icosahedral Short Range Order
LH-DAC	Laser Heated Diamond Anvil Cell
LDS	Liquid Diffuse Scattering
MCB	Mantle Core Boundary
MD	Molecular Dynamics
NBSE	NIST core-level Bethe-Salpeter Equation
NPD	Nano-polycrystalline Diamond
OCEAN	Obtaining Core Excitations from *Ab-initio* electronic structure and NBSE

PDOS	Projected Density of States
PREM	Preliminary Reference Earth Model
PTM	Pressure Transmitting Medium
QMD	Quantum Molecular Dynamics
RDF	Radial Distribution Function
RH-LVP	Resistively Heated Large Volume Press
RMC	Reverse Monte Carlo
SEM	Scanning Electron Microscopy
SRO	Shord Range Order
XRD	X-ray Diffraction
XANES	X-ray Absorption Near Edge Structure
XAS	X-ray Absorption Spectroscopy

Bibliography

[1] https://en.wikipedia.org/wiki/Kola_Superdeep_Borehole, accessed October 2017.

[2] D. Alfè, M. J. Gillan, and G. D. Price. Temperature and composition of the Earth's core. *Contemp. Phys.*, 48(2):63–80, 2007.

[3] D Alfè, L Vocadlo, G D Price, and M J Gillan. Melting curve of materials : theory versus experiments. *Journal of Physics: Condensed Matter*, 16:S973–S982, 2004.

[4] Claude J. Allègre, Jean-Paul Poirier, Eric Humler, and Albrecht W. Hofmann. The Chemical Composition of the Interior Shells of the Earth. *Earth and Planetary Science Letters*, 134:515–526, 1995.

[5] O. L. Anderson. *Theory of the Earth*. Blackwell Scientific Publications, 1989.

[6] William W Anderson and Thomas J Ahrens. An equation of state for liquid iron and implications for the Earth's core. *Journal of Geophysical Research*, 99(B3):4273–4284, 1994.

[7] Denis Andrault, Julien Monteux, Michael Le, and Henri Samuel. The deep Earth may not be cooling down. *Earth and Planetary Science Letters*, 443:195–203, 2016.

[8] Daniele Antonangeli, Julien Siebert, James Badro, Daniel L Farber, Guillaume Fiquet, Guillaume Morard, and Frederick J Ryerson. Composition of the Earth's inner core from high-pressure sound velocity measurements in Fe – Ni – Si alloys. *Earth and Planetary Science Letters*, 295(1-2):292–296, 2010.

[9] S Anzellini, A Dewaele, M Mezouar, P Loubeyre, and G Morard. Melting of iron at Earth's inner core boundary based on fast X-ray diffraction. *Science*, 340(6131):464–6, 2013.

[10] Simone Anzellini. *Phase diagram of iron under wxtreme conditions measured with time-resolved methods*. PhD thesis, Université Pierre et Marie Curie, 2014.

[11] Giuliana Aquilanti, Angela Trapananti, Amol Karandikar, Innokenty Kantor, Carlo Marini, Olivier Mathon, Sakura Pascarelli, and Reinhard Boehler. Melting of iron determined by x-ray absorption spectroscopy to 100 gpa. *Proceedings of the National Academy of Sciences*, 112(39):12042–12045, 2015.

[12] Matthew M. Armentrout and Abby Kavner. A new high pressure and temperature equation of state of fcc cobalt. *Journal of Applied Physics*, 118(19), 2015.

[13] N. W. Ashcroft and J. Lekner. Structure and Resistivity of Liquid Metals. *Physical Review*, 145:83, 1966.

[14] J. Badro, A. S. Cote, and John P. Brodholt. A seismologically consistent compositional model of Earth's core. *Proceedings of the National Academy of Sciences*, 111(21):7542–7545, 2014.

[15] A B Belonoshko, S Davis, A Rosengren, R Ahuja, B Johansson, S I Simak, L Burakovsky, and D L Preston. Xenon melting : Density functional theory versus diamond anvil cell experiments. *Physical Review B*, 74:054114, 2006.

[16] L Benedetti and P Loubeyre. Temperature gradients, wavelength-dependent emissivity, and accuracy of high and very-high temperatures measured in the laser-heated diamond cell. *High Pressure Research*, 24(4):423–445, 2004.

[17] R E Benfield, A Filipponi, D T Bowron, R J Newport, and S J Gurman. X-ray absorption study of gold coordination compounds: EXAFS refinements and double-electron excitation background . *Journal of Physics: Condensed Matter*, 6:8429, 1994.

[18] J. D. Bernal. The structure of liquids. *Proceedings of the Royal Society of London A: Mathematical, Physical and Engineering Sciences*, 280:299, 1964.

[19] Chandrani Bhattacharya, M K Srivastava, and S V G Menon. Melting curves of FCC-metals by cell-theory. *Physica B: Physics of Condensed Matter*, 406(21):4035–4040, 2011.

[20] Francis Birch. Elasticity and constitution of the Earth's interior. *Journal of Geophysical Research*, 57(2):227–286, 1952.

[21] Silvia Boccato, Andrea Sanson, Innokenty Kantor, Olivier Mathon, Vadim Dyadkin, Dmitry Chernyshov, Alberto Carnera, and Sakura Pascarelli. Thermal and magnetic anomalies of α -iron : an exploration by extended x-ray absorption fine structure spectroscopy and synchrotron x-ray diffraction. *Journal of Physics: Condensed Matter*, 28:355401, 2016.

[22] Silvia Boccato, Raffaella Torchio, Innokenty Kantor, Guillaume Morard, Simone Anzellini, Ruggero Giampaoli, Richard Briggs, Alessandro Smareglia, Tetsuo Ir-

ifune, and Sakura Pascarelli. The Melting Curve of Nickel Up to 100 GPa Explored by XAS. *Journal of Geophysical Research: Solid Earth*, 122:1–10, 2017.

[23] R Boehler, H G Musshoff, R Ditz, G Aquilanti, A Trapananti, R Boehler, H G Musshoff, R Ditz, G Aquilanti, A Trapananti, and I I Laser-heating System. Portable laser-heating stand for synchrotron applications. *Review of Scientific Instruments*, 80:045103, 2009.

[24] R. Boehler, D. Santamaría-Pérez, D. Errandonea, and M. Mezouar. Melting , density , and anisotropy of iron at core conditions : new X-ray measurements to 150 GPa. *Journal of physics: Conference Series*, 121(022018), 2008.

[25] Reinhard Boehler. Temperatures in the Earth's core from melting-point measurements of iron at high static pressures. *Nature*, 363(6429):534–536, 1993.

[26] Reinhard Boehler and Koen De Hantsetters. New anvil designs in diamond-cells. *High Pressure Research*, 24(3):391–396, 2004.

[27] Martin Brehm and Barbara Kirchner. Travis - a free analyzer and visualizer for monte carlo and molecular dynamics trajectories. *Journal of Chemical Information and Modeling*, 51(8):2007–2023, 2011.

[28] Robin Brett. The Current Status of Speculations on the Composition of the Core of the Earth. 14(3), 1976.

[29] J Michael Brown and Rober G McQueen. Phase Transitions, Gruneisen Parameter, and Elasticity for Shocked Iron Between 77 GPa and 400 GPa. *Journal of Geophysical Research*, 91(B7):7485–7494, 1986.

[30] Bruce A Buffett. Earth's Core and the Geodynamo. *Science*, 288:2007–2013, 2000.

[31] Grant Bunker. *Introduction to XAFS. A Practical Guide to X-ray Absorption Fine Structure Spectroscopy*. Cambridge University Press, 2010.

[32] Qi-Long Cao, Pan-Pan Wang, Duo-Hui Huang, Jun-Sheng Yang, Ming-Jie Wan, and Fan-Hou Wang. Properties of Liquid Nickel along Melting Lines under High Pressure. *Chinese Physics Letters*, 32(8):086201, 2015.

[33] Jiuhua Chen, Tony Yu, Shu Huang, Jennifer Girard, and Xiaoyang Liu. Compressibility of liquid FeS measured using X-ray radiograph imaging. *Physics of the Earth and Planetary Interiors*, 228:294–299, 2014.

[34] P. D'Angelo, A. Di Nola, A. Filipponi, N. V. Pavel, and D. Roccatano. An extended x-ray absorption fine structure study of aqueous solutions by employing molecular dynamics simulations. *The Journal of Chemical Physics*, 100(2):985, 1994.

[35] Agnès Dewaele and Paul Loubeyre. Pressurizing conditions in helium-pressure- transmitting medium. *High Pressure Research*, 27(4):419–429, 2007.

[36] Agnès Dewaele, Paul Loubeyre, and Mohamed Mezouar. Equations of state of six metals above 94 GPa. 094112:1–8, 2004.

[37] Agnès Dewaele, Mohamed Mezouar, Nicolas Guignot, and Paul Loubeyre. Melting of lead under high pressure studied using second-scale time-resolved x-ray diffraction. *Physical Review B - Condensed Matter and Materials Physics*, 76(14):1–5, 2007.

[38] Agnès Dewaele, Mohamed Mezouar, Nicolas Guignot, and Paul Loubeyre. High melting points of tantalum in a laser-heated diamond anvil cell. *Physical Review Letters*, 104(25):29–31, 2010.

[39] Agnès Dewaele and Chrystèle Sanloup. *L'intérieur de la Terre et des planètes*. Belin, 2005.

[40] Agnès Dewaele, Marc Torrent, Paul Loubeyre, and Mohamed Mezouar. *Physical Review B - Condensed Matter and Materials Physics*, 78(10):1–13, 2008.

[41] A. Di Cicco, F. Iesari, S. De Panfilis, M. Celino, S. Giusepponi, and A. Filipponi. Local fivefold symmetry in liquid and undercooled ni probed by x-ray absorption spectroscopy and computer simulations. *Phys. Rev. B*, 89:060102, 2014.

[42] Andrea Di Cicco. Phase Transitions in Confined Gallium Droplets. *Physical review letters*, 81(14):2942–2945, 1998.

[43] Andrea Di Cicco and Angela Trapananti. Study of local icosahedral ordering in liquid and undercooled liquid copper. *Journal of Non-Crystalline Solids*, 353(32-40):3671–3678, 2007.

[44] Andrea Di Cicco, Angela Trapananti, Emiliano Principi, Simone De Panfilis, and Adriano Filipponi. Polymorphism and metastable phenomena in liquid tin under pressure. *Applied Physics Letters*, 89(221912):1–3, 2006.

[45] V Dose, R Drube, and A Hartl. Empty electronic states in solid and liquid nickel. *Solid State Communications*, 57(4):273–275, 1986.

[46] D J Dunstan. Theory of the gasket in diamond anvil high-pressure cells. *Review of Scientific Instruments*, 60(12):3789–3795, 1989.

[47] A. M. Dziewonski and D. L. Anderson. *Physics of the Earth and Planetary Interiors*, 25:297, 1981.

[48] Almax easyLab. `http://www.almax-easylab.com`, accessed July 2017.

[49] T Egami. Icosahedral order in liquids. *Journal of Non-Crystalline Solids*, 353:3666–3670, 2007.

[50] D. Errandonea. High-pressure melting curves of the transition metals Cu, Ni, Pd, and Pt. *Physical Review B - Condensed Matter and Materials Physics*, 87(5):1–5, 2013.

[51] Daniel Errandonea, Beate Schwager, Reiner Ditz, Christine Gessmann, Reinhard Boehler, and Marvin Ross. Systematics of transition-metal melting. *Physical Review B*, 63(13):132104, 2001.

[52] A Filipponi, M Borowski, P W Loeffen, S De Panfilis, A Di Cicco, F Sperandini, M Minicucci, and M Giorgetti. Single-energy x-ray absorption detection : a combined electronic and structural local probe for phase transitions in condensed matter. *Journal of physics. Condensed matter*, 10:235–253, 1998.

[53] A. Filipponi and A. Di Cicco. Short-range order in crystalline, amorphous, liquid, and supercooled germanium probed by x-ray-absorption spectroscopy. *Physical Review B*, 51(18):12322–12336, 1995.

[54] A. Filipponi and A. Di Cicco. Short-range order in crystalline, amorphous, liquid, and supercooled germanium probed by x-ray-absorption spectroscopy. *Physical Review B*, 51(18):12322–12336, 1995.

[55] Adriano Filipponi. EXAFS for liquids. *Journal of Physics: Condensed Matter*, 13(7):R23, 2001.

[56] Adriano Filipponi, Adrea Di Cicco, Angela Trapananti, Emiliano Principi, Marco Minicucci, and Agnieszka Witkowska. Gnxas. July 2009.

[57] Adriano Filipponi, Andrea Di Cicco, and Simone De Panfilis. Structure of Undercooled Liquid Pd Probed by X-Ray Absorption Spectroscopy. *Physical Review Letters*, 83(3):560–563, 1999.

[58] J. L. Finney. Random packings and the structure of simple liquids: I . The geometry of random close packing. *Proceedings of the Royal Society of London A: Mathematical, Physical and Engineering Sciences*, 319:479–493, 1970.

[59] Rebecca A. Fischer. In Jidenori Terasaki and Rebecca A. Fischer, editors, *Deep Earth: Physics and Chemistry of the Lower Mantle and Core*, chapter Melting of Fe Alloys and the Thermal Structure of the Core, pages 3–12. Wiley, Hoboken, New Jersey, 2016.

[60] Dipartimento Fisica, Universith Aquila, and L Aquila. Double-electron excitation effects above inner shell X-ray absorption edges Filipponi. *Physica B*, 209:29–32, 1995.

[61] Richard A. Forman, Gasper J. Piermarini, J. Dean Barnett, and Stanley Block. Pressure Measurement Made by the Utilization of Ruby Sharp-Line Luminescence. *Science*, 176:284, 1972.

[62] Paolo Fornasini. In S. Mobilio and G. Vlaic, editors, *Synchrotron Radiation: Fundamentals, Methodologies and Applications*, chapter Introduction to X-ray absorption spectroscopy, pages 129–170. Conference Proceedings, Bologna, 2003.

[63] Paolo Fornasini. Introduction to X-ray absorption spectroscopy. *XI School on Synchrotron Radiation*, pages 1–32, 2011.

[64] F. C. Frank. A discussion on theory of liquids - supercooling of liquids. *Proceedings of the Royal Society of London A: Mathematical, Physical and Engineering Sciences*, 215(1120):43–46, 1952.

[65] Zachary M. Geballe and Raymond Jeanloz. Origin of temperature plateaus in laser-heated diamond anvil cell experiments. *Journal of Applied Physics*, 111(12), 2012.

[66] Ruggero Giampaoli. Temperature measurements at megabar pressures: direct comparison between reflective and refractive optics for the laser heated diamond anvil cell, 2017.

[67] Ruggero Giampaoli et al. in preparation.

[68] K Gilmore, John Vinson, E L Shirley, D Prendergast, C D Pemmaraju, J J Kas, F D Vila, and J J Rehr. Efficient implementation of core-excitation Bethe – Salpeter equation calculations. *Computer Physics Communications*, 197:109–117, 2015.

[69] Alexander F Goncharov, Joseph M Zaug, Jonathan C Crowhursteugene Gregoryanz, Alexander F Goncharov, Joseph M Zaug, Jonathan C Crowhurst, and Eugene Gregoryanz. Optical calibration of pressure sensors for high pressures and temperatures Optical calibration of pressure sensors for high pressures and temperatures. *Journal of Applied Physics*, 97:094917, 2005.

[70] Eugene Gregoryanz, Olga Degtyareva, Maddury Somayazulu, Russell J Hemley, and Ho-kwang Mao. Melting of Dense Sodium. 185502(May):1–4, 2005.

[71] Helmut Hermann, Antje Elsner, and Dietrich Stoyan. Behavior of icosahedral clusters in computer simulated hard sphere systems. *Journal of Non-Crystalline Solids*, 353:3693–3697, 2007.

[72] Kei Hirose, Staphane Labrosse, and John Hernlund. Composition and State of the Core. *Annual Review of Earth and Planetary Sciences*, 41(1):657–691, 2013.

[73] Takamichi Iida and Roderick I. L. Guthrie. *Fundamentals*, volume 1 of *The Thermophysical Properties of Metallic Liquids*. Oxford University Press, 1 edition, 2015.

[74] Tetsuo Irifune, Ayako Kurio, Shizue Sakamoto, Toru Inoue, and Hitoshi Sumiya. Ultrahard polycrystalline diamond from graphite. *Nature Publishing Group*, 421(February):600, 2003.

[75] Naoki Ishimatsu, Ken Matsumoto, Hiroshi Maruyama, Naomi Kawamura, Masaichiro Mizumaki, Hitoshi Sumiya, and Tetsuo Irifune. Glitch-free X-ray absorption spectrum under high pressure obtained using nano-polycrystalline diamond anvils. *Journal of Synchrotron Radiation*, 19(5):768–772, 2012.

[76] Noel Jakse and Alain Pasturel. Ab initio molecular dynamics simulations of local structure of supercooled Ni. *The Journal of chemical physics*, 120(13):6124–6127, 2004.

[77] Noël Jakse and Alain Pasturel. Molecular-dynamics study of liquid nickel above and below the melting point. *The Journal of chemical physics*, 123(24):244512, 2005.

[78] Stefanie Japel, Beate Schwager, Reinhard Boehler, and Marvin Ross. Melting of copper and nickel at high pressure: The role of d electrons. *Physical Review Letters*, 95(16):1–4, 2005.

[79] Raymond Jeanloz and S. Morris. Temperature distribution in the crust and mantle. *Annual Review of Earth and Planetary Sciences*, 14:377–415, 1986.

[80] Raymond Jeanloz and Frank M Richter. Convection , Composition , and the Thermal State of the Lower Mantle. *Journal of Geophysical Research*, 84(9):5497, 1979.

[81] I Kantor, C Marini, O Mathon, and S Pascarelli. A laser heating facility for energy-dispersive X-ray absorption spectroscopy. *Review of Scientific Instruments*, 89(013111):1–13, 2018.

[82] Innokenty Kantor, Jean-Claude Labiche, Emmanuel Collet, Laurent Siron, Jean-Jacques Thevenin, Cyril Ponchut, Jacques Borrel, Trevor Mairs, Carlo Marini, Cornelius Strohm, Olivier Mathon, and Sakura Pascarelli. A new detector for sub-millisecond EXAFS spectroscopy at the European Synchrotron Radiation Facility. *Journal of Synchrotron Radiation*, 21(6):1240–1246, 2014.

[83] Amol Karandikar and Reinhard Boehler. Flash melting of tantalum in a diamond cell to 85 GPa. *Physical Review B*, 93(054107):1–6, 2016.

[84] Abby Kavner and Wendy R Panero. Temperature gradients and evaluation of thermoelastic properties in the synchrotron-based laser-heated diamond cell. *Physics of the Earth and Planetary Interiors*, 143-144:527–539, 2004.

[85] S N Khanna and F Cyrot-Lackmann. Density of electronic states in liquid Ni. *Philosophical Magazine B*, 38(2):197–203, 1978.

[86] S N Khanna, F Cyrot-Lackmann, and M C Desjonquères. Density of electronic states in amorphous and liquid cobalt. *Journal of Physics F: Metal Physics*, 9(1):79, 1979.

[87] S Klotz, J-C Chervin, P Munsch, and G Le Marchand. Hydrostatic limits of 11 pressure. *Journal of Physics D: Applied Physics*, 42:075413, 2009.

[88] L. Koči, E M Bringa, D S Ivanov, J Hawreliak, J. McNaney, A Higginbotham, L V Zhigilei, A B Belonoshko, B A Remington, and R Ahuja. Simulation of shock-induced melting of Ni using molecular dynamics coupled to a two-temperature model. *Physical Review B - Condensed Matter and Materials Physics*, 74(1):2–5, 2006.

[89] Tetsuya Komabayashi and Yingwei Fei. Internally consistent thermodynamic database for iron to the Earth's core conditions. *Journal of Geophysical Research: Solid Earth*, 115(3):1–12, 2010.

[90] Yasuhiro Kuwayama, Kei Hirose, Nagayoshi Sata, and Yasuo Ohishi. Phase relations of iron and iron-nickel alloys up to 300 GPa: Implications for composition and structure of the Earth's inner core. *Earth and Planetary Science Letters*, 273(3-4):379–385, 2008.

[91] Stephane Labrosse. In Jidenori Terasaki and Rebecca A. Fischer, editors, *Deep Earth: Physics and Chemistry of the Lower Mantle and Core*, chapter Thermal State and Evolution of the Earth Core and Deep Mantle, pages 43–54. Wiley, Hoboken, New Jersey, 2016.

[92] P. Lazor, G. Shen, and S. K. Saxena. Laser-heated diamond anvil cell experiments at high pressure: Melting curve of nickel up to 700 kbar. *Physics and Chemistry of Minerals*, 20(2):86–90, 1993.

[93] Peter Lazor. *Phase Diagrams, Elasticity and Thermodynamics of Ni, Co and Fe under High Pressure*. PhD thesis, Faculty of Science and Technology, 1994.

[94] Byeongchan Lee and Geun Woo Lee. A liquid-liquid transition can exist in monatomic transition metals with a positive melting slope. *Scientific Reports*, (6):35564, 2016.

[95] G. W. Lee, A. K. Gangopadhyay, K. F. Kelton, R. W. Hyers, T. J. Rathz, J. R. Rogers, and D. S. Robinson. Difference in icosahedral short-range order in early and late transition metal liquids. *Physical Review Letters*, 93(3):037802–1, 2004.

[96] R Letoullec, J P Pinceaux, and P Loubeyre. The membrane diamond anvil cell: A new device for generating continuous pressure and temperature variations. *High Pressure Research*, 1:77–90, 1988.

[97] J. Li and C. B. Agee. The effect of pressure, temperature, oxygen fugacity and composition on partitioning of nickel and cobalt between liquid Fe-Ni-S alloy and liquid silicate: Implications for the Earth's core formation. *Geochimica et Cosmochimica Acta*, 65(11):1821–1832, 2001.

[98] Lin-gun Liu. Speculations on the composition and origin of the earth. *Geochemical Journal*, 16:287–310, 1982.

[99] Yin Liyuan. Research on First-principles Calculations of the Pressure-induce Structure of Liquid Cobalt at High Temperature. *Natural Science Journal of Harbin Normal University*, 2011.

[100] Oliver T. Lord, Ian G. Wood, David P. Dobson, Lidunka Vocadlo, Weiwei Wang, Andrew R. Thomson, Elizabeth T. H. Wann, Guillaume Morard, Mohamed Mezouar, and Michael J. Walter. The melting curve of Ni to 1 Mbar. *Earth and Planetary Science Letters*, 408:226–236, 2014.

[101] Hans Lueth. *Solid Surfaces, Interfaces and Thin Films*. Springer, fifth edition, 2010.

[102] Fen Luo, Xiang Rong Chen, Ling Cang Cai, and Guang Fu Ji. Solid-liquid interfacial energy and melting properties of nickel under pressure from molecular dynamics. *Journal of Chemical and Engineering Data*, 55(11):5149–5155, 2010.

[103] Jianbo Ma, Yongbing Dai, Jiao Zhang, Zhenlei Zhang, Jun Wang, and Baode Sun. Ab initio molecular dynamics study of the structure of undercooled Ni melt. *Journal of Non-Crystalline Solids*, 376:216–220, 2013.

[104] H. K. Mao. In P. L. A. Polian and N. Boccara, editors, *Simple molecular systems at very high density*, chapter Static compression of simple molecular systems in the megabar range, pages 221–236. Plenum Press, New York, 1989.

[105] C. Marini, F. Occelli, O. Mathon, R. Torchio, V. Recoules, S. Pascarelli, and P. Loubeyre. A microsecond time resolved x-ray absorption near edge structure synchrotron study of phase transitions in Fe undergoing ramp heating at high pressure. *Journal of Applied Physics*, 115(9):1–5, 2014.

[106] J. Mathon and A. Umerski. *Physics of low dimentional sysyems*. ed by J. Moran-Lopez (Kluwer/Plenum), New York, 2001.

[107] S. Mazevet, V. Recoules, J. Bouchet, F. Guyot, M. Harmand, A. Ravasio, and A. Benuzzi-Mounaix. Ab initio calculation of x-ray absorption of iron up to 3 Mbar and 8000 K. *Physical Review B - Condensed Matter and Materials Physics*, 89(10):1–5, 2014.

[108] W. F. McDonough and S. s. Sun. The composition of the Earth. *Chemical Geology*, 120(3-4):223–253, 1995.

[109] R. G. McQueen and S. P. Marsh. Shock-Wave Compression of Iron-Nickel Alloys and the Earth's Core. *Journal of Geophysical Research*, 71(6):1751, 1966.

[110] Ronald T. Merril and Michael W. McElhinny. *The Earth's Magnetic Field: It's History, Origin and Planetary Perspective*. Academic, New York, 1983.

[111] M. Mezouar, W. A. Crichton, S. Bauchau, F. Thurel, H. Witsch, F. Torrecillas, G. Blattmann, P. Marion, Y. Dabin, J. Chavanne, O. Hignette, C. Morawe, and C. Borel. Development of a new state-of-the-art beamline optimized for monochromatic single-crystal and powder X-ray diffraction under extreme conditions at the ESRF. *Journal of Synchrotron Radiation*, 12(5):659–664, 2005.

[112] D V Minakov. Melting curves of metals with excited electrons in the quasiharmonic approximation. 224102:1–10, 2015.

[113] G. Morard, D. Andrault, D. Antonangeli, Y. Nakajima, A.L. Auzende, E. Boulard, S. Cervera, A. Clark, O.T. Lord, J. Siebert, V. Svitlyk, G. Garbarino, and M. Mezouar. Fe-feo and fe-fe3c melting relations at earth's core – mantle boundary conditions: Implications for a volatile-rich or oxygen-rich core. *Earth and Planetary Science Letters*, 473:94–103, 2017.

[114] G Morard, J Siebert, D Andrault, N Guignot, and G Garbarino. The Earth ' s core composition from high pressure density measurements of liquid iron alloys. *Earth and Planetary Science Letters*, 373:169–178, 2013.

[115] Guillaume Morard et al. *in preparation*.

[116] C. R. Natoli and M. Benfatto. A unifying scheme of interpretation of X-ray absorption spectra based on the multiple scattering theory. *Journal de Physique*, Colloque C8(47):11–23, 1986.

[117] K Nishida, E Ohtani, S Urakawa, A Suzuki, T Sakamaki, H Terasaki, and Y Katayama. Density measurement of liquid FeS at high pressures using synchrotron X-ray absorption X-ray. *American Mineralogist*, 96:864–868, 2011.

[118] Akifumi Onodera, Kaichi Suito, and Yasuhire Morigami. High-Pressure Synthesis of Diamond from Organic Compounds. *Proc. Japan Acad.*, 68B(10):167–171, 1992.

[119] Paolo M. Ossi. *Disordered Materials, an introduction*. Springer, second edition, 2006.

[120] S. Pascarelli, O. Mathon, T. Mairs, I. Kantor, G. Agostini, C. Strohm, S. Pasternak, F. Perrin, G. Berruyer, P. Chappelet, C. Clavel, and M. C. Dominguez. The Time-resolved and Extreme-conditions XAS (TEXAS) facility at the European Synchrotron Radiation Facility: the energy-dispersive X-ray absorption

spectroscopy beamline ID24. *Journal of Synchrotron Radiation*, 23(1):353–368, 2016.

[121] S. Pascarelli, O. Mathon, M. Munõz, T. Mairs, and J. Susini. Energy-dispersive absorption spectroscopy for hard-X-ray micro-XAS applications. *Journal of Synchrotron Radiation*, 13(5):351–358, 2006.

[122] W Pepperhof and M Acet. *Constitution and Magnetism of Iron and its Alloys*. Springer, 2001.

[123] G J Piermarini, S Block, and J D Barnett. Hydrostatic limits in liquids and solids to 100 kbar. *Journal of Applied Physics*, 44(12):5377, 1973.

[124] Jean-Paul Poirier. Light elements in the Earth's outer core : A critical review. *Physics of the Earth and Planetary Interiors*, 85(94):319–337, 1994.

[125] Jean-Paul Poirier. *Introduction to the Physics of the Earth's Interior*. Cambridge University Press, 2003.

[126] R Poloni, S De Panfilis, A Di Cicco, G Pratesi, E Principi, A Trapananti, and A Filipponi. Liquid gallium in confined droplets under high-temperature and high-pressure conditions. *Physical Review B*, 71(184111):1–8, 2005.

[127] Monica Pozzo and Dario Alfé. Melting curve of face-centered-cubic nickel from first-principles calculations. *Physical Review B*, 88:024111, 2013.

[128] E Principi, M Minicucci, A Di Cicco, A Trapananti, S De Panfilis, and R Poloni. Metastable phase diagram of Bi probed by single-energy x-ray absorption detection and angular dispersive x-ray diffraction. *Physical Review B*, 74(064101):1–7, 2006.

[129] A. T. Raji, S. Scandolo, M. Härting, and D. T. Britton. Probing the structure of iron at extreme conditions by X-ray absorption near-edge structure calculations. *High Pressure Research*, 33(1):119–123, 2013.

[130] A.T. Raji and S. Scandolo. Theoretical x-ray absorption near-edge structure signatures of solid and liquid phases of iron at extreme conditions. *High Pressure Research*, 34(2):250–258, 2014.

[131] J.J. Rehr, J.J. Kas, F.D. Vila, M.P. Prange, and K. Jorissen. *Phys. Chem*, 12:5503, 2010.

[132] Alberto Riva. Expanding the accessible p/t domain of the paris-edinburgh-press, a versatile tool to study liquid network structures at extreme p/t conditions, 2017.

[133] Marvin Ross, Reinhard Boehler, and Daniel Errandonea. Melting of transition metals at high pressure and the influence of liquid frustration : The late metals Cu , Ni , and Fe. *Physical Review B*, 76(184117):1–7, 2007.

[134] Marvin Ross, Daniel Errandonea, and Reinhard Boehler. Melting of transition metals at high pressure and the influence of liquid frustration : The early metals Ta and Mo. *Physical Review B*, 76(184118):1–6, 2007.

[135] Marvin Ross, Lin H. Yang, and Reinhard Boehler. Melting of aluminum, molybdenum, and the light actinides. *Physical Review B - Condensed Matter and Materials Physics*, 70(18):1–8, 2004.

[136] C Sanloup, G Fiquet, E Gregoryanz, G Morard, and M Mezouar. Effect of Si on liquid Fe compressibility : Implications for sound velocity in core materials. *Geophysical Research Letters*, 31(L07604):1–4, 2004.

[137] C Sanloup, F Guyot, P Gillet, G Fiquet, R J Hemley, M Mezouar, and I Martinez. Structural changes in liquid Fe at high pressures and high temperatures from synchrotron X-ray diffraction. *Europhys. Lett.*, 52(2):151–157, 2000.

[138] C Sanloup, F Guyot, P Gillet, G Fiquet, M Mezouar, and I Martinez. Density measurements of liquid Fe-S alloys at high-pressure. *Geophysical Research Letters*, 27(6):811–814, 2000.

[139] C Sanloup, W Van Westrenen, R Dasgupta, H Maynard-casely, and J Perrillat. Compressibility change in iron-rich melt and implications for core formation models. *Earth and Planetary Science Letters*, 306:118–122, 2011.

[140] T. Schenk, D. Holland-Moritz, V. Simonet, R. Bellissent, and D. M. Herlach. Icosahedral short-range order in deeply undercooled metallic melts. *Physical Review Letters*, 89(7):075507–1–075507–2, 2002.

[141] Guoyin Shen, Vitali B Prakapenka, Mark L Rivers, and Stephen R Sutton. Structure of liquid iron at pressures up to 58 GPa. *Physical Review Letters*, 92(18):185701–1, 2004.

[142] Yuta Shimoyama, Hidenori Terasaki, Eiji Ohtani, Satoru Urakawa, Yusaku Takubo, Keisuke Nishida, Akio Suzuki, and Yoshinori Katayama. Density of Fe-3.5 wt % C liquid at high pressure and temperature and the effect of carbon on the density of the molten iron. *Physics of the Earth and Planetary Interiors*, 224:77–82, 2013.

[143] Eric L Shirley. Bethe – Salpeter treatment of X-ray absorption including core-hole multiplet effects. *Journal of Electron Spectroscopy and Related Phenomena*, 144-147:1187–1190, 2005.

[144] Franz Simon and Gunther Glatzel. Bemerkungen zur Schmelzdruckkurve. *Zeitschrift für Anorganische und Allgemeine Chemie*, 178:309–316, 1929.

[145] Ryosuke Sinmyo and Kei Hirose. The Soret diffusion in laser-heated diamond-anvil cell. *Physics of the Earth and Planetary Interiors*, 180(3-4):172–178, 2010.

[146] A. V. Soldatov. X-ray Absorption Near Edge Structure as a Source of Structural Information. *Journal of Chemistry*, 49:102–106, 2008.

[147] D J Stevenson. Models of the Earth's Core. *Science (New York, N.Y.)*, 214(4521):611–9, 1981.

[148] Shigehiko Tateno, Kei Hirose, Tetsuya Komabayashi, Haruka Ozawa, and Yasuo Ohishi. The structure of Fe-Ni alloy in Earth's inner core. *Geophysical Research Letters*, 39(12):2–5, 2012.

[149] Shigehiko Tateno, Kei Hirose, Yasuo Ohishi, and Yoshiyuki Tatsumi. The structure of iron in Earth's inner core. *Science*, 330:359–361, 2010.

[150] Shigehiko Tateno, Yasuhiro Kuwayama, Kei Hirose, and Yasuo Ohishi. The structure of Fe-Si alloy in Earth's inner core. *Earth and Planetary Science Letters*, 418:11–19, 2015.

[151] H Terasaki, K Nishida, Y Shibazaki, T Sakamaki, A Suzuki, E Ohtani, and T Kikegawa. Density measurement of Fe3C liquid using X-ray absorption image up to 10 GPa and effect of light elements on compressibility of liquid iron. *Journal of Geophysical Research*, 115(B06207):1–7, 2010.

[152] Hidenori Terasaki. In Jidenori Terasaki and Rebecca A. Fischer, editors, *Deep Earth: Physics and Chemistry of the Lower Mantle and Core*, chapter Physical Properties of the Outer Core, pages 129–142. Wiley, Hoboken, New Jersey, 2016.

[153] R Torchio, S Boccato, V Cerantola, G Morard, T Irifune, and I Kantor. Probing the local, electronic and magnetic structure of matter under extreme conditions of temperature and pressure. *High Press. Res.*, 36(3):293–302, 2016.

[154] R Torchio, Y O Kvashnin, S Pascarelli, O Mathon, C Marini, L Genovese, P Bruno, G Garbarino, A Dewaele, F Occelli, and P Loubeyre. X-Ray Magnetic Circular Dichroism Measurements in Ni up to 200 GPa : Resistant Ferromagnetism. *Physical Review Letters*, 107(237202):1–5, 2011.

[155] Raffaella Torchio. *Magnetism structure and chemical order in the 3d metals and their alloys at extreme pressures*. PhD thesis, Universitá degli Studi Roma Tre, 2012.

[156] Raffaella Torchio, A. Monza, F. Baudelet, Sakura Pascarelli, Olivier Mathon, E. Pugh, Daniele Antonangeli, and J. Paul Itié. Pressure-induced collapse of ferromagnetism in cobalt up to 120 GPa as seen via x-ray magnetic circular dichroism. *Physical Review B - Condensed Matter and Materials Physics*, 84(6):5–8, 2011.

[157] Raffaella Torchio, Florent Occelli, Olivier Mathon, Arnaud Sollier, Emilien Lescoute, Laurent Videau, Tommaso Vinci, Alessandra Benuzzi-mounaix, Jon Headspith, William Helsby, Simon Bland, Daniel Eakins, David Chapman, Sakura Pascarelli, and Paul Loubeyre. Probing local and electronic structure in Warm Dense Matter : single pulse synchrotron x-ray absorption spectroscopy on shocked Fe. *Scientific Reports*, 6(June):26402, 2016.

[158] Angela Trapananti, Andrea Di Cicco, and Marco Minicucci. Structural disorder in liquid and solid CuI at high temperature probed by x-ray absorption spectroscopy. *Physical Review B*, 66(014202):1–11, 2002.

[159] Taku Tsuchiya, Kenji Kawai, Xianlong Wang, Hiroki Ichikawa, and Haruhiko Dekura. In Jidenori Terasaki and Rebecca A. Fischer, editors, *Deep Earth: Physics and Chemistry of the Lower Mantle and Core*, chapter Temperature of the Lower Mantle and Core Based on Ab Initio Mineral Physics Data, pages 13–30. Wiley, Hoboken, New Jersey, 2016.

[160] D. Turnbull and R. E. Cech. Microscopic observation of the solidification of small metal droplets. *Journal of Applied Physics*, 21(8):804–810, 1950.

[161] Pascal Vinet, John Ferrante, James H. Rose, and John R. Smith. Compressibility of solids. *Journal of Geophysical Research*, 92:9319–9325, 1987.

[162] J Vinson, J J Rehr, J J Kas, and E L Shirley. Bethe-Salpeter equation calculations of core excitation spectra. 115106, 2011.

[163] Michael J Walter and Kenneth T Koga. The effects of chromatic dispersion on temperature measurement in the laser-heated diamond anvil cell. *Physics of the Earth adn Planetary Interiors*, 143-144:541–558, 2004.

[164] Yoshio Waseda. *The structure of Non-Crystalline Materials*. McGraw-Hill, 1980.

[165] T E Westre, A Di Cicco, A Filipponi, C R Natoli, B Hedman, E I Solomon, and K O Hodgson. GNXAS, a multiple-scattering approach to EXAFS analysis: methodology and applications to iron complexes . *J. Am. Chem. Soc*, 117:1566, 1995.

[166] E D Williamson and L H Adams. Density distribution in the Earth . *J. Washington Acad. Sci.*, 13:413–428, 1923.

[167] Kenichi Yaoita, Kazuhiko Tsuji, Yoshinori Katayama, Motoharu Imai, and Jian-Qiang Chen. The structure of liquid bismuth under pressure, 1992.

[168] C S Yoo, H Cynn, P Söderlind, and V Iota. New b (fcc) -Cobalt to 210 GPa. *Physical Review Letters*, 84(18):4132–4135, 2000.

[169] Choong-Shik Yoo, Per Söderlind, and Hyunchae Cynn. The phase diagram of cobalt at high pressure and temperature: the stability of -cobalt and new -cobalt. *Journal of Physics: Condensed Matter*, 10(20):L311–L318, 1998.

[170] Xueyang Yu and Richard A Secco. Equation of state of liquid Fe-17 wt % Si to 12 GPa. *High Pressure Research*, 28(1):19–28, 2008.

[171] Zhao-Yi Zeng, Cui-E Hu, Ling Cang Cai, and Fu-Qian Jing. *Physica B: Condensed Matter*, 407(3):330–334, 2012.

[172] Wen-jin Zhang, Zhi-yong Liu, Zhong-li Liu, and Ling-cang Cai. Melting curves and entropy of melting of iron under Earth's core conditions. *Physics of the Earth and Planetary Interiors*, 244:69–77, 2015.

[173] Wen-jin Zhang, Zhong-li Liu, and Yu-feng Peng. Molecular dynamics simulations of the melting curves and nucleation of nickel under pressure. *Physica B: Physics of Condensed Matter*, 449:144–149, 2014.

[174] Wen Jin Zhang, Yu Feng Peng, and Zhong Li Liu. Molecular dynamics study of melting curve, entropy of fusion and solid-liquid interfacial energy of cobalt under pressure. *Physica B: Condensed Matter*, 440:33–40, 2014.

[175] Youjun Zhang, Toshimori Sekine, Hongliang He, Yin Yu, Fusheng Liu, and Mingjian Zhang. Experimental constraints on light elements in the Earth's outer core. *Nature Publishing Group*, 6:1–9, 2016.

[176] V N Zharkov. *Equations of State for Solids at High Pressures and Temperatures*. Springer, 1971.

Acknowledgements

Many people have accompanied me in the adventure contained within these pages, and these words are dedicated to express my gratitude to them.

First of all, I want to thank Dr. Sakura Pascarelli, my supervisor, who enriched this work with her competence and enthusiasm, and who could always find time to devote to me when needed. Dr. Raffaella Torchio, my co-supervisor, had an invaluable role in this work. She provided teaching, guidance and company everyday over these past three years and I am very grateful for all her support.

I wish to thank Prof. Andrea Di Cicco, Prof. François Guyot, Dr. Daniele Antonangeli, Dr. Agnès Dewaele, Dr. Jean-Paul Itié and Prof. Alexandre Simionovici for agreeing to referee the present manuscript and for their precious comments and remarks.

This thesis wouldn't have been technically possible without the development of the laser heating system, for which I am indebted mainly to Innokenty Kantor, who patiently taught me how to use the setup and always answered all my curiosities. I wish to thank Guillaume Morard for the FIB and SEM post analysis, for his teaching and his friendship. I am grateful to thank Vanina Recoules for the molecular dynamics simulations and for her help. I am indebted to Keith Gilmore for his patience in explaining theoretical concepts to me and for the XANES and DOS calculations. I am grateful to Angela Trapananti who introduced me to the world of GnXAS and to Paola D'Angelo who continued to guide me in its use until good results were obtained. I would like to acknowledge the technical assistance of Jeroen Jacobs with the high pressure cells for experiments; along with Florian Perrin and Sebastien Pasternak for their prompt and decisive technical support on the beamline. I am also thankful to Gaston Garbarino and Mohamed Mezouar for helpful discussions during this work.

Both in preparing and performing experiments I was fortunate to benefit from the expertise, the practical support, and time of: Simone Anzellini, Ruggero Giampaoli,

Richard Briggs, Angelika Rosa, Francesca Miozzi and Alessandro Smareglia, as well as Raffaella Torchio, Innokenty Kantor, Guillaume Morard, Olivier Mathon and Sakura Pascarelli. I wish to thank all of them for their help and their ability to transform experiments into something fun.

I wish to thank my office mate Olivier Mathon for his company and his support over these past years as well as for revising the résumé. These past three years many people have been part of the ID24/BM23 team: Giovanni, Manuel, Armelle, Virginia, Margarita, Vera, Debora, Alberto, Nicolas, Kirill, Mourad, Naoki, Jogchum, Marija, Suresh, Antonella, Roger and some of the people already mentioned above. First of all I have to apology for complaining about the early lunches, and then I want to thank all of them for their company and camaraderie; in some of them I found real friends.

This time would not have been the same without the friends in Grenoble and those scattered all over Europe. Their company during coffee breaks, around a beer, somewhere in the mountains or back home during holidays and their constant presence made this adventure worthwhile. Among them I want to mention Oonagh, Ruxandra and Mauro to whom I am especially grateful for their time spent proofreading parts of this manuscript and Pierre for his help with the first writing(s) of the résumé.

Giulia and Leandro deserve to be thanked as well. Not only for indirectly participating in the experiments, but also for sharing their mum's time with me, especially in the last months.

I am indebted to my parents and my sister for transmitting to me since I was a child the way they see the world, and for their constant support and encouragement.

Finally, I'm deeply grateful to Mauro for his continuous presence, and for always understanding when it was the moment to encourage me or to scold me and tell me to take it easy.